12-22-2023

The Development and Validation of Novel Imaging Biomarkers for Uterine Contraction, Cervix and Placenta in Pregnancy

Wenjie Wu
Washington University – McKelvey School of Engineering

WASHINGTON UNIVERSITY IN ST. LOUIS

McKelvey School of Engineering
Department of Biomedical Engineering

Dissertation Examination Committee:
Yong Wang, Chair
Sarah K. England
Ian S. Hagemann
Daniel W. Moran
Pamela K. Woodard

The Development and Validation of Novel Imaging Biomarkers for Uterine Contraction, Cervix and Placenta in Pregnancy

by

Wenjie Wu

A dissertation presented to
the McKelvey School of Engineering
of Washington University in
partial fulfillment of the
requirements for the degree
of Doctor of Philosophy

December 2023
St. Louis, Missouri

Table of Contents

List of Figures

List of Tables

Acknowledgments

I would like to extend my deepest gratitude to my Ph.D. advisor for his invaluable mentorship throughout the course of my doctoral studies. As his first Ph.D. student, we navigated the complexities of early-stage clinical experimentation in electromyometrial imaging (EMMI) together. His guidance was instrumental in imparting the fundamental theories and methodologies essential for EMMI and Diffusion Basis Spectrum Imaging (DBSI) development. Beyond technical acumen, his continual encouragement and support have been pivotal in fostering my pursuit of innovative methods and clinical solutions.

I extend my gratitude to my committee members for their mentorship and the sharing of their knowledge and expertise. In alphabetical order, I thank Sarah K. England, PhD, Ian S. Hagemann, MD, PhD, Daniel W. Moran, PhD, and Pamela K Woodard, M.D. Their guidance has been invaluable to my academic progress.

I extend my sincere appreciation to my collaborators, whose contributions have been indispensable to my dissertation work and publications. In alphabetical order, I thank Alison G. Cahill, M.D., MSCI, Sarah K. England, PhD, Phillip S. Cuculich, M.D., Ian S. Hagemann, M.D., PhD, Hannah R Krigman, M.D., George A. Macones, M.D., MSCE, Robert C. McKinstry, M.D., PhD, Alan L. Schwartz, M.D., PhD, Pamela K Woodard, M.D., Qing Wang, PhD, and Nanbert Zhong, PhD, for their valuable investment of time, expertise, and knowledge.

I extend my gratitude to my lab members for their collaborative efforts and contributions to our research. In alphabetical order, I acknowledge Hansong Gao, Yujie Dun, PhD, Yuelin Li, Meng Jiang, Nilay Jakati, Zhexian Sun, Zulfia Kisrieva-Ware, PhD, Shengsheng Lai, Yiqi Lin,

PhD, Josephaone Lau, Yuan Nan, Wenxu Qi, MD, PhD, Peinan Zhao, PhD, Haonan Xu, Kara Wei, Hui Wang, PhD, Zezhen Xiang, and Zichao Wen, PhD.

I extend my gratitude to Deborah Frank, PhD, for her critical review of several manuscripts that constitute the outcomes of this dissertation. Her insights have been invaluable to the quality and rigor of the work presented.

I extend my gratitude to the Division of Clinical Research at the Department of Obstetrics and Gynecology at Washington University School of Medicine for managing the clinical studies. Additionally, I would like to thank, in alphabetical order, Monica Anderson, Jessica Battle, Tracy Burger, Jessica Chubiz, Madison Copeland, Emily Crews, Bri Dawson, Emily Diveley, Eva Goins, Lara Goodrich, Cassy Hardy, Jordyn Lehr, Claire Novack, Stephanie Pizzella, and Megan Steiner for their contributions to the clinical studies.

I extend my gratitude to multiple individuals for their respective contributions to this work. For clinical MR imaging, I thank Scott Love, BSRT, Mark Nolte, RT, and Glenn Foster, RT. Jim Quirk, PhD, provided expertise on the operation of the Varian 11.7T small animal MRI, while Jie Shen, PhD, offered guidance in biology and histology. Specimen collection was carried out by Sue Boss-Miller and Jessie Archie. Wet lab preparation was managed by Zulfia Kisrieva-Ware PhD, and histology sectioning was conducted by Alma Johnson. Histological staining tasks were handled by Phillip Foxwell and team, and Autumn Watson and the AMP team. Lastly, for literature review contributions, I acknowledge Wenxu Qi, MD, PhD, and Huijuan Zhang, MD.

I extend my appreciation to the Alafi Neuroimaging Laboratory for granting us access to their Hamamatsu NanoZoomer, which was funded by NIH shared instrumentation grant S10-RR0227552, for the digitization of histology images.

I extend my appreciation to the following organizations for their funding support, which has been instrumental in the completion of this dissertation: March of Dimes Center Grant (22-FY14-486), National Institutes of Health (NIH) / National Institute of Child Health and Human Development (R01HD094381 to PIs Y. Wang/Cahill; R01HD104822 to PIs Y.Wang / Schwartz / Cahill), National Institutes on Aging (R03AG072375-01 and R01AG074909 to PI Q. Wang), Burroughs Wellcome Fund Preterm Birth Initiative (NGP10119 to PI Y. Wang) and Bill & Melinda Gates Foundation (INV-005417, INV-035476, and INV-037302 to PI Y. Wang).

I extend my gratitude to my friends for their encouragement and emotional support throughout this endeavor. In alphabetical order, I thank Liu Cao, Qiyun Gao, Yining Huang, Lin Lin, Minglu Liu, Elena Lyashenko, Dennis C. Pease, PhD, Collleen Pease, Yizhe Song, Frank Wang, PhD, Jannice Yan, and Zhengyang Zhou, PhD.

Lastly, I extend my heartfelt gratitude to my parents and family for their unwavering support throughout my doctoral research journey. Their encouragement has been instrumental to my academic pursuits.

Wenjie Wu

Washington University in St. Louis

December 2023

Dedicated to my family.

ABSTRACT OF THE DISSERTATION

The Development and Validation of Novel Imaging Biomarkers for Uterine Contraction, Cervix and Placenta in Pregnancy

by

Wenjie Wu

Doctor of Philosophy in Biomedical Engineering

Washington University in St. Louis, 2023

Professor Yong Wang, Chair

Annually, nearly half a million neonates in the United States and 15 million globally are born preterm, defined as prior to 37 completed weeks of gestation. These births present elevated risks of neonatal mortality and long-term neurological deficits. The predominant obstetric precursors of preterm birth (PTB) include spontaneous preterm labor (45%), medically-indicated deliveries (30%), and preterm premature rupture of membranes (PPROM, 25%). Each precursor is associated with distinct physiological or structural alterations such as uterine contractions, placental dysfunction, or cervical insufficiency.

Current methodologies for monitoring uterine contractions, such as intrauterine pressure catheters and electrohysterography, possess limitations in spatial resolution, coverage, and specificity. Likewise, imaging techniques like optical-based methods and positron emission tomography have shown promise in animal studies for assessing placental immune response but are constrained by factors like invasiveness and temporal resolution, preventing their real-time, *in vivo* application in human subjects. Furthermore, various techniques, including cervical elastography, quantitative ultrasound, magnetic resonance elastography, optical coherence

tomography, Raman spectroscopy, and second harmonic generation imaging have been employed to quantitatively evaluate cervical remodeling, primarily in *ex vivo* specimens. Despite these advancements, existing methodologies lack the capability to discriminate and quantitatively assess cellularity, collagen fibers, and muscle fibers within each imaging voxel. Thus, a comprehensive understanding of the *in vivo* microstructure of the human cervix remains elusive.

This dissertation targets the multifaceted issue of PTB by focusing on three core biomarkers: uterine contractility, placental inflammatory processes, and cervical integrity. It is designed to advance imaging methodologies pertinent to each area. Aim 1 centers on the development and validation of noninvasive 3D imaging tools for analyzing uterine contractions. Aim 2 seeks to develop novel imaging modalities for evaluating inflammatory and immune responses in the placenta. Aim 3 concentrates on the development and validation of imaging methods for quantitative analysis of cervical microstructure. Through these efforts, the dissertation aspires to furnish clinicians and researchers with intuitive imaging tools for a more targeted, patient-specific understanding of the etiological factors contributing to PTB.

Chapter 1 : Introduction

1.1 Background and motivation

1.1.1 Cause of preterm birth

Each year, approximately half a million babies in the United States and 15 million globally are delivered preterm, defined as birth prior to 37 completed weeks of gestation[1]. These neonates are subject to elevated mortality rates and increased susceptibility to long-term neurological impairments[2,3]. Preterm birth (PTB) can principally be attributed to three key obstetric precursors: i) spontaneous preterm labor, accounting for approximately 45% of PTB occurrences; ii) medically-indicated deliveries due to maternal or fetal complications, constituting around 30% of PTB; and iii) preterm premature rupture of membranes (PPROM), responsible for an estimated 25% of PTB instances[4]. Spontaneous preterm labor is generally characterized by regular uterine contractions accompanied by cervical dilation, occurring prior to 37 weeks of gestation. In medically-indicated deliveries due to maternal or fetal complications, early and excessive inflammatory indication, fetal growth restriction and fetal distress are related to placental functions. PPROM is characterized by the spontaneous rupture of the amniotic membrane before 37 gestational weeks and at least one hour prior to the initiation of labor contractions, thereby excluding membrane rupture instigated by preterm labor. Early cervical remodeling, resulting in cervical insufficiency, may compromise the structural integrity of the amniotic membrane, potentially culminating in PPROM and subsequent preterm birth.

In the context of preterm birth, it is critical to recognize the interrelated nature of its three primary obstetric precursors before the event of delivery. The clinical pathway toward labor is conventionally delineated by a sequence of key events: increased uterine contractility, cervical dilatation, and rupture of fetal membranes[5]. the transition of the myometrium from a quiescent to a contractile state is concomitant with a signaling shift from anti-inflammatory to pro-inflammatory pathways. This involves the upregulation of specific chemokines [interleukin-8 (IL-8)], cytokines (IL-1 and IL-6), and contraction-associated proteins (oxytocin receptor, connexin 43, prostaglandin receptors)[6]. Progesterone serves a vital role in maintaining uterine quiescence by inhibiting the expression of these pro-inflammatory genes[6]. The placenta, an essential organ for hormone production and fetal immune protection, may also play a pivotal role in the timing of labor. Precocious or excessive activation of inflammatory processes within the placenta could affect the ability of the placenta to support a normally timed labor. Concurrently, in a typical pregnancy, cervical softening commences as early as the first trimester and progresses throughout the majority of the third trimester, all while maintaining tissue integrity[7–10]. This is followed by an accelerated ripening phase occurring a few weeks or days prior to labor. Finally, in conjunction with regular uterine contractions, the ripened cervix dilates, facilitating term delivery of the fetus[7]. If this physiological change manifests prematurely, absent concurrent uterine contractions, it could undermine the structural integrity of the amniotic membrane, leading potentially to PPROM and, consequently, preterm birth.

Consequently, this dissertation aims to address the complex issue of preterm birth (PTB) by focusing on three core parameters: i) uterine contractility, ii) inflammatory processes, and iii) cervical integrity. To elucidate these facets, the dissertation is structured to develop specialized imaging methodologies. Aim 1, elaborated in Chapter 2, focuses on the development and

validation of noninvasive three-dimensional imaging tools designed to investigate uterine contractions. Aim 2, detailed in Chapter 3, explores the imaging of inflammatory processes and immune responses in the placenta. Aim 3, covered in Chapter 4, delves into the development, validation, and quantitative analysis of the microstructural properties of the whole cervix. By employing these imaging techniques, the dissertation aspires to provide clinicians and researchers with tools that can offer a more systematic, patient-specific understanding of the factors leading to preterm birth.

1.1.2 Lack of imaging tools in investigation human uterus, placenta and cervix

In the study of preterm birth, research paradigms generally bifurcate into animal models and human clinical investigations. Animal models offer invaluable insights into the mechanisms underlying preterm parturition and facilitate the testing of intervention strategies. However, the translational applicability of these models to human physiology is inherently limited, as they do not fully represent the intricacies of human parturition.

On the other hand, human clinical studies necessitate safe and robust imaging modalities. Despite advances in imaging technology, there remains a significant gap in the availability of non-invasive, high-resolution tools for the quantitative assessment of the uterus, placenta, and cervix at organ level. A comprehensive review of current technologies is provided in the subsequent sections of Chapters 2, 3, and 4.

1.2 Contribution of the Dissertation

The principal contributions of this dissertation include:

- Development and validation of EMMI methodology and associated post-processing software for reconstructing uterine surface maps from body surface measurements and MRI-derived body-uterus geometry. Collaborative work with Hui Wang.
- Design and execution of animal (sheep) experiments to evaluate the accuracy, robustness, and feasibility of EMMI. Collaborative work with Hui Wang.
- Formulation of protocols for human EMMI studies, including experimental hardware, electrode patches, and procedures, and three-dimensional optical scanning of abdominal geometry. Collaborative work with Hui Wang.
- Conduct of human EMMI experiments in collaboration with the Wang lab team.
- Development of an *ex vivo* small tissue block DBSI imaging protocol using small animal MR scanner, which includes MRI coil design, MRI pulse sequences, post-MRI histological procedures such as sectioning, embedding, alignment, immunohistochemistry staining, and a post-experimental image processing pipeline. This protocol has been applied on human placenta, uterus, cervix, and brain tissue blocks.
- Development and validation of a placenta-specific DBSI methodology and associated post-processing software to generate DBSI-derived maps and metrics. Collaborative work with Zhexian Sun.
- Conduct of *ex vivo* DBSI imaging on placental tissue blocks. Primarily conducted by Wenjie Wu with assistance from Zhexian Sun, Haonan Xu, and Wenshang Wang.

- Development and validation of a whole-cervix DBSI methodology and associated post-processing software for generating DBSI-derived maps and metrics.
- Conduct of *ex vivo* DBSI imaging experiment on cervical tissue blocks.
- Conduct of *in vivo* cervical DBSI imaging experiment in collaboration with the Center for Clinical Imaging Research at Washington University School of Medicine.
- Conduct of a longitudinal case study of one patient within the cervical imaging cohort, including the DBSI experiment and data analyses of *in vivo* images, *ex vivo* whole uterus and cervix, and *ex vivo* small block.

1.3 Organization of the Dissertation

Chapter 2 focuses on the development and validation of noninvasive high-resolution electromyometrial imaging (EMMI) for uterine contractions, employing a translational sheep model.

Chapter 3 details the development and validation of placenta-specific diffusion basis spectrum imaging (DBSI).

Chapter 4 details the development and validation of whole-cervix DBSI imaging techniques for assessing collagen, muscle, and cellularity in both term and preterm birth scenarios.

Chapter 5 provides the concluding remarks of this dissertation and outlines future research directions.

Chapter 2 : Development and validation of noninvasive high-resolution electromyometrial imaging (EMMI) of uterine contractions in a translational sheep model

In this chapter, we introduce and validate a novel imaging modality, electromyometrial Imaging (EMMI), assessing its accuracy, robustness, and feasibility through experimentation on a pregnant sheep model.

2.1 The uterus and uterine contraction in pregnancy

The uterus is a muscular organ that that accommodates the implantation and growth of a fertilized embryo into a placenta and fetus[11]. Throughout the extended period of gestation, it expands and stretches, experiencing occasional local contractions that lack the intensity and coordination required for labor. At term, the uterus initiates a series of contractions sufficient to induce cervical dilation and generate enough intrauterine pressure to expel the fetus. Postpartum, it produces a distinct, sustained contraction to occlude blood flow to the severed vessels between the endometrium and placenta, thereby mitigating the risk of postpartum hemorrhage[11].

The precise timing and magnitude of uterine contractions are critical to uncomplicated term delivery and neonatal health. While mild, localized uterine activity prior to term generally poses no threat to gestational progress, early onset of forceful contractions may lead to preterm birth. Excessively forceful contractions at term could induce fetal hypoxia and distress, whereas

inadequately forceful contractions may necessitate delivery via Caesarean section[11]. Thus, the regulation of uterine contractility is complex yet essential for ensuring optimal birth outcomes.

Despite extensive research on uterine contractions, significant knowledge gaps persist in understanding the comprehensive uterine contraction dynamics during labor. Fundamental questions remain unresolved, including the initiation sites of uterine contractions, the mechanisms of contraction propagation, and the specific types of contractions that may result in preterm birth or necessitate cesarean delivery due to contractile dysfunction. The paucity of reliable imaging modalities for continuously monitoring the spatial contraction patterns across the entire uterus during labor further compounds these challenges, as elaborated in the subsequent sections.

2.2 Techniques to monitor uterine contractions

Several methodologies are available for the monitoring of uterine contractions, each presenting specific limitations. Manual abdominal palpation, although straightforward, is both time-consuming and subject to observer variability. Intrauterine pressure (IUP) measurement, recognized as the gold standard, entails the transvaginal insertion of an IUP catheter. Despite its widespread use, this invasive technique presents risks such as potential maternal and neonatal infection, thereby limiting its application to medically essential circumstances[12].

Tocodynamometers (TOCO) measure abdominal contour displacements associated with uterine contractions. While user-friendly and informative regarding contraction frequency and duration, TOCO data exhibit a weak correlation with IUP measurements[13]. Additionally, frequent transducer adjustments are necessary, and the method is susceptible to artifacts from maternal and fetal movements.

Magnetomyography (MMG) utilizes an array of sensors in a fixed-contour hemisphere positioned over the anterior abdomen during early labor[14,15]. Although MMG offers localized uterine activity maps and correlates with maternal perception of contractile events, it lacks three-dimensional spatial representation and necessitates specialized equipment within a magnetically shielded room.

Electrohysterography (EHG) employs abdominal electrodes to measure electrical potential changes corresponding to uterine contractions[16–18]. Despite recent advancements in spatial resolution via 4 × 4 (covering approximately 8 × 8 cm)[19,20] and 8 × 8 sensor arrays (covering 2.8 × 2.8 cm)[21], EHG remains confined to a limited abdominal area and thus lacks full three-dimensional view of the entire uterus.

Lastly, uterine electromyography (EMG) requires the direct application of electrodes to the uterine surface. Although utilized in animal models both *in vivo*[22] and *in vitro*[23,24], its invasive nature precludes its application in human studies.

2.3 Inspiration from electrocardiographic imaging

To address the constraints associated with current technologies for uterine contraction monitoring, this research draws upon the principles of electrocardiographic imaging (ECGI)[25–30]. ECGI integrates patient-specific body-heart geometry, captured through computed tomography, and high-resolution body surface electrical maps generated from up to 256 electrodes embedded in a vest. This framework enables the noninvasive imaging of cardiac electrical dynamics—including activation, propagation, and reentry circuits—with high temporal and spatial resolution and remarkable accuracy[27–31].

Motivated by this methodology, we have engineered an Electromyometrial Imaging (EMMI) system[32,33]. The EMMI system utilizes magnetic resonance imaging (MRI), known for its safety during pregnancy[34–36], to establish a body-uterus geometry. Electrical activity data are then recorded from a maximum of 256 abdominal electrodes and mapped onto this geometry through specialized EMMI software. This novel system allows the noninvasive, three-dimensional monitoring of uterine contraction initiation and propagation, thus offering a comprehensive depiction of electrical activity across the entire uterine surface.

2.4 Overview of EMMI

To construct a three-dimensional, subject-specific body-uterus geometry, magnetic resonance imaging (MRI) was employed following the placement of up to 256 MRI markers on the subject's abdominal and lumbar regions. During labor, these MRI markers were substituted with surface electrodes situated in identical locations, and multi-channel body surface potentials were synchronously recorded utilizing a portable electrical mapping apparatus. Subsequently, in a manner similar to the methodology employed in ECGI[26,37], the EMMI software employed the method of fundamental solutions to solve Laplace's partial differential equations. This facilitated the integration of the recorded electrical signals with the pre-established uterus geometry to produce uterine surface potential maps (**Figure 2.1A**), which represent the electrical activity across the uterus at a single time point. These potential maps were then employed to generate electrograms—temporal electrical waveforms at discrete uterine locations—and isochrone maps, which depict the patterns of temporal activation sequence across the entire uterine surface.

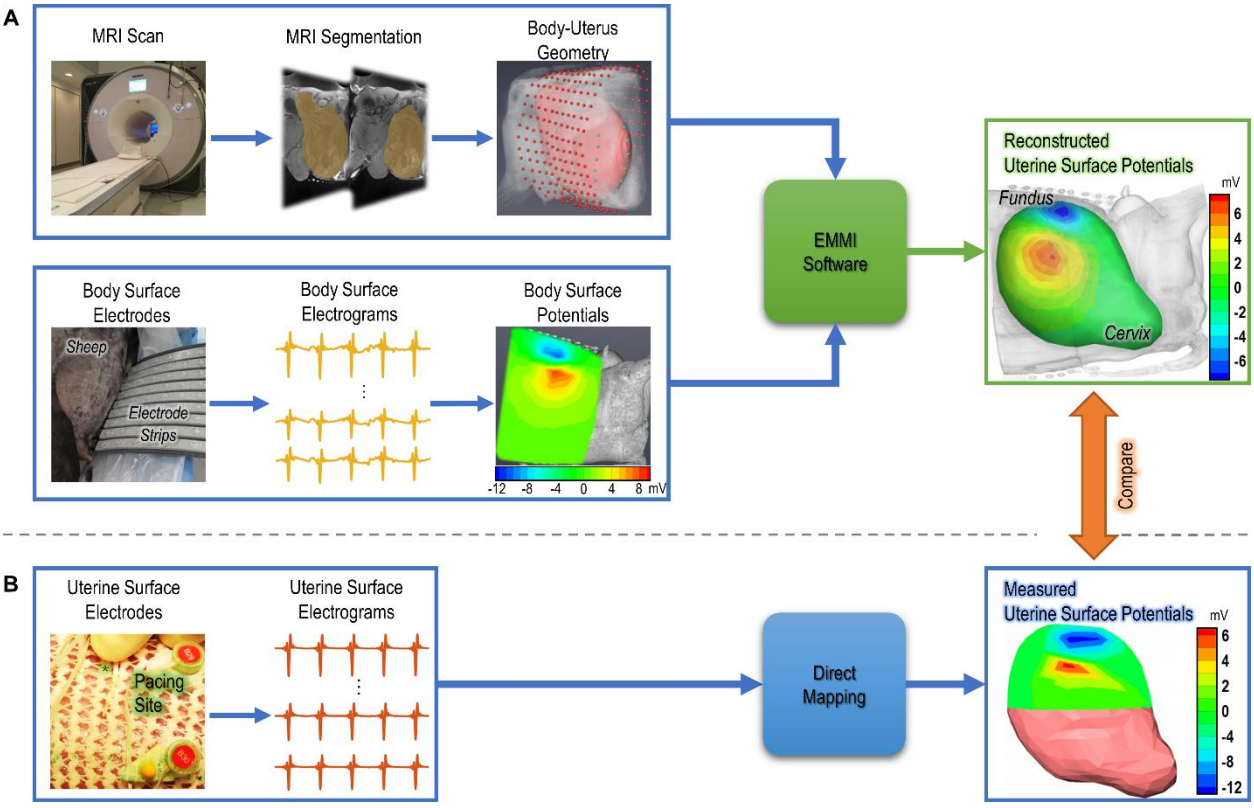

Figure 2.1: EMMI system and method to assess accuracy.
(A) MRI scans were acquired and then segmented to generate body-uterus geometry. On the body surface, up to 256 electrodes were placed in the locations of the corresponding MRI markers. Body surface electrograms were recorded and mapped onto body surface potentials. The measured body surface potentials and the body-uterus geometry were combined by EMMI software to generate reconstructed uterine surface potentials (spatial potential distribution on the 3D uterine surface at each instance in time). (B) The sheep uterus was surgically exposed, and an elastic sock containing 64 electrodes was slipped over the uterus. An electrical pacing lead (indicated by asterisk) was placed onto the uterine surface. After closing the abdomen, body surface electrodes were placed in their original locations. When pacing the uterus through the pacing lead, the uterine and body surface electrograms were recorded simultaneously. The uterine surface electrograms were directly mapped onto MRI-derived uterine surface to generate measured uterine surface potentials. Finally, the EMMI-reconstructed uterine surface potentials (A) were qualitatively and quantitatively compared to the measured (B) uterine surface potentials.

2.5 Experiment design

This study aims to develop and validate Electromyometrial Imaging (EMMI) for the noninvasive imaging of three-dimensional electrical activation patterns during uterine contractions. Initially, a pregnant sheep model was utilized to simultaneously acquire electrical potentials from both body surface and uterine surface electrodes. The accuracy of EMMI was validated by comparing reconstructed uterine potential maps with those directly measured from the uterine surface during pacing episodes. Subsequently, the robustness of EMMI in

reconstructing uterine electrical activation under clinically relevant conditions was assessed. Specifically, EMMI's ability to reconstruct uterine electrical activation maps during oxytocin-induced contractions was examined, even when subjected to simulated Gaussian noise and geometrical deformations. Finally, the feasibility of employing EMMI for noninvasive mapping of uterine contractions in humans was evaluated.

2.5.1 Sheep model and preparation

To evaluate EMMI, we employed near-term pregnant Katahdin sheep[22,38,39], a suitable animal model for human pregnancy due to their comparable abdominal dimensions. Despite the anatomical difference of a bipartite uterus in sheep, the weight of a single newborn offspring approximates that of a human neonate[38]. This breed also exhibits less lanolin skin secretions, enhancing the quality of electrical recordings. Moreover, the sheep's labor can be induced with precisely timed steroid injections[39,40]. Nine Katahdin sheep were initially selected; the first three served as pilot subjects for MRI sequence development and protocol refinement, while the subsequent six were utilized for electrical data collection. One sheep carrying twins was excluded, leaving five subjects for comprehensive evaluation of EMMI's accuracy, robustness, and feasibility.

Following procurement from Francis Sheep Farm, an institutionally approved vendor, Katahdin sheep in either their first or second pregnancies were selected between gestational days 140 and 145. Typically, this breed undergoes parturition around gestational day 147. To augment uterine responsiveness to oxytocin, intramuscular administration of dexamethasone (16 mg) was performed 24 to 48 hours prior to MRI[40,41]. Animals were subjected to fasting protocols in anticipation of anesthesia and subsequent study procedures. Anesthesia was induced using 10

mg/kg intramuscular ketamine, followed by isoflurane inhalation through a mask; this anesthetic regimen was maintained throughout MRI acquisition and any surgical interventions. Prior to experimental commencement, hair was thoroughly removed from the animals' abdominal region, extending circumferentially from the midthorax to the pelvis. All aforementioned procedures were conducted in strict compliance with the ethical guidelines set forth by the Washington University in St. Louis Institutional Animal Care and Use Committee.

2.5.2 Anatomical imaging by MRI

After the preparation, MRI markers were affixed externally to the sheep's lower abdomen and dorsal region (**Figure 2.2A, B**). Magnetic resonance imaging was performed on a 3T Siemens PRISMA scanner, utilizing a Radial Volume Interpolated Breath-hold Examination (VIBE) fast T1-weighted sequence with spatial resolution of 1 mm × 1 mm × 3 mm. Prior to the T1-weight imaging, a localizer sequence was employed to calibrate the field of view, ensuring comprehensive imaging of the entire uterus and cervix. The T1-weighted imaging was conducted along the axial direction, generating approximately 135 to 200 slices, contingent upon the individual dimensions of the sheep.

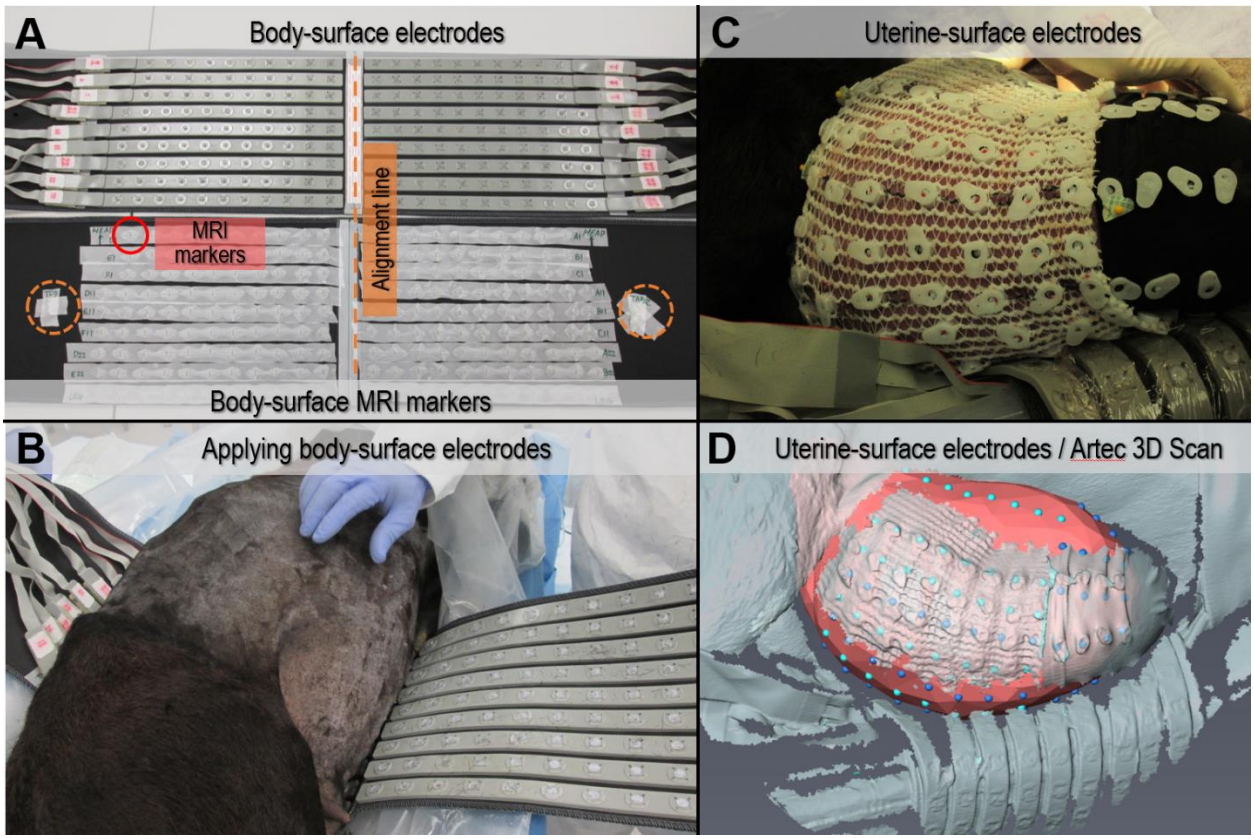

Figure 2.2: Body-surface electrodes and uterine-surface electrodes.
(A) Body-surface electrodes were affixed to a wide belt, aligned with MRI markers. A red circle indicates an MRI marker. Orange dashed lines and circles signify alignment marks present on both the MRI marker belt and the electrode belt. (B) Placement of body surface electrodes. (C) Application of a uterine electrode sock equipped with pin-type active electrodes. (D) The uterine surface (pink) was rendered following segmentation on MRI slices. Uterine surface electrodes (in blue and cyan) were labeled directly beneath on the uterine surface. The overlaid cyan surface, generated from an Artec 3D scan conducted during surgery, was used as alignment information for the uterine surface electrodes.

2.5.3 Surgery and electrical mapping

Within one hour after the MRI, the sheep was transferred to the operating room and positioned in left lateral recumbency. Multiple oxytocin boluses (10–20 units, intravenously) were administered, and uterine contractions were monitored via tocodynamometry (TOCO). Preexisting MRI markers on the body surface were substituted with unipolar active electrodes at corresponding sites (**Figure 2.2B**). For the EMMI feasibility assessment, up to 256 body surface electrodes were connected to a BioSemi portable acquisition system and initiated for electrical recording at a sampling rate of 2048 Hz and a 24-bit resolution. This occurred approximately 15–40 minutes prior to surgical intervention.

To facilitate the paralumbar surgical entry, body surface electrodes were retracted dorsally and ventrally. Lidocaine was infiltrated subcutaneously to create a local line block. An incision was made in the right lateral paralumbar fossa to access the abdomen, whereupon the uterus was identified and exteriorized to fit a specialized electrode sock on the uterine surface (**Figure 2.1B**, **Figure 2.2C**). Oxytocin-induced uterine contractions were confirmed by two obstetricians (A.G.C, J.S.R) and a veterinary surgeon (M.T.).

Unipolar pin-type active electrodes were inserted into designated holders on the sock and in direct contact with the uterine surface. The sock was placed such that one column of electrodes was in line with the fetus's spine. Specific electrode placement was documented as per **Figure 2.2C, D** and **Figure 2.4A, B**. For sheep labeled A and B, a cardiac pacing lead, regulated by a Medtronic 5375 Pulse Generator, was positioned adjacent to one of the uterine surface electrodes and in direct contact with the uterine surface. Subsequently, the uterus was reinserted into its anatomical location, and the abdominal layers were sutured closed. The sheep was then reoriented into a prone position, and body surface electrodes were restored to their initial positions.

Simultaneous electrical sampling from both body surface and uterine surface electrodes was performed for approximately 30 minutes. For EMMI accuracy evaluation, electrical pulse trains with inter-pulse durations of either 0.5 or 1 second were applied. For robustness assessments, body surface electrodes were disconnected, retaining only the uterine surface electrodes for data acquisition. Following the completion of all measurements, both the ewe and the fetus were euthanized. All electrodes were subsequently removed, sterilized, and repurposed for future use.

2.5.4 Configurations of electrical mapping system

EMMI's electrical mapping system employed BioSemi (Amsterdam, Netherlands) sintered silver-silver chloride active electrodes, each with an integrated pre-amplifier. For body surface potential mapping, up to 24 rubber strips embedded with flat electrodes were used, yielding a total of 256 electrodes. Uterine surface potentials were recorded using either 64 or 128 pin-type electrodes. The BioSemi portable acquisition system comprised a battery-powered recording box, a fiber-optic cable, a fiber-to-USB converter, and a data-collection computer. Potentials were sampled and digitized at a rate of 2048 Hz with 24-bit precision on a battery-powered recording box. The human subject is protected by optical isolation between the recording box and the data-collecting computer. The leak current of the system is specified as less than 1 µA, well below the safety threshold of 10 µA[42,43]. The system automatically deactivates its circuitry if leakage current exceeds the safety level[43].

Electrical recordings were acquired in unipolar configuration, utilizing the Wilson Central Terminal as a virtual reference; this is the average value of all three common-mode sensing electrodes. The common-mode sensing electrodes—left arm (LA), left leg (LL), and right arm (RA)—were positioned on the sheep's right rear leg (LA and LL) approximately 5 cm apart, and on the right shoulder (RA). These common-mode electrodes were recorded simultaneously with all other unipolar electrodes. During post-experimental signal processing, the virtual reference was subtracted from all unipolar recordings to achieve a full 80 dB common-mode rejection ratio, as per BioSemi's guidelines.

2.6 Schemes for evaluating EMMI

In this section, we elucidate the evaluation schemes for EMMI using a term pregnant sheep model. The assessment comprises three primary dimensions: accuracy, robustness, and feasibility. First, we establish the accuracy of EMMI by demonstrating that uterine surface electrical potential maps reconstructed from body surface potentials align with those directly measured from uterine surface electrodes during electrical pacing. Second, the robustness of the EMMI method is confirmed by its capacity to reconstruct uterine electrical activation maps in the context of oxytocin-induced contractions, even when faced with simulated Gaussian noise and geometric deformations. Finally, we demonstrate the feasibility of EMMI for noninvasive mapping of induced uterine contractions. Collectively, the results point to EMMI's potential utility as a valuable tool for evaluating uterine contractility in human subjects, given its established safety, accuracy, robustness, and feasibility.

2.6.1 EMMI accuracy

To evaluate the accuracy of EMMI, we employed a validation scheme comparable to that utilized for ECGI, wherein epicardial potentials recorded from an animal heart were compared to those reconstructed from body surface potentials measured in a human-torso-shaped tank containing the suspended animal heart[26,44]. We conducted MRI on anesthetized sheep wearing MRI markers situated around the lower abdomen and back (**Figure 2.1A**) to create a body-uterus geometry. We then surgically exposed the uterus, slipped an elastic sock containing 64 electrodes over the uterus and placed a cardiac pacing lead directly on the uterine surface through the sock. The uterus was returned into its anatomical location, followed by abdominal closure.

Post-surgery, 192 electrodes were placed on the body surface in the same position as the MRI markers. Controlled electrical pacing of the uterus was performed via the pacing lead while electrical potentials were simultaneously recorded from both body and uterine surface electrodes. We then used EMMI software to reconstruct uterine surface potential maps from the body surface potentials and MRI-derived body-uterus geometry. The final stage of accuracy assessment entailed a comparative analysis between the reconstructed uterine surface potential maps and those directly measured during the pacing episodes (**Figure 2.1A, B**).

2.6.2 EMMI robustness

To ascertain the robustness of EMMI under clinically relevant conditions, we examined its performance in several scenarios: the influence of maternal and fetal movements occurring post-MRI but prior to or during electrical recording, and the potential impact of ambient electrical noise generated by proximate equipment. We employed a scheme (**Figure 2.3**), similar to a well-established scheme used to validate ECGI[45,46], to evaluate the robustness of EMMI electrogram, potential map and isochrone maps.

Specifically, in this scheme (**Figure 2.3**), up to 128 sock electrodes were used for direct recording of uterine surface potentials during labor in the sheep model. Oxytocin-induced uterine contractions were visually confirmed by two obstetricians (A.G.C, J.S.R.) and one veterinary surgeon (M.T.). Utilizing these measured uterine potentials and MRI-acquired body-uterus geometry, we forward computed the bioelectric field on the body surface, employing the Boundary Element Method for discretization of the bioelectric field equations[45–49]. To simulate real-world clinical variables, we introduced 1) Gaussian noise (10% in amplitude) into the computed body surface potentials, 2) Gaussian-distributed geometric error (up to 1 cm over all of the surface) to

both the uterus and body surface geometries, or 3) both 10% noise and maximal 1 cm deformation. Subsequently, uterine surface potential maps were reconstructed from these body surface potentials using EMMI, which employs the Method of Fundamental Solutions[37]. Finally, a comparative evaluation was conducted between the directly measured and EMMI-reconstructed uterine data, focusing on electrograms, potential maps, and activation isochrones.

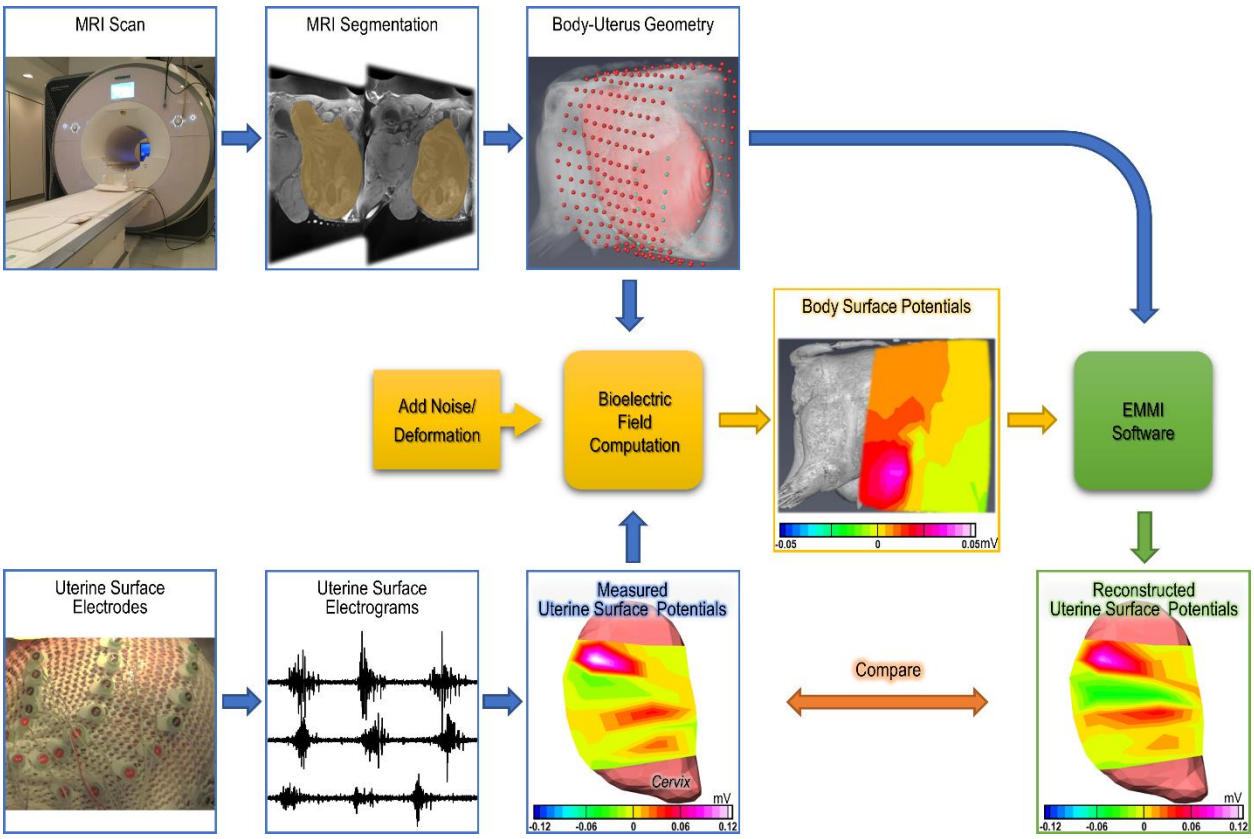

Figure 2.3: Method to assess EMMI robustness.
MRI scans were acquired to provide body-uterus geometry. Next, the uterus was surgically exposed, and an elastic sock containing up to 128 electrodes was slipped over the uterus. The uterine surface potentials were recorded at 2048 Hz sampling rate. Next, adding noise, deformation, or both combined in bioelectric field computation, the body-uterus geometry and experimentally measured uterine surface potentials were used to generate the body surface potentials. EMMI software was then used to reconstruct uterine surface potentials. Finally, the EMMI-reconstructed and measured uterine surface potentials were compared.

2.6.3 EMMI feasibility

In the final phase of our evaluation, we assessed the feasibility of EMMI for noninvasive mapping of uterine surface potentials, utilizing measured body surface potentials only. Data were acquired from the body surface of four sheep following the administration of a minimum of two oxytocin boluses, prior to surgical intervention. The presence of electrical activity bursts on the body surface, corresponding to uterine contractions, was confirmed through measurements and subsequent validation by two obstetricians (A.G.C, J.S.R.) and a veterinary surgeon (M.T.).

2.7 Computational methods for EMMI data analysis

This section describes the computational methods that are used in the evaluation schemes for EMMI.

2.7.1 Signal processing

For assessing EMMI accuracy and robustness, similar signal processing procedures were applied, except that different filter cutoff frequencies and down-sample ratios were used because the native frequency spectrum of the pacing pulse differed from that of oxytocin-induced uterine electrical activity. For assessing EMMI accuracy, raw pacing recordings (at a 2048 Hz sampling rate) from both body surface and uterine surface were down-sampled by 16 via two steps: first, a 64 Hz Butterworth anti-aliasing low-pass filter (-80 dB at 128 Hz) was used to down-sample by 8; second, a 45 Hz low-pass filter (-80 dB at 64 Hz) was used to down-sample by 2. Finally, a 0.6 Hz Butterworth high-pass filter was applied to remove baseline drift, followed by an 18 Hz low-pass filter. For assessing EMMI robustness, raw uterine electrical recordings were filtered with a fourth-order Butterworth notch filter (stop band at 0–0.5 Hz and 59.5–60.5 Hz) and then filtered with a 40 Hz Butterworth low-pass filter. The resulting recordings were then down-sampled by 20 and

filtered with a 10 Hz low-pass filter. For assessing EMMI feasibility, raw body surface electrical recordings were processed the same way as uterine electrical recordings. Large baseline drifts were removed by semi-automatically suppressing the signal's magnitude to the mean value of neighboring signals. If poor electrode contact occurred, as indicated and documented by the BioSemi recording device, the electrical signals recorded from those electrodes were excluded.

2.7.2 Sheep body-uterus geometry segmentation

Amira software was utilized for the segmentation of body-uterus geometry, which was established on absolute Cartesian coordinates based on DICOM header and MRI voxel dimensions. The process involved multiple steps to assure accurate registration and mapping. Initially, a 3D abdomen surface of the sheep was constructed from MRI data by setting a threshold for the high-contrast body-air interface (**Figure 2.4A**). Locations of high-contrast MRI markers on this 3D surface were then labeled. Subsequently, the uterus was manually segmented, culminating in a rendered uterine surface (**Figure 2.4B**). For anatomical registration, sock electrodes aligned with the fetus's spine were first marked on this uterine surface; the spine itself serves as a precise landmark identifiable through MRI. Thereafter, additional uterine surface electrodes were labeled in accordance with the geometric configuration—specifically the rows and columns—of the electrode sock. Minor spatial adjustments were performed based on photographic documentation from various angles.

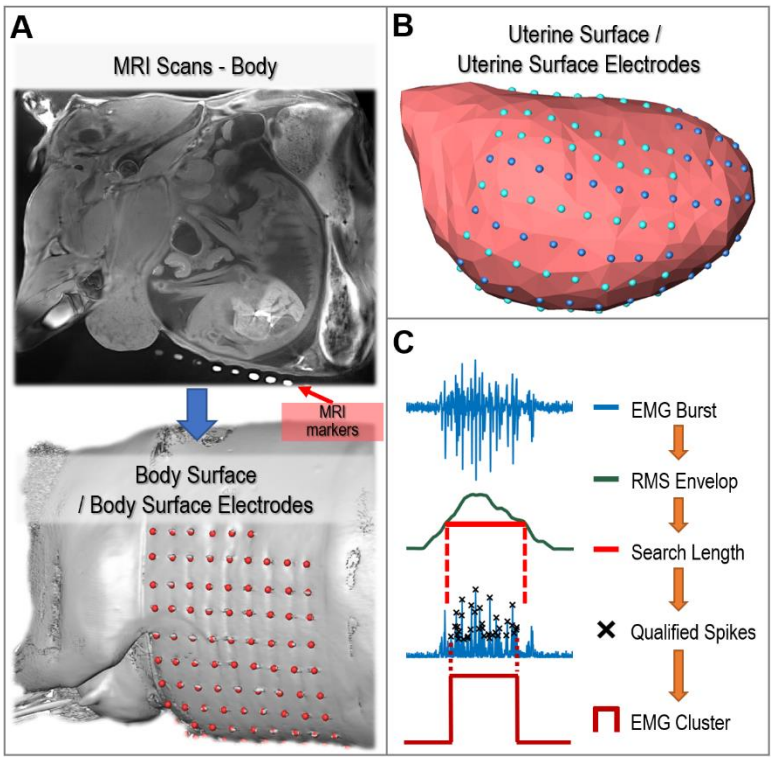

Figure 2.4: Methods to generate sheep body and uterus geometry and to identify EMG burst clusters in electrograms.
(A) MRI scans were rendered to a surface of sheep body in Amira software. Red arrow indicates a row of MRI markers (shown as bright dots on the MRI image). The locations of MRI markers representing body surface electrodes were labeled as red dots on the body surface. (B) Uterine surface (pink) was rendered after segmenting uterus on MRI slices. Uterine surface electrodes (blue and cyan) were labeled directly on the uterine surface below. (C) An EMG burst was converted into an RMS envelope and the search length is determined by the width (at half height) of the envelope. An automated algorithm identified the first and the last qualified spikes within the search length. The first and the last spikes were then marked as the start and end of an EMG burst cluster respectively.

2.7.3 Bioelectric-field forward computation

In the context of an electro-quasistatic problem, the governing equations are:

Electric Field	$\vec{E} = -\nabla\varphi$	(2.1)
Ohm's Law	$\vec{J} = \sigma\vec{E}$	(2.2)
Divergence	$\nabla \cdot \vec{J} = I_v$	(2.3)
Poisson's Equation	$\nabla \cdot \vec{J} = I_v = -\sigma\nabla^2\varphi$	(2.4)

Combining **Equation 2.1 – 2.3**, we could derive the Poisson's Equation (**Eq. 2.4**). In our particular case, with no electrical source present within the volume conductor, the Poisson's Equation becomes the Laplace equation (**Eq. 2.5**). The volume conductor is considered as a multiple-connected domain bounded by the uterine and body surfaces. Dirichlet boundary conditions are specified by the measured electrical potentials on the uterine surface (**Eq. 2.6**), while the Neumann boundary condition with a zero value is applied to the body surface, reflecting the electrical insulating effect of air (**Eq. 2.7**). Solving this Laplace equation[46] yields the body surface potentials, described as the following equations:

$$\nabla^2\varphi(x) = 0, x \in \Omega \quad (2.5)$$

Dirichlet condition

$$\varphi(x) = \varphi_U(x), x \in \Gamma_U \quad (2.6)$$

Neumann condition

$$\frac{\partial\varphi(x)}{\partial n} = 0, x \in \Gamma_B \quad (2.7)$$

where Ω is the 3D volume between the body surface Γ_B and the uterine surface Γ_U. The volume Ω is assumed to be homogeneous. $\varphi(x)$ represents the potential at location x. $\varphi_U(x)$ represents the potential on the uterine surface. $\frac{\partial\varphi(x)}{\partial n}$ represents the normal derivative of the potential on the body surface, which equals zero because the body surface Γ_B separates the conductive volume Ω and the non-conductive air outside of volume Ω. Similar to the validation work in ECGI[26,45,47], the Boundary Element Method was used to discretize the Dirichlet and Neumann conditions and the Laplacian equation. After discretization, body surface potentials (Φ_B) can be related with uterine surface potentials (Φ_U) through a linear matrix A, as **Equation 2.8**. A is the transfer matrix encoding the body-uterus geometrical relationship. Because the boundary

conditions were known on both boundaries, the computation was well-posed, stable, and accurate[26].

$$\Phi_B = \mathrm{A}\,\Phi_{\mathrm{U}} \qquad (2.8)$$

2.7.4 Noise and geometric deformation

For the assessment of EMMI robustness, Gaussian noise, constituting 10% of the signal amplitude, was added into the calculated body surface potentials (**Eq. 2.9**). Additionally, Gaussian-distributed geometric errors (3 times standard deviation = 1 cm) were introduced to both uterine and body surface geometries.

2.7.5 EMMI inverse computation

In the inverse computation, consistent with the assumptions of the bioelectric field calculation, the Laplace equation governs the 3D electro-quasistatic field (**Eq. 2.5**). Multi-channel electrical mapping systems captured body surface electrical activities, employing the Dirichlet boundary condition (**Eq. 2.9**) and the predefined zero Neumann boundary condition (**Eq. 2.10**) on the body surface.

Dirichlet condition
$$\varphi'(x) = \varphi_B(x) + \varphi_N(x)\,, x \in \Gamma_B \qquad (2.9)$$

Neumann condition
$$\frac{\partial \varphi'(x)}{\partial n} = 0, x \in \Gamma_B \qquad (2.10)$$

where $\varphi_B(x)$ represents the potential on the body surface and $\varphi_N(x)$ represents the Gaussian noise added to $\varphi_B(x)$ on the body surface. To solve the inverse problem of EMMI, the

Method of Fundamental Solution (MFS) was used to discretize the Laplacian equation as well as Dirichlet and Neumann conditions as described by **Equation 2.9** and **Equation 2.10**. MFS was accurate for solving inverse bioelectric field problems in other systems[37]. Because boundary conditions are known on the body surface and no boundary conditions are known on the uterine surface, the EMMI computation involves the inverse of a highly ill-conditioned matrix[37]. To obtain a stable inverse potential solution on the uterine surface $\varphi'(x), x \in \Gamma_U$, zeroth order Tikhonov regularization was used[37,50]. The degree of regularization was determined by the Composite Residual and Smoothing Operator method (CRESO)[26,51]. Specifically, we used a scaled mean CRESO parameter.

2.7.6 Processing of potential maps, electrograms, and isochrone maps

Upon completing the EMMI inverse computation, uterine surface potential maps were generated, which display potential distribution over the entire uterine surface at a given time point. An electrogram provides temporal features of electrical activity at a local site on the uterine surface and was generated by assembling a time series of potential values at a given uterine site from the potential maps. An isochrone was generated by assembling local activation time of each uterine surface site during an observation window. The start of an observation window was selected as the time point when uterine electrical activity started to occur on a previously resting uterus, and the end of an observation window was selected as the time point when the uterus returned to electrical quiescence.

To define the precise local activation time from electrograms at each uterine surface site, we developed an automatic electrical burst clustering algorithm (See **Figure 2.4C** for an algorithm flowchart.) The algorithm started by extracting a root-mean-square (RMS) envelope of rectified

electrogram signals (absolute value of original electrogram). A search length was determined by the width at half height of the RMS envelope. The algorithm defined qualified spikes as those with height at least 0.5 times the difference between the two centroids found by a soft-threshold K-mean clustering. In the search window, the first and last qualified spikes were marked as the start and end of an electrical burst cluster. The start of the electrical burst was defined as the activation time. If no electrical burst cluster was detected, the activation time was labeled as "inf". To provide comprehensive information of activation sequences over time on the entire uterine surface, we generated activation movies that trace the uterine activation wave front in a frame-to-frame fashion.

2.7.7 Statistical analysis

In this study, we employed Pearson correlation-coefficients (CC) and relative error (RE) to quantify accuracy of EMMI-reconstructed uterine surface potentials, electrograms and isochrone maps. CC and RE have been well accepted and used in ECGI studies[28,46,52,53].

The EMMI-reconstructed uterine surface potentials were compared to the measured uterine surface potentials by calculating the correlation coefficient (CC) and relative error (RE). The equations defining CC and RE are as follows:

$$CC = \frac{\sum_{i=1}^{L}\left(V_i^M - \overline{V^M}\right)\left(V_i^R - \overline{V^R}\right)}{\sqrt{\sum_{i=1}^{L}\left(V_i^M - \overline{V^M}\right)^2}\sqrt{\sum_{i=1}^{L}\left(V_i^R - \overline{V^R}\right)^2}} \tag{2.11}$$

$$RE = \sqrt{\frac{\sum_{i=1}^{L}(V_i^R - V_i^M)^2}{\sum_{i=1}^{L}(V_i^M)^2}} \tag{2.12}$$

CC is a statistical measure calculating the strength of the relationship between two variables. The range of CC values is between -1.0 to 1.0. A CC of -1.0 indicates a perfect negative correlation, while a CC of 1.0 indicates a perfect positive correlation. A CC of 0.0 indicates no

relationship between the two variables. RE is a statistical measure of precision, defined as the ratio of the absolute error of a measurement to the measurement being examined. RE is dimensionless and expressed as a percentage.

For electrograms, we calculated the temporal CC and RE. L represents the number of sample points over time at which potentials were measured and reconstructed. V_i^M and V_i^R represent the measured and reconstructed potentials, respectively, at the i^{th} sample point. $\overline{V^M}$ and $\overline{V^R}$ represent the temporal average of the measured and reconstructed potentials, respectively.

For potential maps and isochrone maps, we calculated spatial CC and RE. L represents the number of uterine sites at which potentials were measured and reconstructed. V_i^M and V_i^R represent the measured and reconstructed potentials, respectively, at the i^{th} uterine site. $\overline{V^M}$ and $\overline{V^R}$ represent the spatial average of the measured and reconstructed potentials, respectively. In this analysis, reconstructed potential maps during contractions or pacing pulses were compare with corresponding measured uterine potentials, and reconstructed isochrone maps were compared with corresponding measured isochrone maps.

Wilcoxon rank sum test was performed to test the difference in the spatial resolution of measured data and EMMI reconstruction.

2.8 Evaluation of EMMI accuracy

We recorded a total of 118 independent pacing pulses from two sheep. The pacing lead, denoted by an asterisk in **Figure 2.5**, was positioned near the fundus in the upper uterine segment of sheep A (**Figure 2.5A**) and in the middle uterine segment of sheep B (**Figure 2.5B**). **Figure 2.5** illustrates both measured and EMMI-reconstructed uterine surface potential maps in a right lateral view during three independent pacing pulses for both sheep A and B. In these maps, warm and cool colors signify positive and negative potentials, respectively.

Measured potential maps only partially cover the uterine surface due to the limitations imposed by the number of sock electrodes. Conversely, EMMI-reconstructed maps, generated from body surface potentials, offer a complete view of uterine potential distribution. The mean electrode spacing for the measured potential maps was 47 ± 21 (standard deviation) mm for sheep A and 48 ± 18 mm for sheep B. The mean reconstruction point spacing for the EMMI-reconstructed maps was 31 ± 8 mm for sheep A and 32 ± 7 mm for sheep B. A Wilcoxon rank sum test rejected the null hypothesis that the spatial resolution of EMMI-reconstructed maps was equivalent to that of the direct-measured maps ($p < 2.2\times10^{-16}$). Notably, the measured potential maps exhibited interpolation artifacts, manifesting as triangular shapes, attributable to the limited number of sock electrodes.

In both directly measured and EMMI-reconstructed uterine surface potential maps, negative potential centers (*N* and *N'* in **Figure 2.5**) were observed adjacent to the pacing leads (white asterisk in **Figure 2.5**). Positive potential centers (*P* and *P'* in **Figure 2.5**) were also noted in close proximity. These potential centers exhibited comparable spatial locations in both types of maps. Specifically, in sheep A (**Figure 2.5A**), the negative and positive potential centers differed

by 16.5 ± 7.2 mm (mean ± standard deviation) and 28.8 ± 11.4 mm, respectively between the measured and EMMI-reconstructed potential maps, and the angles of the vectors connecting the negative and positive centers differed by 6.1 ± 6.5º (N=138, from 30 pacing pulses, summarized in **Table 2.1**). Similarly, in sheep B (**Figure 2.5B**), the negative and positive potential centers differed by 2.9 ± 0.0 mm and 8.1 ± 6.3 mm, respectively between the measured and EMMI-reconstructed potential maps, and the angles of the vectors connecting two centers differed by 7.5 ± 8.2º (N=390, from 78 pacing pulses, in **Table 2.1**).

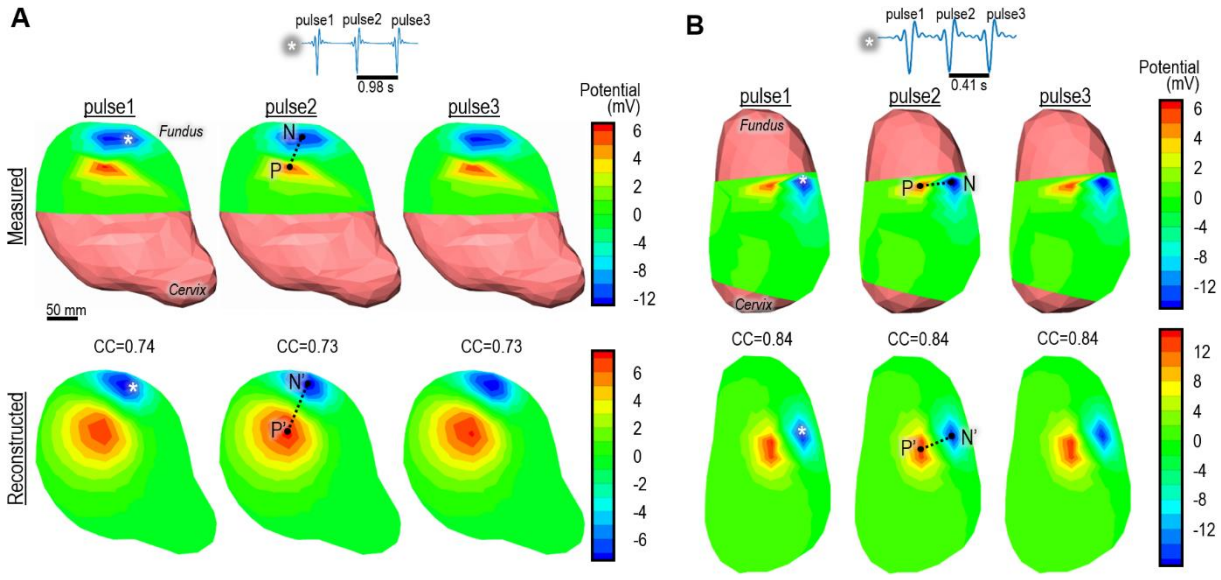

Figure 2.5: Right lateral view of the uterine surface potential maps during pacing pulses.
Potential maps at the peaks of three pacing pulses for sheep A and sheep B. Electrograms at top were from sites of the pacing leads (white asterisks). N and N' denote negative potential centers in the measured and EMMI-reconstructed potential maps respectively, while P and P' denote positive potential centers in the measured and EMMI-reconstructed potential maps respectively. Dashed lines denote vectors connecting the negative and positive centers. Spatial correlation coefficients (CCs) of the potential maps shown on this figure (defined in Eq. 7) were computed at the peak of each pacing pulse. Distance error of negative and positive potential centers between the measured and EMMI-reconstructed potential maps and CC of potential maps were analyzed during all pacing pulses for sheep A (N=138) for sheep B (N=390), summarized in Table 2.1.

To evaluate the accuracy of EMMI reconstruction quantitatively, correlation coefficients (CCs) were calculated between the measured and EMMI-reconstructed uterine surface potential maps. These CCs reflect the spatial correlation between measured and EMMI-reconstructed

potential maps at a single time frame for 62 electrode sites in sheep A and 49 electrode sites in sheep B (64 electrodes were placed on the uterus in both sheep, but data from 2 electrodes in sheep A and 15 electrodes in sheep B were excluded due to suboptimal electrical contact with the uterus). CC values (constrained between 0 and 1) indicate similarity; values approaching 1 indicate high similarity. Potential map CC values had median of 0.71 [first quartile (Q1) = 0.67, third quartile (Q3) = 0.74] for sheep A (N=138) and 0.83 [0.81, 0.84] for sheep B (N=390). These CC values support that EMMI is capable of reconstructing uterine surface potential maps with a high degree of accuracy, as evidenced during uterine pacing experiments in sheep.

Table 2.1: Accuracy analysis of all pacing data, electrograms, potential maps and isochrone maps reconstructed by EMMI.

EMMI Accuracy (Pacing)		**N =**	**Distance Error of Negative Epicenter (mm)** Mean ± std	**Distance Error of Positive Epicenter (mm)** Mean ± std	**Angular Error (degree)** Mean ± std	**Potential Map CC** Median [Q1, Q3]
Sheep A		138	16.5 ± 7.2	28.8 ± 11.4	6.1 ± 6.5	0.71 [0.67, 0.74]
Sheep B		390	2.9 ± 0.0	8.1 ± 6.3	7.5 ± 8.2	0.83 [0.81, 0.84]
EMMI Robustness		**N =**	**Median CC [Q1, Q3]**		**Median RE [Q1, Q3]**	
Electrogram	Noise	595	0.85 [0.72, 0.95]		0.55 [0.36, 0.78]	
	Deformation		0.83 [0.69, 0.93]		0.62 [0.42, 0.86]	
	Noise & Deformation		0.83 [0.68, 0.93]		0.63 [0.43, 0.87]	
Potential Map	Noise	28120	0.80 [0.71, 0.86]		0.59 [0.48, 0.73]	
	Deformation		0.78 [0.68, 0.85]		0.64 [0.52, 0.78]	
	Noise & Deformation		0.77 [0.67, 0.84]		0.64 [0.53, 0.78]	
Isochrone Map	Noise	25	0.99 [0.96, 1.00]		0.01 [0.00, 0.06]	
	Deformation		0.98 [0.95, 0.99]		0.02 [0.01, 0.08]	
	Noise & Deformation		0.97 [0.94, 1.00]		0.03 [0.01, 0.08]	

2.9 Evaluation of EMMI robustness

As described in section 2.6.2, the robustness of EMMI is assessed through the evaluation of its electrograms, potential maps, and isochrone maps.

2.9.1 EMMI electrogram

We initiated our analysis by evaluating individual "episodes," characterized as recording segments lasting 300 ± 70 seconds and typically containing 5–9 electrical bursts at each contracting site. Accuracy was quantified using the Correlation Coefficient (CC), which gauges the temporal correlation between the measured and EMMI-reconstructed electrograms at each uterine site, and the Relative Error (RE, Eq. 2.8), which assesses the magnitude discrepancy between the measured and EMMI-reconstructed electrograms. RE is unbounded, with zero indicating perfect agreement.

In Episode #1, we applied both CC and RE metrics to evaluate the concordance between measured and EMMI-reconstructed uterine electrograms under varying conditions: presence of noise, geometrical deformation, or a combination of both. Under noise conditions, median CC and RE values were 0.88 [0.73, 0.96] and 0.55 [0.32, 0.78] respectively. With geometrical deformation, median CC and RE were 0.86 [0.71, 0.94] and 0.62 [0.41, 0.83], respectively. Under combined conditions, median CC was 0.86 [0.70, 0.94] and RE was 0.63 [0.41, 0.85] (**Figure 2.6A**). Subsequent analysis focused on a subset of five representative sites (15, 19, 21, 48, 53) (**Figure 2.6B**). EMMI-reconstructed electrogram morphologies at these sites were highly similar to measured morphologies, with CC ranging from 0.70 to 0.95 under all test conditions (**Figure 2.6C**). RE values, indicating the integrity of reconstructed electrical amplitudes, ranged from 0.34 to 0.71 across all uterine locations. Additional comparative analyses between measured and EMMI-reconstructed electrograms for Episode #2-8 are presented in **Figure 2.7**.

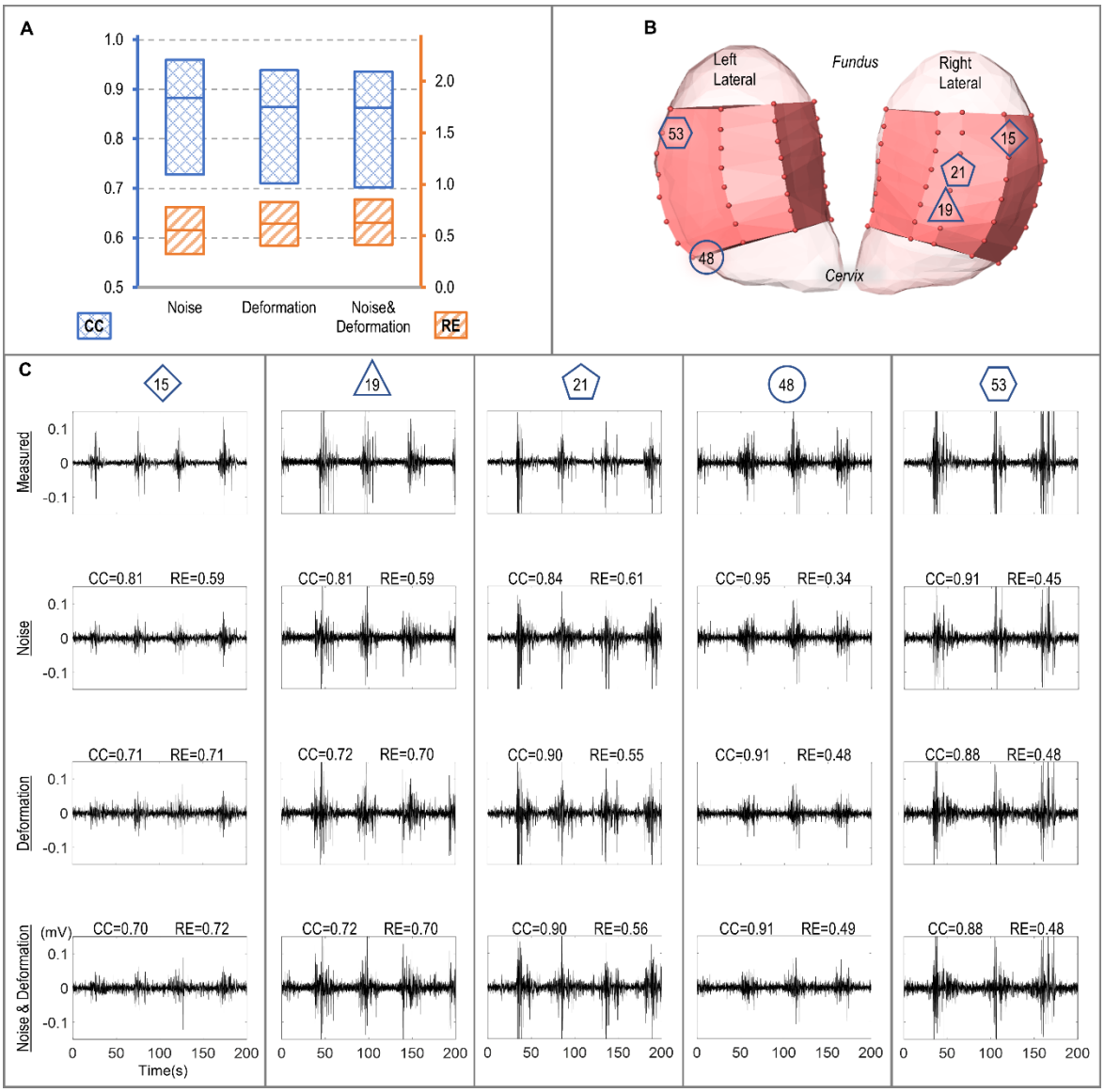

Figure 2.6: Evaluation of EMMI-reconstructed uterine surface electrograms in episode #1.
(A) Box plot of correlation coefficients (CCs, blue, diamond checkered pattern) and relative errors (REs, orange, diagonal pattern) comparing EMMI-reconstructed with measured uterine surface electrograms under the indicated conditions (N=52, see Data file S4). Horizontal lines indicate 1st quartile, median, and 3rd quartile. (B) Left and right lateral view of sheep uterus. The numbers differentiated by various shapes indicate the discrete uterine surface sites where measured and reconstructed uterine surface electrograms are compared in panel C. (C) Measured and EMMI-reconstructed electrograms (0-200 seconds) from the indicated sites. Analysis of all episodes are presented in Table 2.1 (N=595).

To summarize, across all eight episodes, median CC values were recorded as 0.85 [0.72, 0.95], 0.83 [0.69, 0.93], and 0.83 [0.68, 0.93] under conditions of noise, deformation, and combined noise and deformation, respectively. Corresponding RE values were 0.55 [0.36, 0.78], 0.62 [0.42, 0.86], and 0.63 [0.43, 0.87] under these same conditions (N = 595, refer to **Table 2.1**).

Collectively, these results support the capacity of EMMI to reliably reconstruct uterine electrograms based on body surface potential data, even when subjected to added noise, geometrical deformations, or a combination of both.

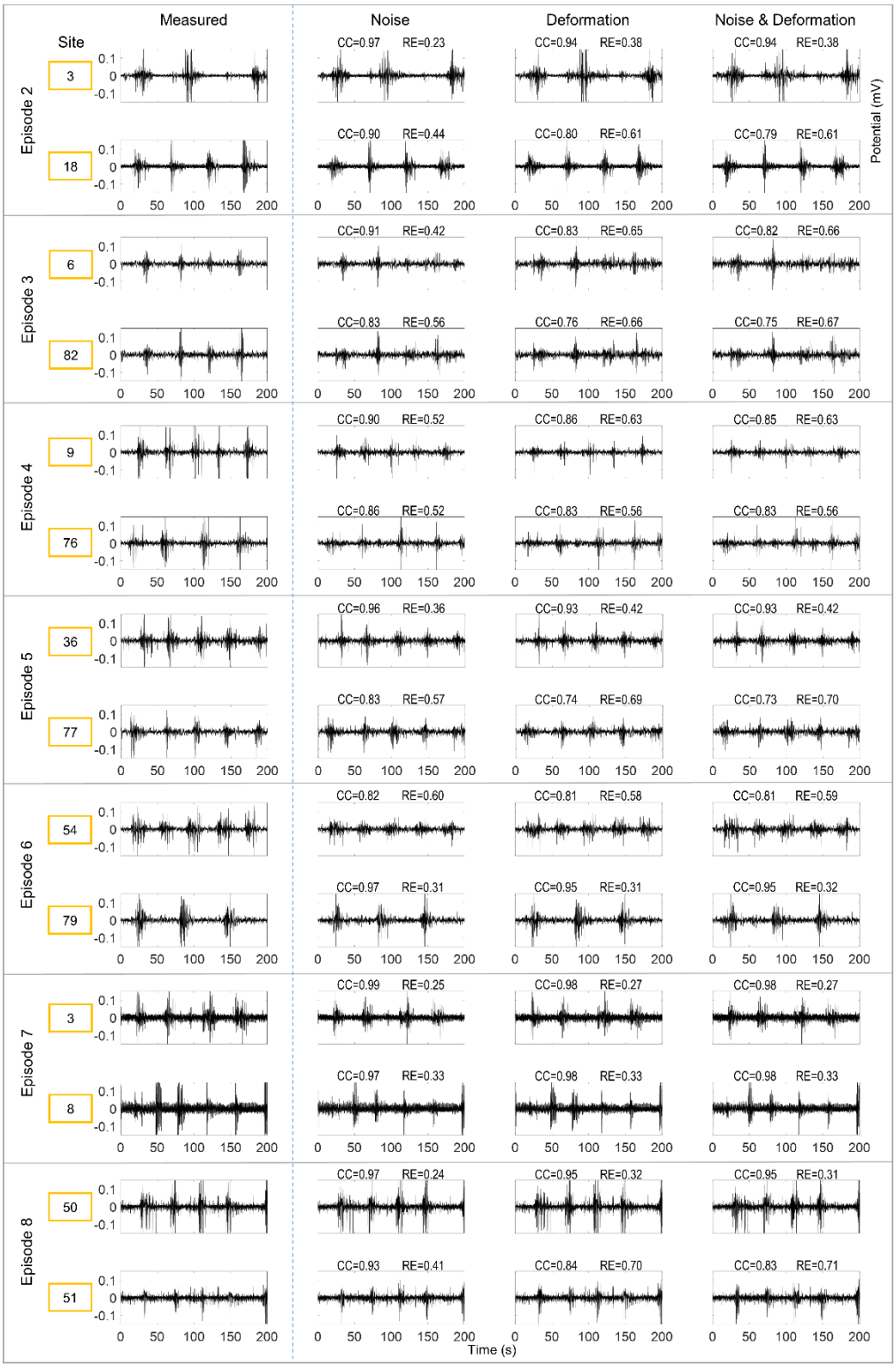

Figure 2.7: Measured and EMMI-reconstructed uterine surface electrograms in episode #2-8.
Correlation coefficients (CCs,) and relative error (RE) of the electrograms from the indicated sites were labeled. Analysis of electrograms from all sites in all episodes are presented in Table 2.1 (N=595).

2.9.2 EMMI potential maps

We subsequently analyzed potential maps, comparing directly measured uterine surface potentials to EMMI-reconstructed potentials under conditions of noise, geometrical deformation, and the combination of both. **Figure 2.8** illustrates three representative potential maps at distinct time frames, indicated by red arrows in the electrograms, during episode #1. The EMMI-reconstructed potential distribution patterns were similar to those measured directly on the uterine surface under all three conditions. In **Figure 2.8A**, potential distribution patterns denoted as A1, A2, and A3 in the measured maps were preserved in the EMMI-reconstructed maps under each condition. Spatial correlation coefficients (CC) for these entire maps were notably high (range: 0.87-0.93), while the spatial relative error (RE) was low (range: 0.38-0.49).

Quantitative analysis of 28,120 potential maps from eight episodes yielded CC values of 0.80 [0.71, 0.86], 0.78 [0.68, 0.85], and 0.77 [0.67, 0.84] and RE values of 0.59 [0.48, 0.73], 0.64 [0.52, 0.78], and 0.64 [0.53, 0.78] under conditions of noise, deformation, and combined noise and deformation, respectively (summarized in **Table 2.1**). These findings suggest that EMMI is capable of reconstructing accurate uterine surface potential patterns even when subjected to added noise, geometrical deformations, or a combination of both.

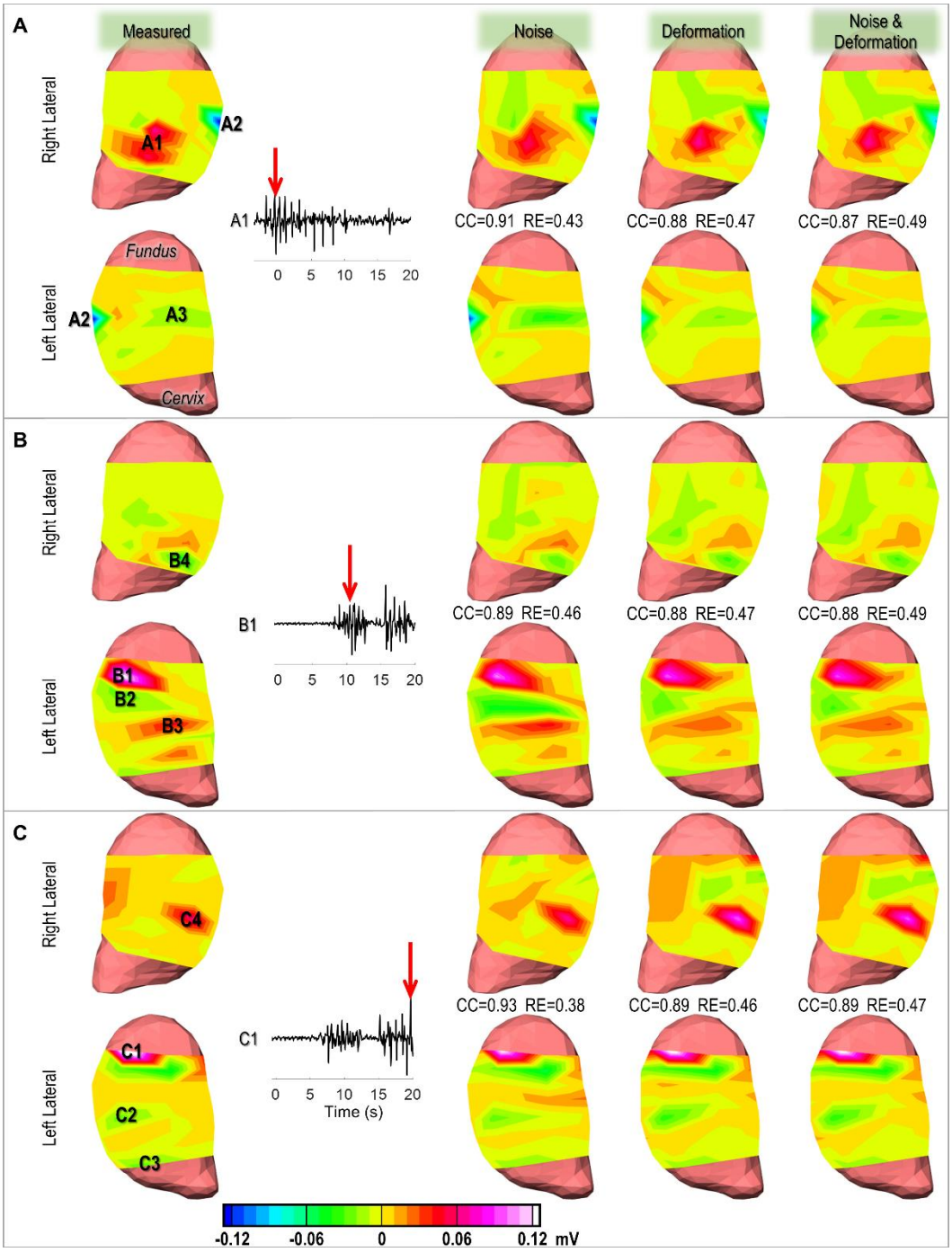

Figure 2.8: Evaluation of EMMI-reconstructed uterine surface potential maps during episode #1.
Measured potential maps and reconstructed maps with noise, deformation, or both noise and deformation shown at time instances (red arrows in electrograms) 0 seconds (A), 11 seconds (B), and 20 seconds (C). The electrograms shown were from sites A1, B1, and C1. CC, correlation coefficient; RE, relative error. CCs and REs shown on this figure were computed at their corresponding time instance. Analysis of all potential maps during contraction are presented in Table 2.1 (N=28120).

2.9.3 Isochrone maps

To evaluate the robustness of EMMI's reconstruction capabilities, isochrone maps were generated to represent the spatiotemporal electrical activation patterns of the uterus during defined observation windows (as per section **2.7.6**). The heat maps encoded the activation time at individual uterine sites, with warm and cool colors signifying early and late activation regions, respectively. **Figure 2.9** presents isochrone maps for two observation windows in episode #1: one spanning 0 to 59 seconds and another from 173 to 227 seconds.

In the first window (**Figure 2.9A**), early activation was observed along the fetal spine (maternal ventral) and at a smaller region at left lateral and maternal dorsal. This activation subsequently propagated to adjacent regions (yellow and then green in color coding). In the second window (**Figure 2.9B**), early activation was localized in three interconnected regions at the right lateral and later spread to the left lateral. Sites marked by black dashed circles and squares exhibited early activation in both observation windows.

EMMI-reconstructed isochrone maps maintained accurate activation patterns to the directly measured ones across all conditions. Quantitative metrics for the first and second observation windows were as follows: CC values of 0.96, 0.95, and 0.95 and RE values of 0.14, 0.14, and 0.14 under noise, deformation, and both, respectively, for observation window A; and CC values of 0.99 and RE values of 0.01 under all three conditions for observation window B. Aggregate analysis of 25 isochrone maps from 8 episodes yielded CC values of 0.99 [0.96, 1.00], 0.98 [0.95, 0.99], and 0.97 [0.94, 1.00] and RE values of 0.01 [0.00, 0.06], 0.02 [0.01, 0.08], and 0.03 [0.01, 0.08] under noise, deformation, and both conditions, respectively (summarized in **Table 2.1**).

These data support that EMMI reliably reconstructs isochrone maps even under conditions of noise and deformation.

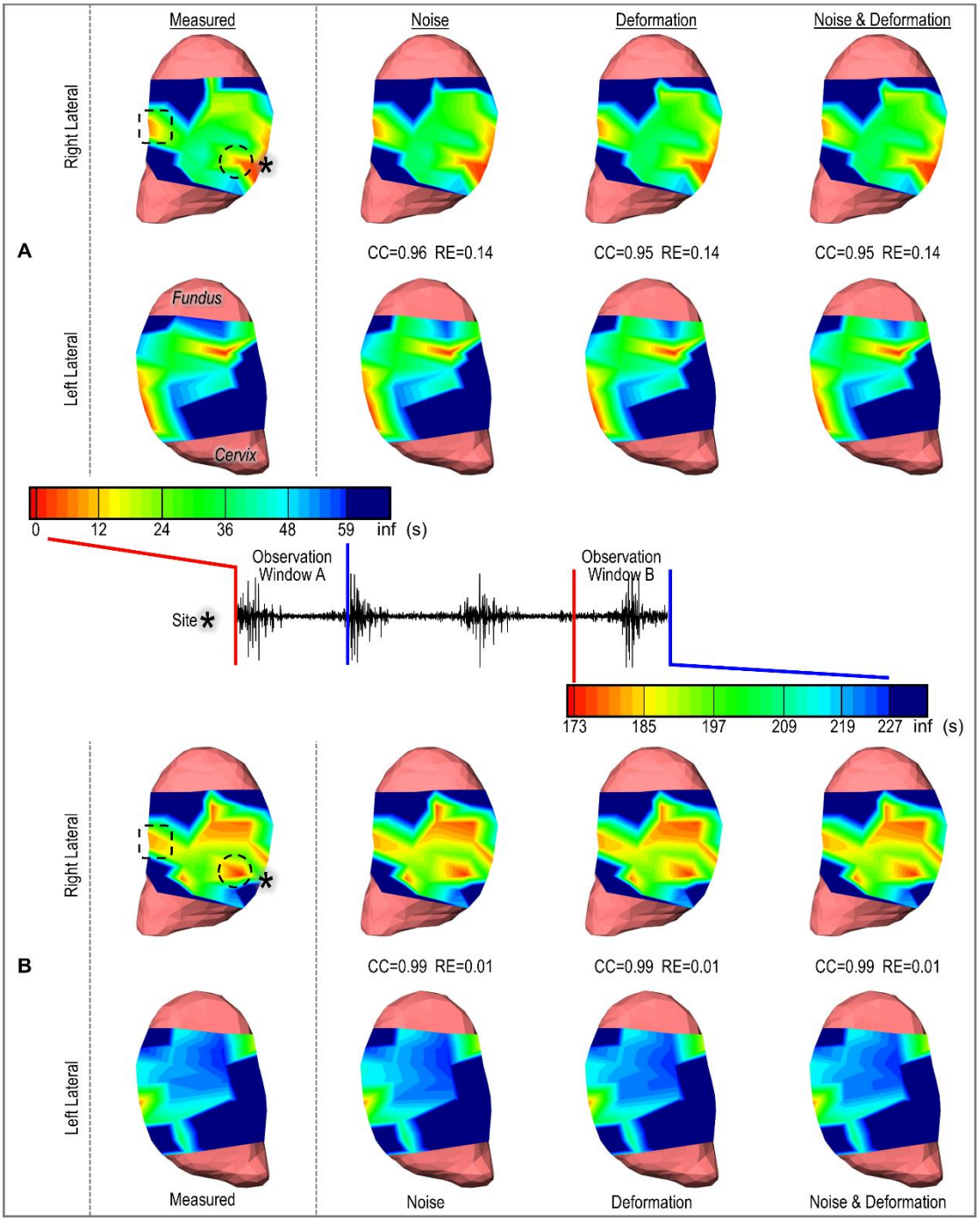

Figure 2.9: Evaluation of EMMI-reconstructed activation isochrone maps in episode #1.
Measured and EMMI-reconstructed activation isochrone maps with noise, deformation, or both noise and deformation are shown during observation window A (0–59 seconds, A) and observation window B (173 to 227 seconds, B). The electrogram represents the site marked with an asterisk. In the isochrone maps, red indicates the earliest activation, blue indicates the latest activation, and the darkest blue, labeled 'inf', denotes regions in which no activation was

recorded during the observation window. Black dashed circles and squares denote uterine surface areas that activated early in both windows. CCs and REs shown on this figure were computed at their corresponding observation windows. Analysis of all isochrone maps are presented in Table 2.1 (N=25).

2.10 Evaluation of EMMI feasibility

To assess the feasibility of EMMI for noninvasive mapping of uterine surface potentials, we examined data obtained from the body surface of four sheep. Each subject received a minimum of two oxytocin boluses prior to surgical intervention. Body surface electrical activity corresponding to uterine contractions was verified by two obstetricians (A.G.C., J.S.R.) and one veterinary surgeon (M.T.). EMMI was then employed to reconstruct the electrical patterns of three consecutive uterine contractions, utilizing both the measured body surface potentials and MRI-derived anatomical data. Detailed activation sequences are presented in **Figure 2.10**. An additional set of nine uterine contractions was similarly reconstructed, with the corresponding isochrone sequences displayed in **Figure 2.11**. These findings support the feasibility of EMMI for noninvasive imaging of uterine contractions.

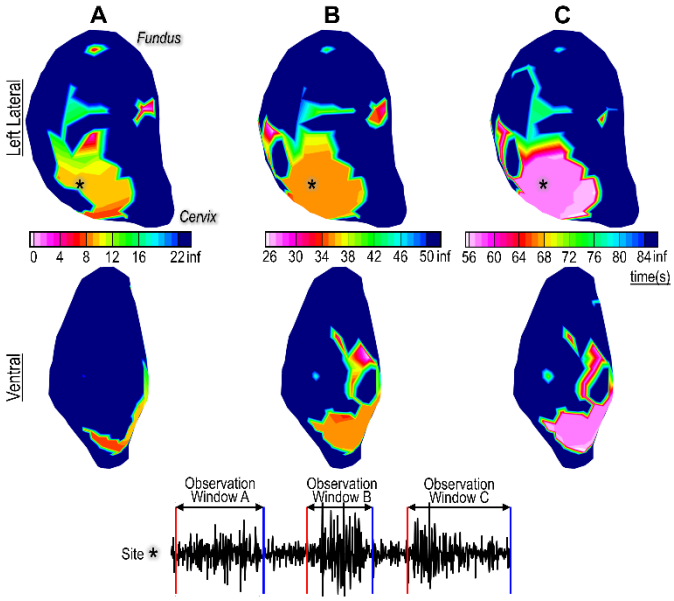

Figure 2.10: EMMI-reconstructed activation isochrone maps of oxytocin-induced contractions.
Three contiguous contractions (0–22 seconds, A), (26–50 seconds, B), and (56–84 seconds, C) mapped by EMMI. The EMMI-reconstructed electrogram is from the uterine surface site denoted by an asterisk. In the isochrone maps, light pink indicates the earliest activation, blue indicates the latest activation, and the darkest blue, labeled 'inf', denotes regions in which no activation was recorded during the observation window.

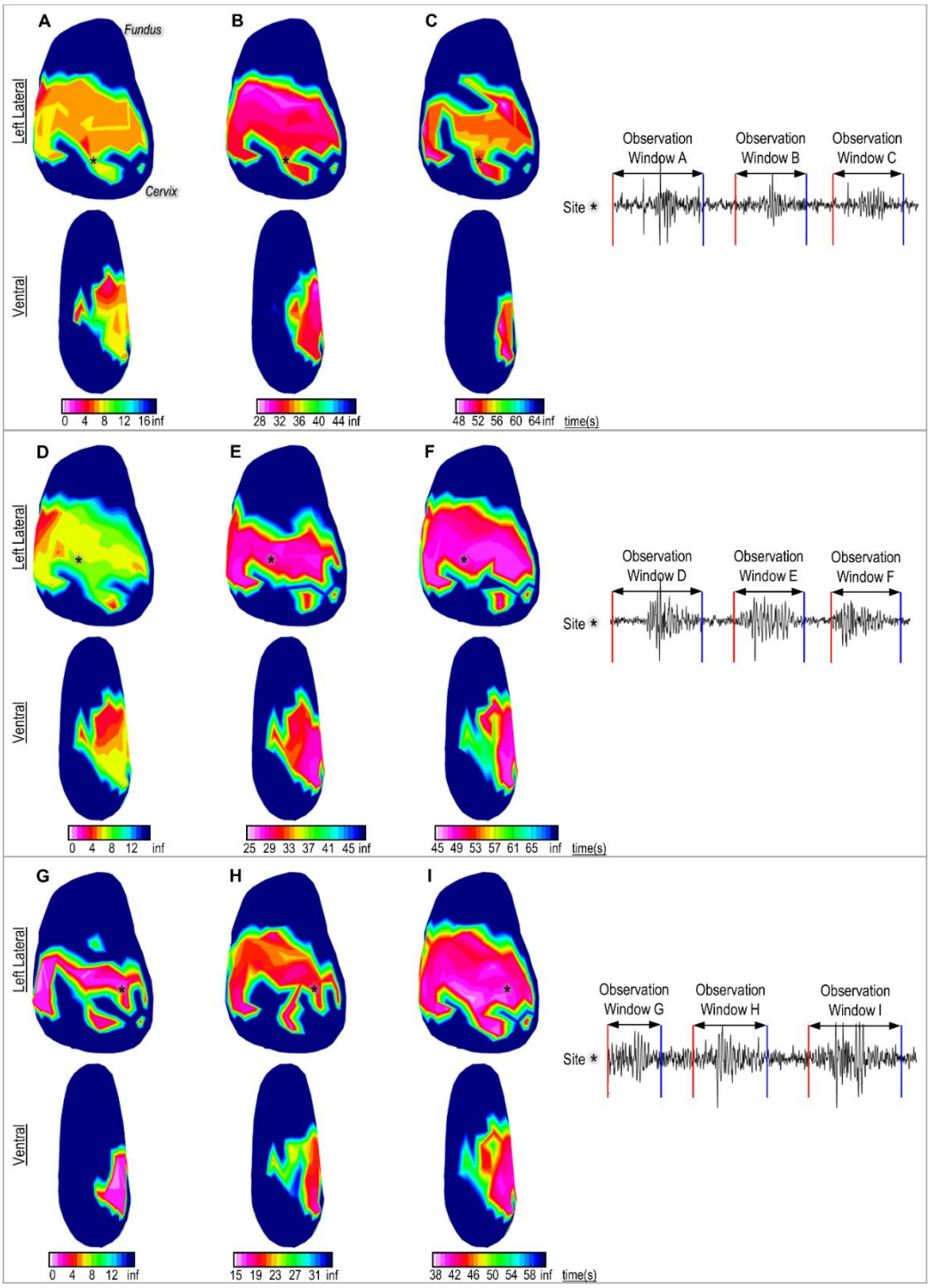

Figure 2.11: EMMI-reconstructed activation isochrone maps of 9 oxytocin-induced contractions.
Nine contractions (0–17 seconds, A), (28–46 seconds, B), (48–64 seconds, C), (0–14 seconds, D), (25–47 seconds, E), (45–70 seconds, F), (0–15 seconds, G), (15–33 seconds, H), and (38–60 seconds, I) were mapped by EMMI. The EMMI-reconstructed electrogram is from the uterine surface site denoted by a white asterisk. In the isochrone maps, light pink indicates the earliest activation, blue indicates the latest activation, and the darkest blue, labeled 'inf', denotes regions in which no activation was recorded during the observation window.

2.11 EMMI clinical development

In the clinical procedure for EMMI (**Figure 2.12**), magnetic resonance imaging (MRI) is conducted after placing up to 256 MRI markers on the abdominal and lumbar regions of the subject. During active labor, these markers are replaced with surface electrodes at the same locations, and multi-channel body surface potentials are synchronously recorded using a portable electrical mapping system. This recorded electrical data, in conjunction with MRI-derived geometrical information, is processed by EMMI software to generate uterine surface maps.

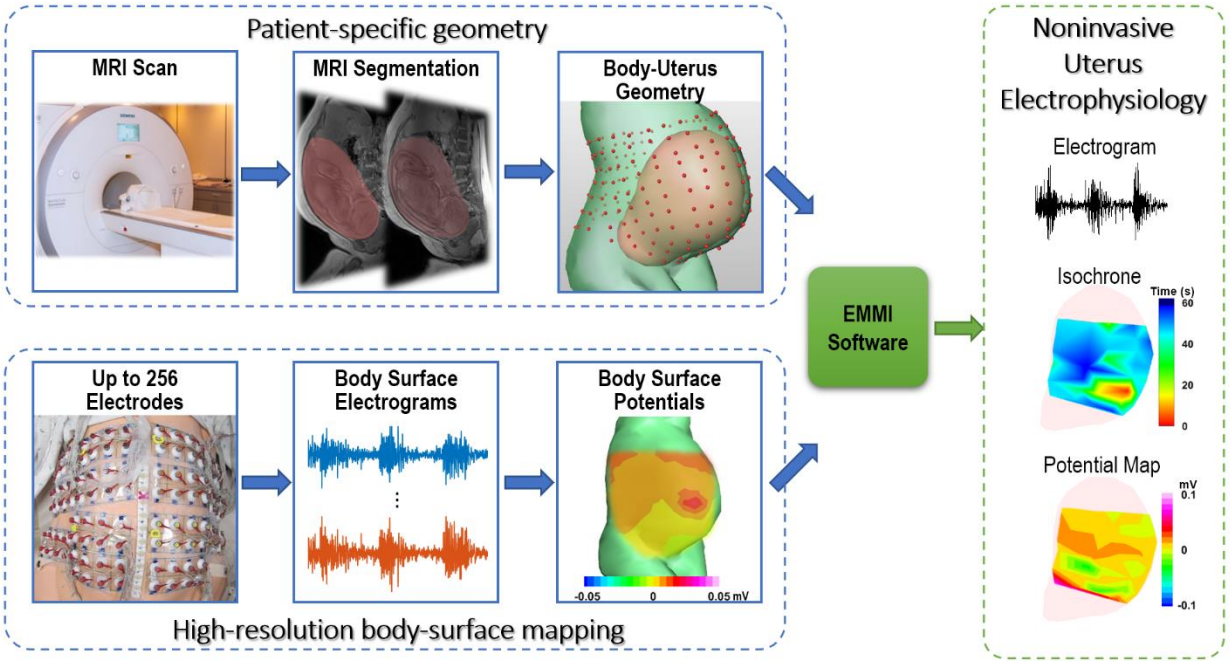

Figure 2.12: EMMI's clinical procedures flowchart

2.12 Discussion

The presented results strongly support the utility of EMMI as a viable, noninvasive method for imaging uterine electrical activity during contractions. We demonstrated that potential maps

generated by EMMI, based on body surface recordings, closely align with those obtained via direct electrode placement on the uterine surface. Furthermore, our computational models indicate that EMMI reconstructions remain accurate under clinically relevant variables such as maternal and fetal movements and electrical noise from adjacent equipment. Lastly, we verified the clinical translatability of the EMMI approach by using sheep's body-surface electrical recording and MRI-derived anatomical data for noninvasive electrical imaging. Collectively, these findings support the accuracy, robustness, and feasibility of EMMI for mapping uterine electrical activity during contractions.

Multiple factors support the safety of EMMI for application in pregnant women. MRI technology has a well-documented record of safe use in evaluating obstetrical, placental, and fetal conditions during the second and third trimesters of pregnancy[34,54]. Although concerns have been raised regarding exposure to static and gradient magnetic fields, radio frequency radiation, heating of sensitive tissue[55], and acoustic environment[56], a comprehensive cohort study involving over 1.4 million pregnant women found no significant association between first-trimester MRI and adverse outcomes such as stillbirth, neonatal death, congenital anomalies, neoplasms, or hearing loss[36]. In terms of electrical recording, the setup ensures patient safety through a battery-powered recording box and optical isolation between the recording unit and the computer interface. The system is also designed to restrict leak currents to less than 1 μA[42,43], significantly below the 10 μA safety threshold. Moreover, a built-in safety feature automatically deactivates the system if leak currents exceed specified safety limits[43].

EMMI offers several advantages over traditional electromyography (EMG) that involves direct uterine surface measurements. Most significantly, EMMI operates noninvasively, circumventing the necessity for surgical procedures that limit uterine EMG to animal studies.

Additionally, EMMI achieves a higher spatial resolution compared to EMG due to the limitations on the number of electrodes that can be surgically implanted on the uterine surface. In our pacing study, a 64-electrode sock was used for direct measurement; however, EMMI allowed for the assessment of approximately 180 or more reconstruction points. This resulted in a reduced mean distance between reconstruction points, enhancing the spatial resolution and yielding more physiologically plausible potential distributions. Unlike EMG-generated potential maps that are susceptible to interpolation artifacts, EMMI-generated maps display an ellipsoid shape, indicative of anisotropic electrical propagation and aligned with findings from studies on isolated rat uterine tissue[57]. Lastly, while EMG's surgical constraints preclude comprehensive uterine mapping, EMMI offers complete three-dimensional electrical mapping and activation pattern of the uterus during contractions.

We noted a few potential limitations in this first EMMI study. Firstly, due to the low electrode density in the uterine sock employed, we achieved only partial uterine coverage, thereby providing a less detailed electrophysiological data on sheep uterine contractions.

Secondly, our computational methods presumed a homogenous volume conductor between the body surface and uterus, devoid of any other electrical sources. Similarly, previous ECGI studies found that ignoring inhomogeneity minimally affected the reconstructed signal morphology[47,48]. While this assumption led to comparable activation time and potential patterns between direct measurements and EMMI reconstructions, anatomical inhomogeneities, such as bone, fat, and skeletal muscle, could introduce inaccuracy in the magnitude of EMMI's reconstructed potentials. Future work will be aimed at modeling the effects of inhomogeneity to improve EMMI reconstruction. Thirdly, the current analysis is limited to electrical burst propagation and does not include electrical spike propagation[58]. Future investigations should explore EMMI’s capability to

accurately reflect a single spike propagation at high temporal and spatial resolutions. Fourthly, to stabilize EMMI's inverse solutions, we employed conventional Tikhonov regularization with parameters derived via the Composite Residual and Smoothing Operator. While effective for analyzing cardiac maps in ECGI[26,37], these parameters for EMMI remains less optimized, given the difference in signal morphologies and amplitudes between cardiac and uterine measurements. Further research is needed to fine-tune these regularization parameters for EMMI-specific applications. Finally, our robustness analysis was restricted to the effects of Gaussian noise and geometrical deformation. Future work will expand this analysis to include various noise types and deformation severities, thereby providing a more comprehensive assessment of EMMI's robustness.

The potential for EMMI to quantify the propagation velocity of single electrical spikes in the myometrium merits more exploration. Previous literature has reported that propagation velocity is linked to increased expression of the gap junction protein connexin-43, augmented intercellular coupling, and enhanced uterine synchronization and maturation[59–62]. Consequently, propagation velocity may serve as a biomarker for labor progression[21,62]. While regional propagation velocity has been invasively quantified on the uterine surface of rats and guinea pigs[23,24], global assessments of propagation velocity covering the entire uterus are absent from the current literature. In humans, prior attempts to measure propagation velocity have employed limited electrode arrays covering a 2.8 × 2.8 cm or 8 × 8 cm area on the body surface[21,63,64]. However, the propagation velocity measured from the maternal body surface may be inaccurate, especially when the uterine surface electrical wave front propagation is not parallel to the axis of a measuring electrode pair on the body surface[58]. Given EMMI's ability to accurately reconstruct

isochrone maps across the whole uterus, it is plausible that EMMI could be adapted to measure propagation velocity.

Another important aspect of labor that could be investigated with EMMI is the characterization of "pacemakers"[65–67] that initiate contractions in a coordinated fashion during active labor to generate sufficient intrauterine pressure to expel the fetus. While early hypotheses proposed a single uterine pacemaker[68] similar to the heart's sinoatrial node, such node has not yet been found after decades of research[58,69]. Alternative hypotheses propose the existence of multiple pacemakers dispersed throughout the uterus[66,67,70–72]. One of the plausible working models is that each pacemaker paces a region of myometrium in the uterus, leading to gradually increased intrauterine pressure, which in turn initiates other pacemaker activities at different locations[70,73]. In support of this hypotheses, our sheep-based EMMI data indicated early activation at diverse sites on the uterine surface within a single observation window. Moreover, Magnetomyography (MMG) studies utilizing superconducting quantum interference devices (SQUIDs) for measuring the magnetic signals during contractions have yielded additional evidence consistent with the multiple pacemakers model[14,15,74]. Future human-based EMMI investigations will prioritize the localization and quantification of these pacemakers and explore their correlation with various stages of labor progression.

Chapter 3： Development and validation of placenta-specific diffusion basis spectrum imaging (DBSI)

In this chapter, we present the development and validation of a novel imaging technique—placenta-specific diffusion basis spectrum imaging (DBSI)—by assessing its correlation with histological data in experiments conducted on small *ex vivo* placental tissue samples.

3.1 Placenta

The human placenta serves as a critical, temporary organ responsible for nutrient supply to the fetus, exchanges of oxygenated blood for deoxygenated blood, pregnancy-supporting hormone production, and modulation of maternal and fetal immune responses. Placental inflammation can activate the maternal and fetal immune systems to varies degrees depending on the severity of inflammation[75]. A successful pregnancy requires initiation and progression of physiologic inflammation to facilitate embryo implantation, placentation, membrane rupture, cervical ripening, and labor, which are synchronous with fetal maturation[76,77]. This physiological state is intricately balanced by the placenta, which regulates immune tolerance and suppression in both maternal and fetal systems[75].

However, early or excessive inflammation, asynchronous with fetal development, can induce preterm labor and fetal injury[76]. Placental immune cell infiltration and inflammation is a leading cause of such outcomes[78], with 50% of spontaneous preterm births associated with maternal infections, which are often asymptomatic[79,80]. The infection and accompanying inflammation could go undiagnosed prior to onset of preterm labor and standard blood test lacks

specificity at placenta organ level. On the other hand, most knowledge on placental immune response originates from animal models or histological analysis of *ex vivo* human specimens. These methods provide limited translational insights and only offer a snapshot of pathological conditions post-delivery.

To comprehensively understand placental immune processes and inspire therapeutic interventions, it is important to investigate these mechanisms from early pregnancy stages. Currently, no technology exists for non-invasive, real-time assessment of placental immune responses *in vivo* during the entire length of gestation.

3.2 Techniques to evaluate placenta

Several imaging modalities have shown promise for studying placental immune response, yet inherent limitations restrict their applicability for *in vivo*, real-time analysis in human pregnancies. Optical-based techniques, including intravital microscopy, confocal microscopy, and two-photon microscopy, have demonstrated utility for cellular-level inflammation assessment in animal models[81]. However, the requisite injection of fluorescent dyes renders these methods unsuitable for human pregnancy. Positron emission tomography (PET) is another viable option for imaging immune responses but is precluded due to the requirement for radiative tracers, which contravene safety protocols for pregnant women. Magnetic resonance imaging (MRI) techniques that could potentially elucidate inflammation necessitate contrast agents. However, the use of these agents is proscribed during pregnancy, given a recent study associating their usage with elevated risks of stillbirth or neonatal death[36].

3.3 Inspiration from DBSI in brain

To overcome limitations inherent in existing technologies for the assessment of placental immune response, this study leverages an noninvasive MRI method called diffusion basis spectrum imaging (DBSI). Previously validated for quantitative imaging of neuroinflammation in multiple sclerosis[82], DBSI decomposes diffusion MRI signals into components attributable to water molecules in discrete environments—restricted water in intracellular space, hindered water in the extracellular matrix, and freely moving water molecules. An important advantage of DBSI is that it will not require any dye or contrast agent and MRI without contrast agent has shown being safe to use during pregnancy[34–36].

Inspired by the utility of DBSI in neurological applications, we adapted this methodology to develop a placenta-specific multi-tensor DBSI model. This imaging tool holds significant promise for the quantitative analysis of placental immune response during pregnancy, thereby informing potential clinical interventions and assessing their efficacy in mitigating pathological inflammation.

To validate the utility of placenta-specific DBSI, we conducted *ex vivo* MRI studies on human placental specimens. Our central hypothesis posits a correlation between DBSI-derived metrics—specifically, the cell fraction (the percentage of the diffusion signal attributed to intracellular water) and the apparent diffusion coefficient (ADC) attributable to intracellular water—and histological markers. Validation was achieved by correlating these DBSI metrics with positive nuclei staining in hematoxylin and eosin (H&E) and positive staining in immunohistochemistry (IHC).

3.4 Experiment design

3.4.1 Patient enrollment criteria

We designed the following patient enrollment criteria, and all the following procedures were approved by the Washington University in St. Louis Human Research Protection Office (HRPO: 201707152, 202006021).

For this study, patients were eligible if they meet the following criteria:

Inclusion criteria

1. Singleton pregnancy with obstetric care and intention to deliver at Washington University in St. Louis
2. Multiparous
3. No identified fetal anomalies
4. For term group, history of one or more prior deliveries at 37 weeks or after, no history of preterm birth
5. For pre-term group, history of one or more prior spontaneous preterm births at <34 weeks

Exclusion criteria

1. Multiple gestation (incidence of multiple gestation is small, and mechanisms for PTB are thought to differ from those of singletons)
2. Nulliparous women (lack of obstetric history affects both risk of PTB and recommended medical interventions)
3. Contraindications to progesterone therapy (precludes inclusion in pre-term group)
4. Major fetal anomaly (affects counseling and management)
5. Contraindication to MRI (prevents participation in the study protocol)

3.4.2 *Ex vivo* imaging of placental tissue blocks

Ten placentas from uncomplicated deliveries were stored at 4 °C for up to 24 hours, five of which from normal term delivery without pathological legion and five of which from preterm delivery. Among them, three specimens have pathological chorioamnionitis. A specimen (10 × 10

mm × placental thickness) from each placenta was rinsed with phosphate-buffered saline (PBS) to remove large blood clot to avoid MR imaging artifacts due to high iron concentration in blood.

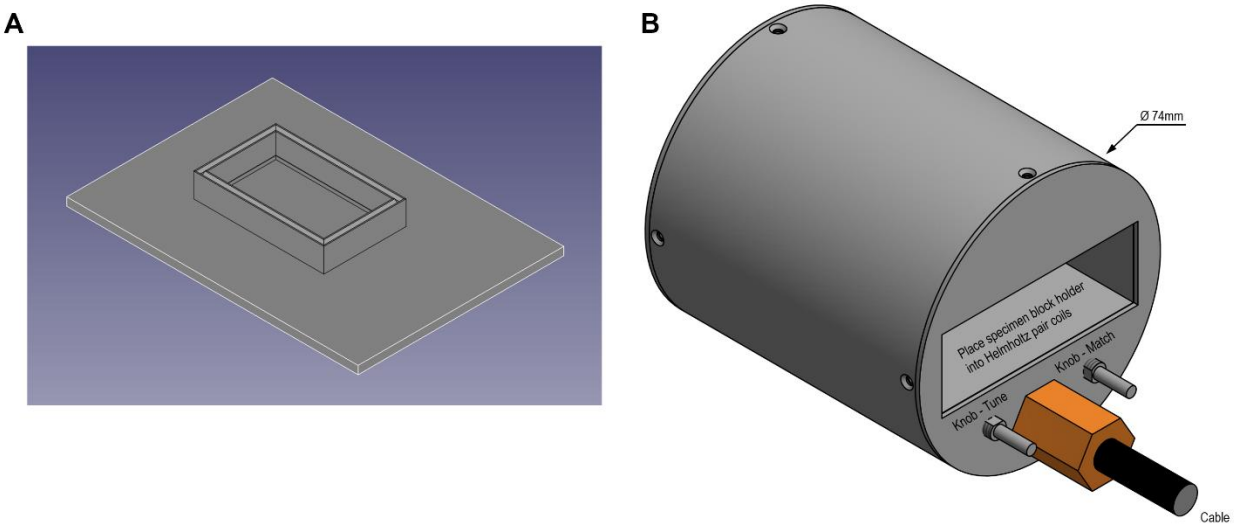

Figure 3.1: Custom cervix specimen holder and custom Helmholtz pair coil.

A custom-design specimen container (**Figure 3.1**) was 3D printed (Form Labs, Form 2, RS-F2-GPCL-04 clear resin). The specimen was embedded in 2% agar gel (**Figure 3.2B**) (Sigma, SKU-0504D-100G) in the specimen container at approximately 40°C and quickly cool down to room temperature. The container was placed in the temperature-controlled (at 20 °C) MRI scanner room for 30 minutes to allow temperature to be equalized to ambient temperature. The specimen container was then inserted into a custom-made Helmholtz pair coil (**Figure 3.1**, Extend MR, LLC). Several scout images were acquired with a Varian 11.7T MRI, and the specimen container was adjusted to align the MRI center coronal plane with the post-MRI bisection plane (alignment marking engraved in the container). The specimen was then imaged using 2D spin-echo sequence for both T2 images and diffusion image series with up to 74-direction diffusion encoding (**Table Appx. 1**) at the same resolution (TR = 1000 ms, TE = 32 ms, max b = 4500 s/mm^2, voxel = 0.25

× 0.25 × 1 mm). After imaging, the specimen was precisely bisected along the plane of imaging (**Figure 3.2C**) and fixed in 10% neutral-buffered formalin for a week. One half of the specimen was processed into paraffin. Slide-mounted 5 µm histologic sections were stained with hematoxylin & eosin (H&E) and DAB immunohistochemistry (CD4 antibody, hematoxylin counterstain) and digitized (20× magnification, Hamamatsu NanoZoomer HT). The nuclei density map (**Figure 3.2D**) was computed by segmenting hematoxylin staining of nuclei and then registered to the corresponding MR images.

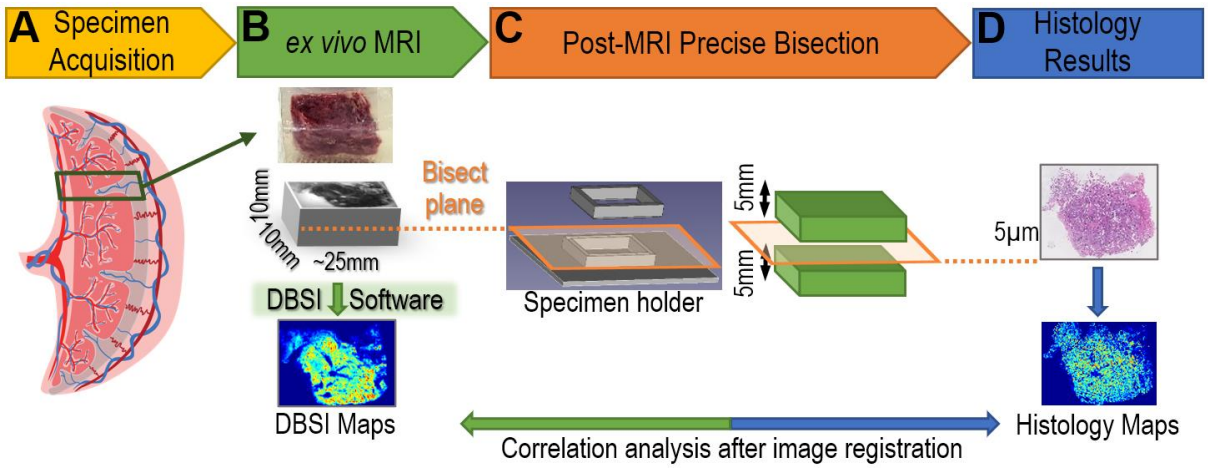

Figure 3.2: Validation scheme for placenta-specific DBSI using *ex vivo* specimen.
(A) A specimen (10 × 10 mm × thickness) was dissected from chorionic plate to basal plate from a placenta after the delivery (B) The specimen was embedded in 2% agar gel and imaged with a Varian 11.7T MRI, using DBSI sequence. DBSI maps were computed by in-house placenta optimized DBSI software (C) After MRI, the specimen was precisely bisected along the plane of imaging. (D) the specimen was fixed in formalin and embedded into paraffine. The stained slide-mounted 5µm histologic sections were digitized and converted to histology maps.

3.5 Computational methods

3.5.1 Monte-Carlo simulation of water diffusion in spherical cell model

The boundary condition at the cell membrane for water molecules was specular reflection. The membrane structures inside the cell (e.g., nuclear membranes) were neglected in the modelling. The sphere model was scaled to a series of radii from 6 μm to 15 μm to mimic the size of all cells in placenta. Each model had a fixed density (10 counts / μm^3) of random seeds (representing water molecules).

The simulated diffusion MRI signal is based on the same diffusion gradient (*b-values* and *b-vectors*) used in *in vivo* and *ex vivo* MRI. The in-house Monte-Carlo simulation software (written in MATLAB) is designed to according to the following physics equations.

$$l = \sqrt{6 * D * dt} \tag{3.1}$$

$$d\phi = \gamma G(t) * r(t) * dt \tag{3.2}$$

$$S = \sum_{j=1}^{N} Re(\exp(i\phi_j)) \tag{3.3}$$

Where l is the discretized stepsize for water molecule diffusion. D is diffusion coefficient with any restriction in certain temperature. dt is the discretize time step in simulation and equal to 1ms. γ is gyromagnetic ratio. $r(t)$ represent the full trajectory of water molecule random within simulation duration. $G(t)$ is the bipolar diffusion gradient. ϕ_j is the dephase of j^{th} water molecular. S is the normalize simulated diffusion signal.

Figure 3.3 displays the relationship between diffusivity and cell diameter as derived from Monte-Carlo simulations. Informed by these results, we proceed to construct isotropic tensor models in the subsequent section.

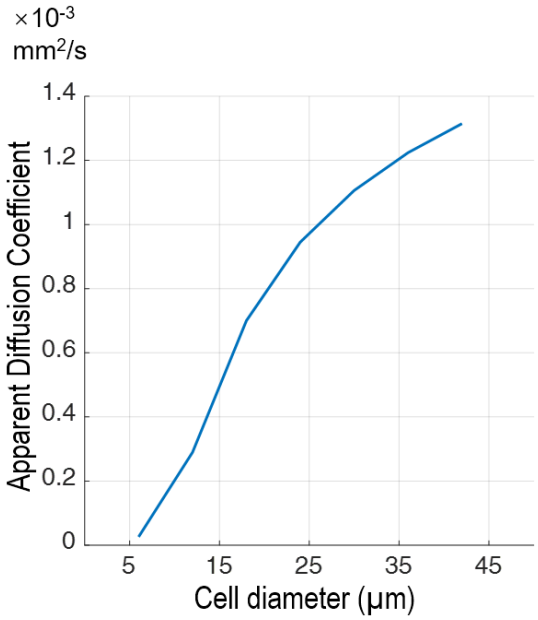

Figure 3.3: Monte-Carlo simulation of the ADC (diffusivity) based on cell diameter.

3.5.2 Multi-tensor DBSI model for placenta

We adapted the principles of diffusion basis spectrum imaging[83], which models diffusion weight MRI signals as a linear combination of multiple anisotropic and isotropic tensors that are tailored to microstructures of the specific organ and disease model. Here, we developed placenta-specific tensor models for imaging placental inflammation. In **Equation 3.4** and **Figure 3.4**, the total diffusion weight signal in an image voxel could be decomposed to two parts: summation of signals contributed by the linear combination of all anisotropic and isotropic tensors.

$$S_k = \underbrace{\sum_{i=1}^{N_{Aniso}} f_i e^{-|\vec{b}_k|\cdot\lambda_{\perp i}}\, e^{-|\vec{b}_k|\cdot(\lambda_{\parallel i}-\lambda_{\perp i})\cdot\cos^2\psi_{ik}}}_{\text{Signals from anisotropic tensors}} + \underbrace{\sum_{j=1}^{N_{Iso}} f_j e^{-|\vec{b}_k|D_j}}_{\text{Signals from isotropic tensors}} \quad (k = 1,2,\dots,K) \qquad (3.4)$$

Total signals

where S_k and $|\vec{b}_k|$ are the diffusion weighted signal at each voxel and *b-value* of the k^{th} diffusion gradient respectively. N_{Aniso} and N_{Iso} represents the number of anisotropic and isotropic tensors respectively. ψ_{ik} denotes the angle between the k^{th} diffusion gradient and the principal direction of the i^{th} anisotropic tensor. $\lambda_{\parallel i}$ and $\lambda_{\perp i}$ are the axial diffusivity and radial diffusivity of the i^{th} anisotropic tensor respectively. f_i is the signal intensity fraction for the i^{th} anisotropic tensor, while f_j is the signal intensity fraction for the j^{th} isotropic tensor. D_j denotes isotropic diffusivity of j^{th} isotropic tensor.

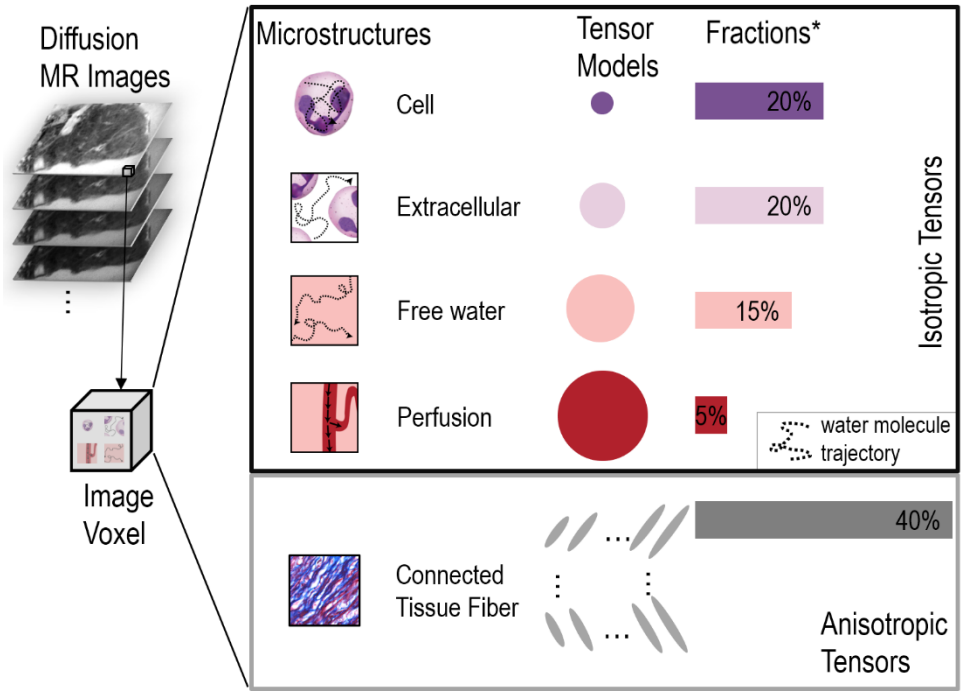

Figure 3.4: The design and physiological implication of isotropic tensor models in placenta optimized DBSI. In an image voxel, we designed anisotropic tensors to represent water diffusion in connected tissue fibers and four categories of isotropic tensors to represent water diffusion in cell, extracellular space, free moving water and perfusion. (*Fractions of each tensor model are only for demonstration.)

The principal directions ψ_{ik} of the anisotropic tensors were designed based on a set of uniformly distributed in 3D space[84] and the axial diffusivity and radial diffusivity of anisotropic tensors were designed based on the results in DBSI for inflammatory demyelination with minor adjustment[83]. The detailed anisotropic tensor design is described in the **Table 3.1**.

Table 3.1: Anisotropic tensor models for placenta-specifc DBSI.

Diffusivity $\times 10^{-3}$ mm^2/s	Tensor 1	Tensor 2	Tensor 3	Tensor 4	Tensor 5	Tensor 6	Tensor 7	Tensor 8	Tensor 9
Radial Diffusivity (RD)	0.1	0.1	0.1	0.5	0.5	0.5	0.8	0.8	0.8
Axial Diffusivity (AD)	1.0	1.5	2.0	1.5	1.75	2.0	2.0	2.5	3.0
AD / RD	10	15	20	3	3.5	4	2.5	3.13	3.75

Because inflammation often involves changes in cellular matrix and microstructure, which are related to isotropic diffusions, the focus is on the design of isotropic tensors. We designed four categories of isotropic tensors (**Figure 3.4**) to describe the water diffusion in cells, in extracellular spaces and free water diffusion and perfusion (only applicable to *in vivo* DBSI) in an image voxel. We designed restricted isotropic diffusion tensors (ADC = $0 – 0.4\times10^{-3}$ mm^2/s for *ex vivo* specimen at 20 °C; ADC = $0 – 0.6\times10^{-3}$ mm^2/s for *in vivo* at 37 °C) for water modules in cell based on the result of Monte-Carlo simulation of the ADC (diffusivity) of cell diameter below 15 μm. We designed tensors for free water based on common experiment values by Easteal et al and Holz et al[85,86]. The detailed isotropic tensor design is described in **Figure 3.5**.

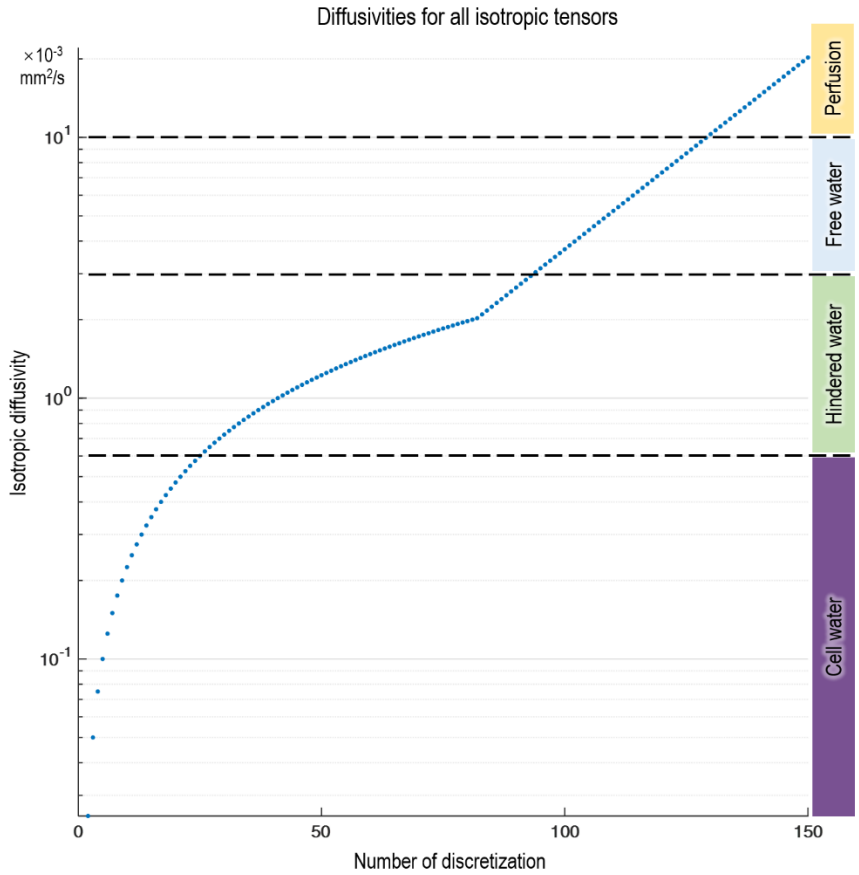

Figure 3.5: Isotropic tensor models for placenta-specifc DBSI.

3.5.3 Histology quantification

A 20× bright field image was trimmed to smaller tiles (5000 × 5000 pixels) for faster histology processing and stitched together after the processing. We first employed Orbit Image Analysis[87] to quantify positive stains of cell nuclei. Researchers with histology training first delineated about a dozen of typical cell nuclei and regions of background and villi tissue (eosin stain) on one tile image to train the Orbit tissue classifier based on chromatic information. Then, all image tiles were classified to a binary map of positive nuclei stain by the trained classifier. The binary maps then underwent in-house MATLAB program to filter large areas spill over hematoxylin stain which does not represent cell nuclei. The filtered binary maps were then converted to the nuclei density maps by calculating percentage of nuclei area per 50 × 50 pixels area. These tiles of nuclei density map were than stitched together and downsampled to 10 times of the MR image plane resolution for the next step of image registration. The CD4+ immunohistochemistry fraction maps were processed in the same pipeline by classifying chromatic information of DAB stain.

3.5.4 Image registration

The specimen contours from the nuclei density map, CD4+ fraction map and T2 MR image were delineated in 3D slicer[88]. An Affine linear registration guided by fiducial landmarks were performed to register the nuclei density map and CD4+ fraction map to the T2 MR image. After the registration, the histology maps were down sampled to the same resolution as the DBSI-derived

maps. In the correlation analysis, both DBSI and histology maps were further downsampled to clinical MRI in plane resolution of 3mm.

3.6 Results

3.6.1 Evaluation of DBSI in *ex vivo* specimen from preterm cohort

To compare cellularity in the histology and DBSI images, we segmented the H&E images and converted the positive stain of nuclei to the nuclei density maps (**Figure 3.6B**). In the DBSI images, we calculated cell fraction as the percentage of diffusion signal contributed by intracellular water over total diffusion signals. Qualitatively, the DBSI cell fraction maps and the histological maps showed similar spatial distribution of cellularity in placenta villi. To quantitatively compare the DBSI-derived cell fraction and histological nuclei density maps, we downsampled the maps and performed correlation analysis by comparing the mean values in 3 × 3 mm regions. The DBSI-derived cell fractions correlated with histological nuclei densities (**Figure 3.6D**).

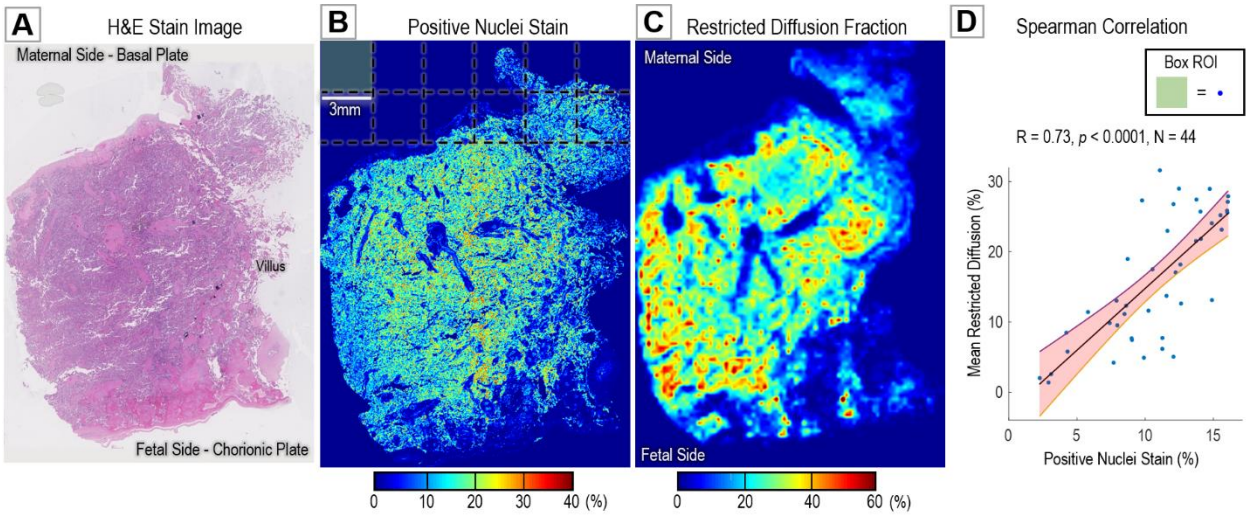

Figure 3.6: Correlation between histologically and PII-derived cellularity in preterm cohort.
(A) Brightfield image of H&E-stained cross-section of a block of placental specimen. (B) Positive hematoxylin (nuclei) stain fraction map derived from the H&E image in A. (C) PII-derived restricted isotropic diffusion fraction reflecting cellularity fraction. (D) Spearman's correlation plot of positive hematoxylin stain and restricted diffusion fraction. Each blue dot represents a ROI.

3.6.2 Evaluation of DBSI in *ex vivo* specimen with chorioamnionitis

In a small cohort presenting with chorioamnionitis, we utilized both H&E and CD4+ immunohistochemistry images to investigate elevated inflammation in placental villi. CD4+ staining was segmented and transformed into positive stain density maps (**Figure 3.7F**). In DBSI images, the apparent diffusion coefficient for cells (cell-ADC) was calculated as a weighted average over varying cell sizes. For quantitative comparison between DBSI-derived cell fractions and histological nuclei density maps, we performed downsampling followed by correlation analysis within 2.5 × 2.5 mm regions, comparing mean values. The results indicate that DBSI-derived cell fractions correlate with histological nuclei densities (**Figure 3.7D**), while DBSI-cell ADC correlates with CD4+ stain density maps (**Figure 3.7H**).

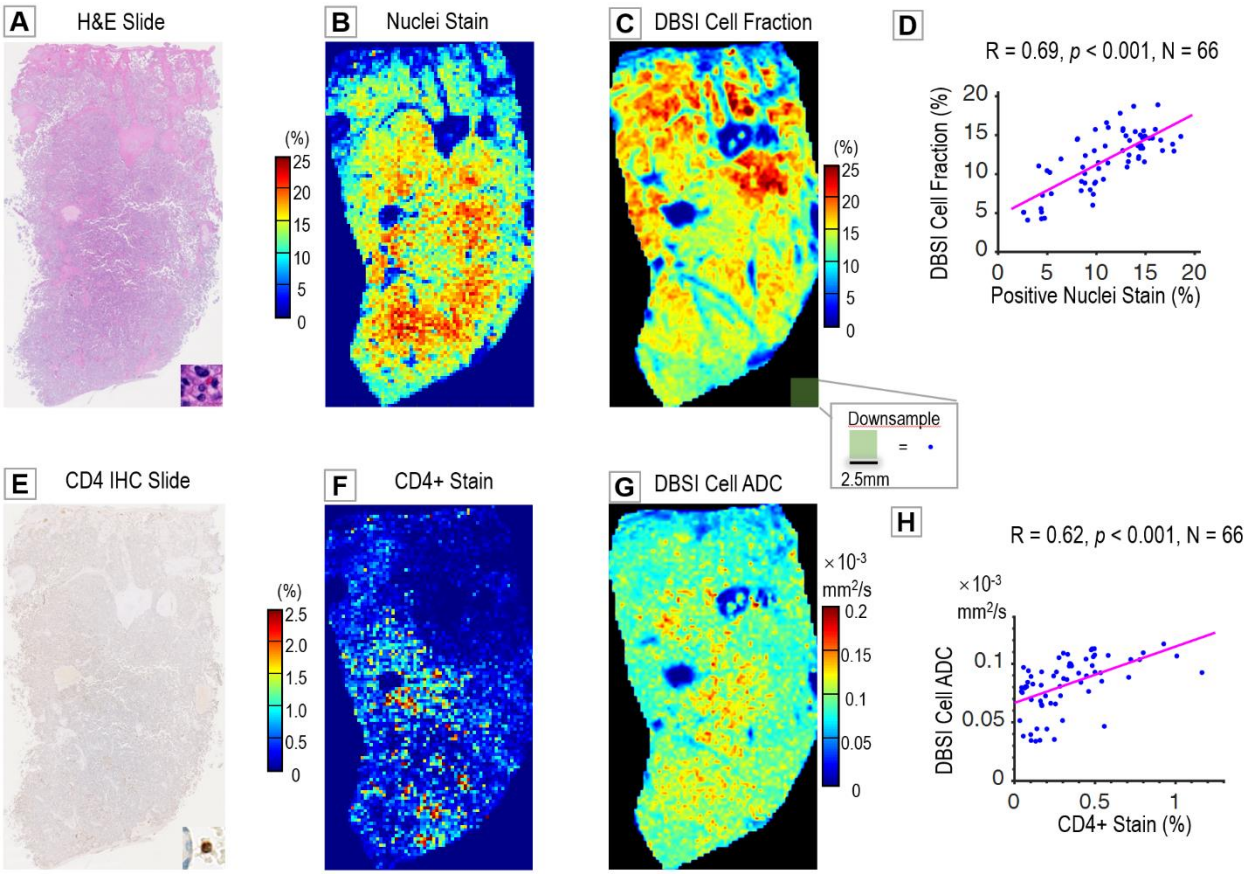

Figure 3.7: Correlation between histologically and PII-derived cellularity in chorioamnionitis cohort.
Brightfield image of (A) H&E-stained, (E) CD4+ stained, cross-section of a block of placental specimen. (B) Positive nuclei stain fraction map. (C) DBSI-derived cell fraction. (F) CD4+ stain fraction map. (G) DBSI-derived cell ADC. Spearman's correlation between: (D) positive hematoxylin stain and DBSI-cell fraction; (H) CD4+ stain and DBSI-cell ADC. Each blue dot represents a ROI.

3.7 Discussion

Our findings confirm the feasibility and validity of employing DBSI-derived imaging for assessing both the severity and spatial distribution of placental inflammation. This was corroborated by correlating DBSI-derived cell fractions with total cell nuclei stain fractions in H&E histology and DBSI-derived cell-ADC with CD4+ staining in immunohistochemistry, respectively. CD4, present on helper-inducer T cells, serves as a common metric for quantifying

levels of placental inflammation. The DBSI-derived cell-ADC exhibited a correlation with CD4+ staining in cases clinically diagnosed with chorioamnionitis.

Several limitations of this study merit discussion. First, the current cohort features a limited number of cases with severe inflammation, including few instances of preterm delivery or chorioamnionitis. Future studies could benefit from employing a more comprehensive cohort to address this limitation. Second, due to limitations in resolution and signal-to-noise ratio inherent in current diffusion MRI technology, DBSI is not capable of cellular-level inflammation assessment. However, DBSI-derived images can effectively capture spatial and temporal changes of placental inflammation *in vivo* during gestation. When integrated with additional clinical data and machine learning models, this capability may serve as a valuable prognostic tool for predicting the course of inflammation and labor outcomes. Third, to mitigate the effects of blood susceptibility and to maintain image quality, a spin-echo sequence was employed with a 1mm slice thickness. This stands in contrast to the 5μm histology sectioning, optimized for staining, which only represents a subset of the 1mm MRI slice. Future work will focus on the development of 3D histological models utilizing CLARITY technology for volumetric correlation.

Chapter 4 : Whole cervix diffusion basis spectrum imaging (DBSI) of collagen, muscle, and cellularity in term and preterm birth

In this chapter, we introduce the development and validation of a novel imaging modality, whole-cervix diffusion basis spectrum imaging (DBSI). The validation process includes correlational assessments between DBSI-derived metrics and histological data from small *ex vivo* cervical tissue samples, as well as between *in vivo* data and clinical outcomes and metrics.

4.1 Cervix

During a typical pregnancy, cervical softening commences as early as the first trimester and progresses throughout the majority of the third trimester, all while maintaining tissue integrity[7–10]. This is followed by an accelerated ripening phase occurring a few weeks or days prior to labor. Finally, in conjunction with regular uterine contractions, the ripened cervix dilates, facilitating term delivery of the fetus[7].

The cervix is composed of an extracellular matrix (ECM) containing fibrillar collagen (types I and III), elastin, and proteoglycans, alongside cellular components including fibroblasts, smooth muscle cells, and immune cells[89,90]. This composition is critical for the cervix's structural integrity. Progressive remodeling of the cervical ECM leads to restructured collagen fibrils and a consequent reduction in tensile strength. Predominantly, quantitative assessments of cervical remodeling have focused on variations in collagen, smooth muscle, and cellularity.

Cervical softening is largely caused by increased hydration, disorganization of collagen fibers, increased collagen solubility, and decreased collagen concentration[91]. For example, analysis of human biopsy specimens from various gestational ages[92], immediately post-hysterectomy, and postpartum[93,94] revealed that, in the third trimester, more than 80% of the cervical collagen becomes soluble, and the collagen concentration is nearly half of that in the nonpregnant state.

Smooth muscle cells in the cervix may also be instrumental in cervical remodeling and may act as a sphincter to regulate cervical closing and opening[95–97]. Histological evidence identifies both longitudinal and circumferential muscle fibers in the human cervix[96]. One hypothesis is that contraction of longitudinal muscle fibers promotes cervical dilation, whereas contraction of circumferential muscle fibers keeps the cervix closed[98].

Finally, the role of immune cell infiltration in cervical remodeling remains under discussions. Earlier studies, involving human and rat specimens, suggested that infiltration of inflammatory cells contributes to disintegration and disorganization of the collagen matrix[99–101]. However, more recent studies in mice suggested that immune cell infiltration are not necessary to initiate cervical ripening, but instead participate in postpartum tissue repair[102,103]. Nonetheless, studies in mouse models suggested that infection and inflammation can promote premature cervical ripening[104,105], and Timmons et al. concluded that inflammatory cells are capable of inducing cervical ripening[7].

In current clinical practice, cervical length is used as a predictor of preterm birth, with studies indicating that early cervical shortening heightens the risk of preterm labor. For example, ultrasound imaging of cervical length during the second trimester[106, 107] revealed that about 50% of women with a very short cervix (≤ 15 mm) delivered at 32 weeks of gestation or earlier.

However, in another study with a different cutoff for diagnosing a short cervix, more than 60% of women with a cervix ≤ 25 mm at 18-22 weeks' gestation delivered at full term (≥ 37 weeks)[108]. Cervical softening can be assessed manually to derive a Bishop score, but this method is not superior to cervical length as a predictor of preterm birth[109].

4.2 Techniques to assess the cervix

Several methods have been developed to quantitatively assess cervical remodeling at the organ level. Cervical elastography, which can be included as an adjunct to routine ultrasound imaging, was used to measure the cervical elasticity index[110,111]. However, accuracy of this method is affected by a patient's respiration, arterial pulsation, fetal movements, and operator hand motion. Other approaches have included acoustic attenuation measurement in pregnant humans[112], quantitative ultrasound measurements on nonpregnant human *ex vivo* specimens[113], and magnetic resonance elastography to measure elasticity and viscosity of non-pregnant cervices *in vivo*[114]. Novel imaging techniques are also being explored, such as optical coherence tomography for quantifying collagen fiber dispersion in *ex vivo* cervix specimens[115,116], Raman spectroscopy for measuring spectral changes on the ectocervix surface *in vivo* during gestation and labor[117,118], and second harmonic generation imaging in *ex vivo* mouse specimens[119].

Several investigators have employed MR imaging (MRI) to quantify the changes in cervical microstructure *in vivo*. For example, Masselli et al. used MR diffusion weighted imaging to measure cervical hydration[120], and others have used 3D tractography of DTI data to delineate longitudinal and circumferential fiber tracts in the human cervix and uterus[121,122]. Qi et al. used a form of DTI that includes a tensor to describe the strength and directionality of water molecule diffusion in each voxel. With this method, they described mean, axial, and radial diffusivity, and

fractional anisotropy measures to reflect fiber organization and hydration[123]. However, as none of these MRI techniques are able to differentiate and quantitate cellularity, collagen fibers, and muscle fibers within each imaging voxel, our understanding of the *in vivo* microstructure of the entire human cervix remains incomplete.

4.3 Motivation to develop whole cervix DBSI

Addressing this critical gap in our understanding of cervical microstructures and monitoring their changes over gestation, this study describes a whole-cervix diffusion basis spectrum imaging (DBSI) multi-tensor model. Utilizing *ex vivo* specimens, we establish its ability to accurately image and quantitate collagen fibers, muscle fibers, and cells throughout the entire human cervix. This technique can provide voxel-level resolution of the cervix microstructural components, wherein each voxel is characterized by anisotropic and isotropic tensors to represent water diffusion within and around tissue-specific microstructural components. A whole brain DBSI multi-tensor model was originally validated for imaging brain inflammation in multiple sclerosis[82,83] and has been widely employed for brain microstructural imaging[84,124,125]. DBSI can be performed without contrast agents in a clinical MRI scanner and is safe for use during pregnancy[34–36]. Moreover, our analysis of *in vivo* DBSI data acquired at 32 weeks of gestation suggests that this method can be used to discern differences between the cervices of patients who delivered at term and those who had inflammation and delivered preterm. Consequently, DBSI holds great promise to provide *in vivo* biomarkers that accurately reflect cervix microstructure and remodeling. Such biomarkers could be instrumental in predicting preterm birth and assessing the efficacy of therapeutic strategies to prevent preterm birth in humans.

4.4 Experiment design

4.4.1 Enrollment criteria for patients included in *ex vivo* and *in vivo* studies

The *ex vivo* study was approved by the Washington University in St. Louis Human Research Protection Office (HRPO: 201903056, 202006074).

The parent study from which the *in vivo* data for this study were obtained was approved by the Washington University in St. Louis Human Research Protection Office (HRPO: 201707152, 202006021). For the parent study, patients were eligible if they were pregnant with a single fetus with a normal fetal anatomy and intended to deliver at Barnes-Jewish Hospital (Saint Louis, Missouri), were English-speaking, and were aged 18 years or older. Patients were excluded from the parent study if they tested positive for a blood-borne infectious disease, were an intravenous drug user, had contraindications to undergoing an MRI, had a body mass index greater than 40, or if the fetus had significant anomalies.

In this retrospective *in vivo* study, the following inclusion criteria were applied: For the preterm cohort with inflammation-associated adverse conditions, participants must have delivered before 37 weeks of gestation. Additionally, they must have had one or more of the following: a positive test result for gonorrhea, chlamydia, trichomoniasis, syphilis, human papillomavirus, bacterial vaginosis, yeast infection, herpes simplex virus, or COVID-19; a positive test for Group B Streptococcus (GBS) during pregnancy or receiving treatment for GBS; or diagnosed with endometriosis, placenta previa/accreta, or chorioamnionitis. For the healthy term cohort, participants must have delivered at or beyond 37 weeks of gestation and must not have had any of the inflammation-related adverse conditions described for the preterm group.

4.4.2 *Ex vivo* imaging of cervical tissue blocks

Blocks of tissue (approximately 30 × 25 × 3 mm^3) were dissected from the posterior midline of fresh total hysterectomy specimens. A custom specimen holder (**Figure 3.1**) was 3D printed (Form Labs, Form 2, RS-F2-GPCL-04 clear resin). The tissue block was embedded in 2% agar gel (**Figure 4.1**) (Sigma, SKU-0504D-100G) in the specimen holder at approximately 40 °C and quickly cooled to room temperature. It was then placed in the temperature-controlled MRI scanner room at 20 °C for 30 minutes to allow the specimen temperature to reach the ambient temperature. The specimen holder was inserted into a custom-made Helmholtz pair coil (**Figure 3.1**, Extend MR, LLC). MR images were acquired in an Agilent/Varian 11.74-T (500-MHz), DirectDrive MRI scanner (United States). Several scout images were acquired, and the specimen holder was adjusted to align the MRI bottom coronal plane with the specimen holder bottom plane. The specimen was then imaged by using two-dimensional single-shot spin-echo sequences for both T2W images and diffusion image series with the following parameters: Repetition time (TR) = 1000 ms, echo time (TE) = 32 ms, FOV = 36 × 36 mm, data matrix = 144 × 144, slice thickness = 1.0 mm, no slice spacing. For the diffusion images, the diffusion gradients were applied in up to 74 directions (same as *in vivo*, see **Table Appx. 1**) with *b values* of 0 – 4500 s/mm^2. After imaging, the specimens were fixed in 10% neutral-buffered formalin for one week and then processed into paraffin in "as-is" orientation. Sections (5 μm) were cut from the bottom plane, which was the same as the MRI bottom coronal plane, mounted on slides, and stained with hematoxylin & eosin and Masson's trichrome (Ventana Trichrome Kit (92)860-031). The slide images were digitized (20× magnification, Hamamatsu NanoZoomer HT).

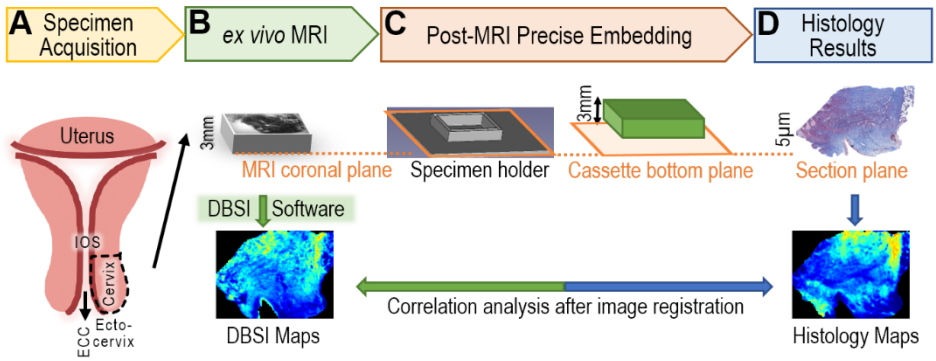

Figure 4.1: Experimental set-up to use *ex vivo* specimens to validate cervix-optimized DBSI parameters. (A) A specimen (3 mm thickness) was dissected from the posterior midline of fresh total hysterectomy uteruses. Labels "IOS" and "ECC" indicate internal OS of cervix and endocervical canal respectively. (B) The specimen was embedded in 2% agar gel and imaged with a Varian 11.7T MRI, using DBSI sequence. DBSI maps were computed by in-house cervix-optimized DBSI software. (C) After MRI, the specimen was fixed in formalin, transferred, and embedded in a paraffin block along the plane of MR imaging (orange dotted lines indicates the same plane). (D) The stained slide-mounted 5 μm histologic sections were digitized and converted to histology maps. The histology maps were then registered to the DBSI maps.

4.4.3 Human *in vivo* MR imaging

MR images from were acquired from a Siemens 3 Tesla MAGNETOM Vida (Erlangen, Germany) at patients' gestational ages of 32 ± 2 weeks. Patients were imaged in the left lateral position with their feet entering the magnet bore first. A 30-channel phased array torso coil covered the entire pelvis. Each patient underwent up to 45 minutes imaging with the following MRI sequences:

1. Localizer (to adjust the field of view to cover the entire uterus and cervix)
2. T1-weighted volume-interpolated breathhold examination (VIBE) sequence in the sagittal plane, with the following parameters: repetition time (TR) = 4.07 ms; echo time (TE) = 1.87 ms; field of view (FOV) = 400 × 400 mm; data matrix, 320 × 320; layer thickness, 4.0mm; slice spacing, 0.8 mm; number of layers, 80; flip angle, 10°.

3. T2-weighted turbo spin echo high-resolution images in sagittal plane, with the following parameters: TR = 4660 ms; TE = 96 ms; FOV, 350 × 350 mm; data matrix, 320 × 650; layer thickness, 4.0 mm; slice spacing, 0.8 mm; number of layers, 34; flip angle, 155°.
4. T2-weighted turbo spin echo high-resolution images in oblique planes perpendicular to cervical cannel, with the following parameters: TR = 4110 ms; TE = 96 ms; FOV, 400 × 400 mm; matrix, 320 × 650; layer thickness, 4.0 mm; slice spacing, 0.8 mm; number of layers, 30; flip angle, 155°.
5. Two dimensional single-shot echo planar imaging diffusion-weighted sequence, with the following parameters: TR = 6300 ms; TE = 63 ms; FOV = 350 × 350 mm; data matrix, 128 × 128; slice thickness, 3.0 mm, no slice spacing. The diffusion gradients were applied in up to 74 directions (**Table Appx. 1**) with B values ranging from 0 - 2000 s/mm^2.

4.5 Computational methods

4.5.1 Multi-tensor DBSI model for cervix

To design a realistic multi-tensor model for imaging cervical microstructures, we used Monte-Carlo simulation (previously detailed in **Section 3.5.1**) to compute the Brownian motion trajectories (dashed arrows in **Figure 4.2B**) of randomly distributed water molecules in different components of cervical microstructures at 37 °C under a diffusion gradient. A cervix contains cells, fibrillar collagen, proteoglycans, hyaluronan elastin, and water[91]. Additionally, some studies have identified smooth muscle cells and fibers in the human cervix[95,96]. Thus, we developed DBSI multi tensor models to reflect five types of water diffusion in cervical microstructures: intracellular water, hindered water, free water, collagen fibers, and muscle fibers.

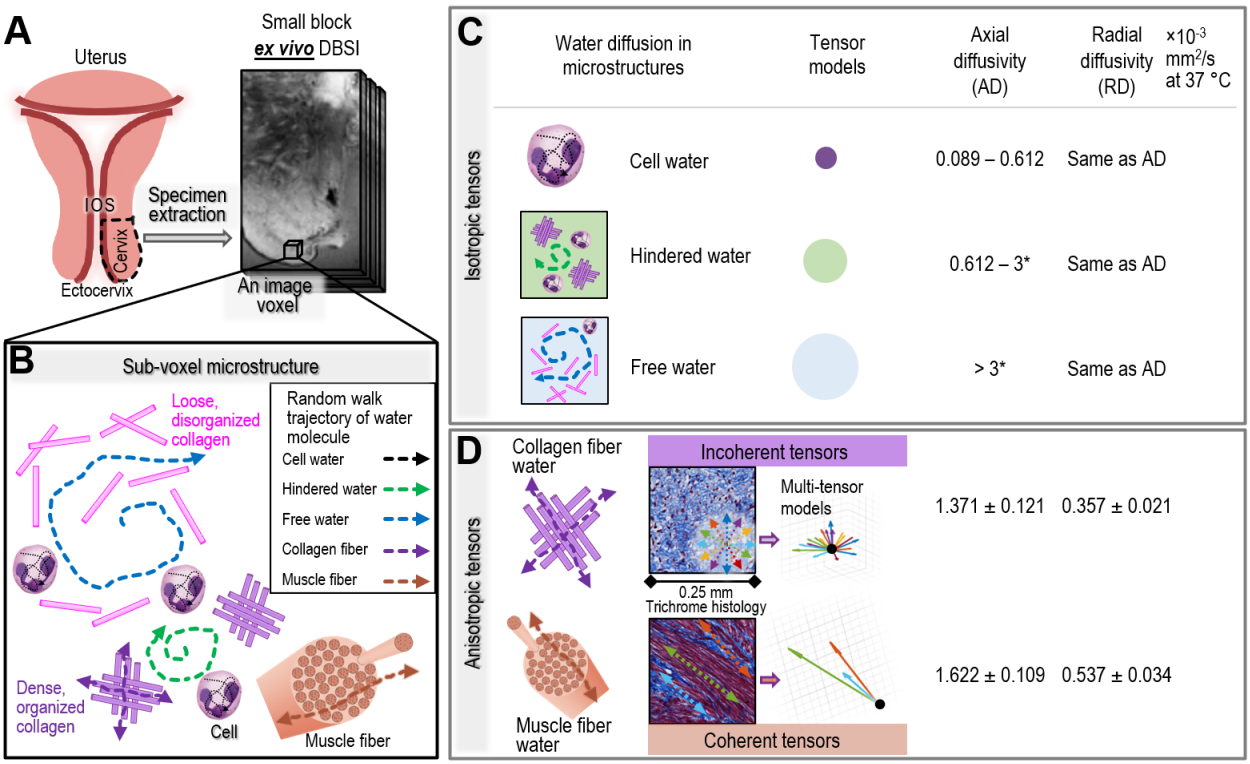

Figure 4.2: The design of multi-tensor models for whole cervix DBSI based on the results from Monte-Carlo simulation.

The design of multi-tensor models for whole cervix DBSI based on the results from Monte-Carlo simulation. (A) Schematic and representative magnetic resonance images of the cervical region used for *ex vivo* validation of the DBSI parameters. (B) In an image voxel in the cervix, we modeled three types of isotropic water diffusion: restricted isotropic diffusion within cell membranes (black dashed line in cells), hindered isotropic diffusion (green) around the dense, organized collagen fiber and cells, and free water diffusion (blue) in the region with loosely distributed and disorganized collagen fiber and cells. We also modeled two types of anisotropic water diffusion: incoherent anisotropic diffusion within bundles of tightly packed crossing collagen fibers (purple) and coherent anisotropic diffusion inside bundles of parallel packed muscle fibers (coral). The dashed arrows are examples of water molecule trajectories under a diffusion gradient. (C) The isotropic tensor models are visualized as spherical balls with the radius reflecting their relative diffusivities. Axial and radial diffusivity of water molecules in cell, collagen, and muscle fiber from the Monte-Carlo simulation. *Free water diffusivity was derived from known experimental values [85,86]. (D) Anisotropic tensors represent water diffusion within a bundle of tightly packed collagen fibers (purple-colored crossing solid rods) and inside a bundle of parallel packed muscle fibers (coral-colored cylindrical tubes).

The diffusion of intracellular water, hindered water, and free water is all isotropic. To model intracellular water diffusion in various cell types in human cervix, we designed spherical models with radii of 5 – 12 μm, with random "seeds" representing water molecules placed inside (**Figure 4.2C**). The Monte-Carlo simulation results yielded restricted isotropic diffusion with apparent diffusion coefficients (which are equal to axial diffusivity [AD] and radial diffusivity [RD] for isotropic diffusion) between 0.089×10^{-3} and 0.612×10^{-3} mm^2/s (**Figure 4.2E**). We then

defined hindered water as isotropic diffusion of water molecules whose trajectories (green dashed arrows, **Figure 4.2B, C**) are hindered by dense, organized collagen fibers (purple rods) and cells. We defined free water as isotropic diffusion of water molecules whose trajectories (blue dashed arrows, **Figure 4.2B, C**) that move freely around loose and disorganized collagen fibers (pink rods) and cells. To model free water, we derived diffusivity of 3×10^{-3} mm^2/s from known experimental values[85,86]. Additionally, isotropic tensors with the diffusivity exceeding 10×10^{-3} mm^2/s were utilized to account for intravoxel incoherent motion effect. A total of 150 isotropic tensors (same as **Figure 3.5**) was then designed by discretizing the four ranges of isotropic diffusivity values.

The diffusion of water surrounding collagen fibers and within muscle fibers is anisotropic. For incoherent anisotropic water diffusion around collagen fibers, we simulated the random walk trajectories of water molecules travelling within a crossing bundle of tightly packed solid cylindrical rods at angles between 0 and 20 degrees (purple rods, **Figure 4.2B, C**) to reflect various fiber orientations and dispersion patterns indicative of both normal and pathological conditions in cervix. The resulting diffusion simulation yielded AD values of $1.371 \pm 0.121 \times 10^{-3}$ mm^2/s and RD values of $0.357 \pm 0.021 \times 10^{-3}$ mm^2/s (**Figure 4.2E**). For coherent anisotropic water diffusion within muscle fibers, we simulated the random walk trajectories of water molecules travelling inside a bundle of parallel hollow cylindrical tubes (**Figure 4.2D**). The resulting diffusion simulation yielded AD values of $1.622 \pm 0.109 \times 10^{-3}$ mm^2/s and RD values of $0.537 \pm 0.034 \times 10^{-3}$ mm^2/s (**Figure 4.2E**).

Nine detailed anisotropic tensor models of AD and RD combinations (**Table 4.1**) were designed to model all anisotropic diffusion in cervix and each was replicated in 25 principal

directions uniformly distributed in a 3D space to achieve a total of 225 anisotropic tensors. Specifically, the tensor models #2 and #3 (AD = 1.8 – 2.0×10^{-3} mm^2/s, RD = 0.3 – 0.4×10^{-3} mm^2/s at 37 °C) represent muscle fibers, and the tensor models #5, #6, and #7 (AD = 1.6 – 2.1×10^{-3} mm^2/s, RD = 0.5 – 0.7×10^{-3} mm^2/s at 37 °C) represent collagen fibers. The other tensor models represent remaining connective tissue structures in the cervix.

For *ex vivo* specimens imaged at 20 °C, a linear coefficient of 0.6667 was applied on all isotropic and anisotropic diffusivity values according to quadratic fit of known diffusivity values at a range of temperatures[85,86].

Table 4.1: Anisotropic tensor models for whole cervix DBSI

Diffusivity ×10^{-3} mm^2/s	Tensor 1	Tensor 2	Tensor 3	Tensor 4	Tensor 5	Tensor 6	Tensor 7	Tensor 8	Tensor 9
Radial Diffusivity (RD)	0.2	0.3	0.4	0.4	0.5	0.6	0.7	0.9	1.2
Axial Diffusivity (AD)	1.2	1.8	2.0	1.6	1.6	1.8	2.1	2.7	3.6
AD / RD	6	6	5	4	3.2	3.0	3.0	3.0	3.0

4.5.2 Histology quantification

A 20× bright field image was trimmed to tiles (5000 × 5000 pixels) and stitched together after processing. Researchers with histology training first delineated about a dozen typical cell nuclei, regions of background, and connective tissue (eosin stain) on one tile image to train an Orbit Image Analysis[87] tissue classifier based on chromatic information. All image tiles were classified to binary masks of positive nuclei stain by the trained classifier. Then, the remainder of the histology quantification was done by an in-house MATLAB program. The binary masks were converted to nuclei density maps by calculating percentage of nuclei area per 50 × 50 pixels area.

These tiles of nuclei density maps were then stitched together and downsampled to 10 times the MR image plane resolution for the next step of image registration. The collagen fiber and muscle fiber density maps were processed with the same pipeline by classifying chromatic information of positive collagen stain (blue) and muscle stain (scarlet) in trichrome histology.

4.5.3 Image registration

The specimen contours from the nuclei, collagen fiber, and muscle fiber density maps and T2W MR image were delineated in 3D slicer[88]. An Affine linear registration guided by fiducial landmarks was performed to register the nuclei density map, collagen fiber fraction map, and muscle fiber fraction map to the T2W MR image. After registration, the histology maps were down sampled to the same resolution as the DBSI-derived maps. In the correlation analysis, both DBSI and histology maps were further downsampled to 2.5 mm to match the resolution of *in vivo* diffusion MR images from a clinical MRI scanner.

4.6 Evaluation of whole cervix DBSI microstructure parameters in *ex vivo* tissue blocks

To validate the DBSI parameters, we recruited three patients who were undergoing planned total hysterectomies. Two multiparous patients (who provided samples P1-S1, P1-S2, and P2-S1) were both 37 years of age and were undergoing hysterectomy after delivery. Patient P1 had placenta previa and placenta accreta and underwent Caesarean hysterectomy at 34.2 weeks of gestation. The pathology examination showed endometriosis involving the cervix. Patient P2 had placenta accreta and underwent Caesarean hysterectomy at 34.0 weeks of gestation. The pathology examination showed a normal cervix. One patient (sample NP1-S1) was 43 years of age, non-

pregnant, and undergoing hysterectomy to treat long-term abnormal uterine bleeding. The pathology examination showed a cervix with chronic inflammation. After surgery, we obtained cervix specimens (**Figure 4.1**), embedded them in agar gel, and imaged with the DBSI sequence in a small animal MRI scanner. We then fixed the samples, cut sections, and stained them with hematoxylin and eosin (H&E) to detect nuclei and Masson's trichrome to detect collagen and muscle fibers. We then co-registered the stained sections and the MR images.

4.6.1 DBSI-cellularity in cervix

To compare cellularity in the histology and DBSI images, we segmented the H&E images and converted the positive stain of nuclei to the nuclei density maps (**Figure 4.3B**). In the DBSI images, we calculated cell fraction as the percentage of diffusion signal contributed by intracellular water over total diffusion signals. Qualitatively, in all four specimens, the DBSI cell fraction maps and the histological maps showed that cells were most abundant in the subglandular region (labeled SG in **Figure 4.3**) near the endocervical canal. To quantitatively compare the DBSI-derived cell fraction and histological nuclei density maps, we downsampled the maps and performed correlation analysis by comparing the mean values in 2.5 × 2.5 mm regions (solid white boxes, **Figure 4.3C**). The DBSI-derived cell fractions correlated with histological nuclei densities in all four specimens (**Figure 4.3D**).

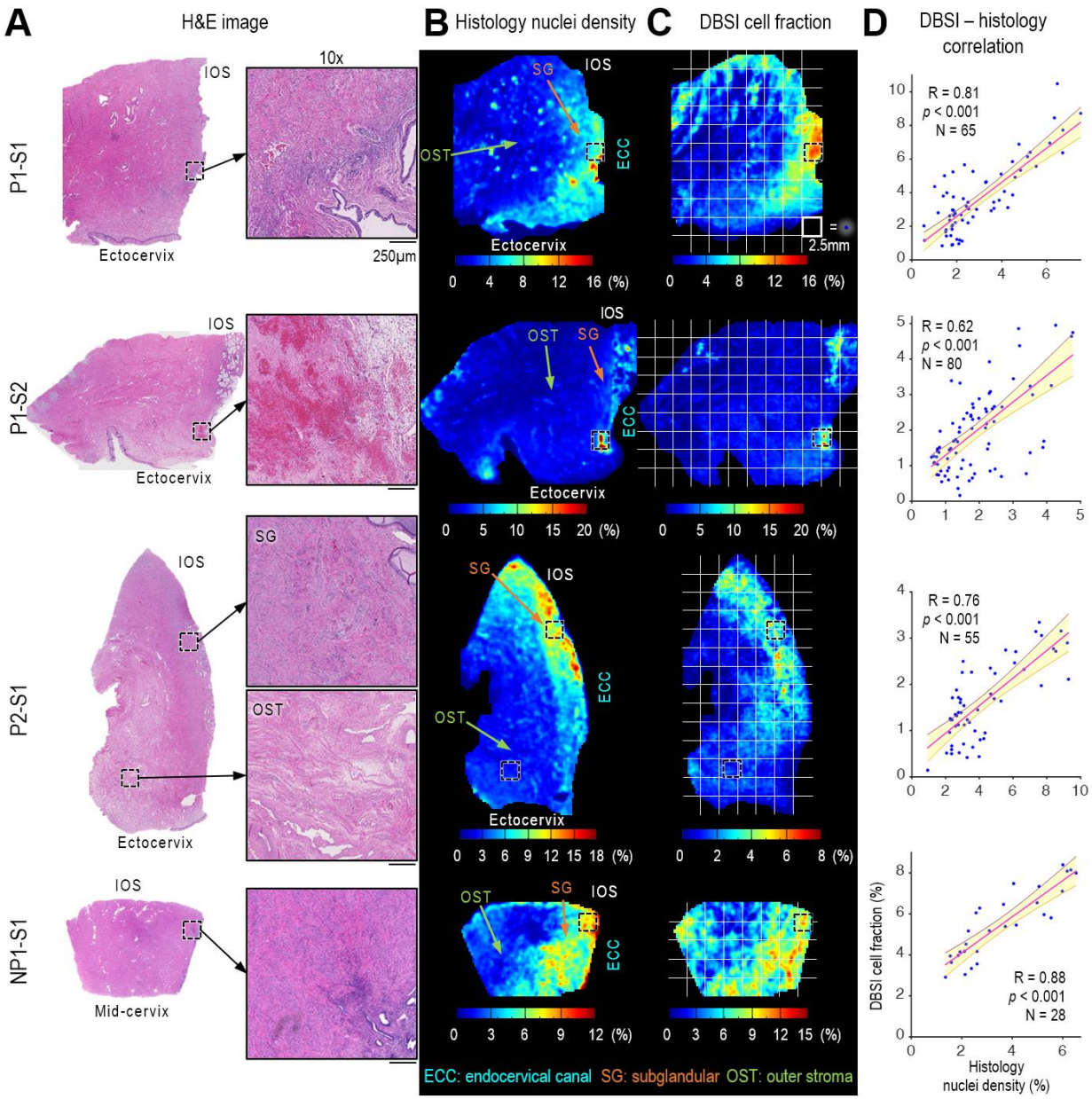

Figure 4.3: Correlation between histological nuclei density maps and DBSI cell fraction maps.
(A) H&E images of cervix specimens and 10× magnified views of the black-dashed-boxed regions. The magnified views of P2-S1 show examples of high cell density in the subglandular (SG) region near the cervical canal and low cell density in outer stroma (OST) region, which are reflected on both histological density maps and DBSI maps. (B, C) Comparison of histological nuclei density maps (B) and DBSI-derived cell fraction maps (C). IOS, internal os; ECC, endocervical canal. (D) Pearson correlation coefficients of DBSI cell fraction and histology nuclei density. Each blue dot represents the mean value from a 2.5 × 2.5 mm white grid box within the specimen's contour in Panels B and C. The red lines are the linear fits, and the shaded areas are 95% confidence intervals.

4.6.2 DBSI-collagen in cervix

In the trichrome-stained images (**Figure 4.4A**), the positive stain of collagen (blue) was segmented and converted to collagen density maps (**Figure 4.4B**). Qualitatively, the DBSI collagen fiber fraction maps and the histological collagen density maps showed the most abundant collagen in the subglandular region and the least abundant collagen in the outer stroma region, especially near the ectocervix. Quantitatively, the DBSI-derived collagen fiber fractions correlated with the histological collagen densities (**Figure 4.4D**)

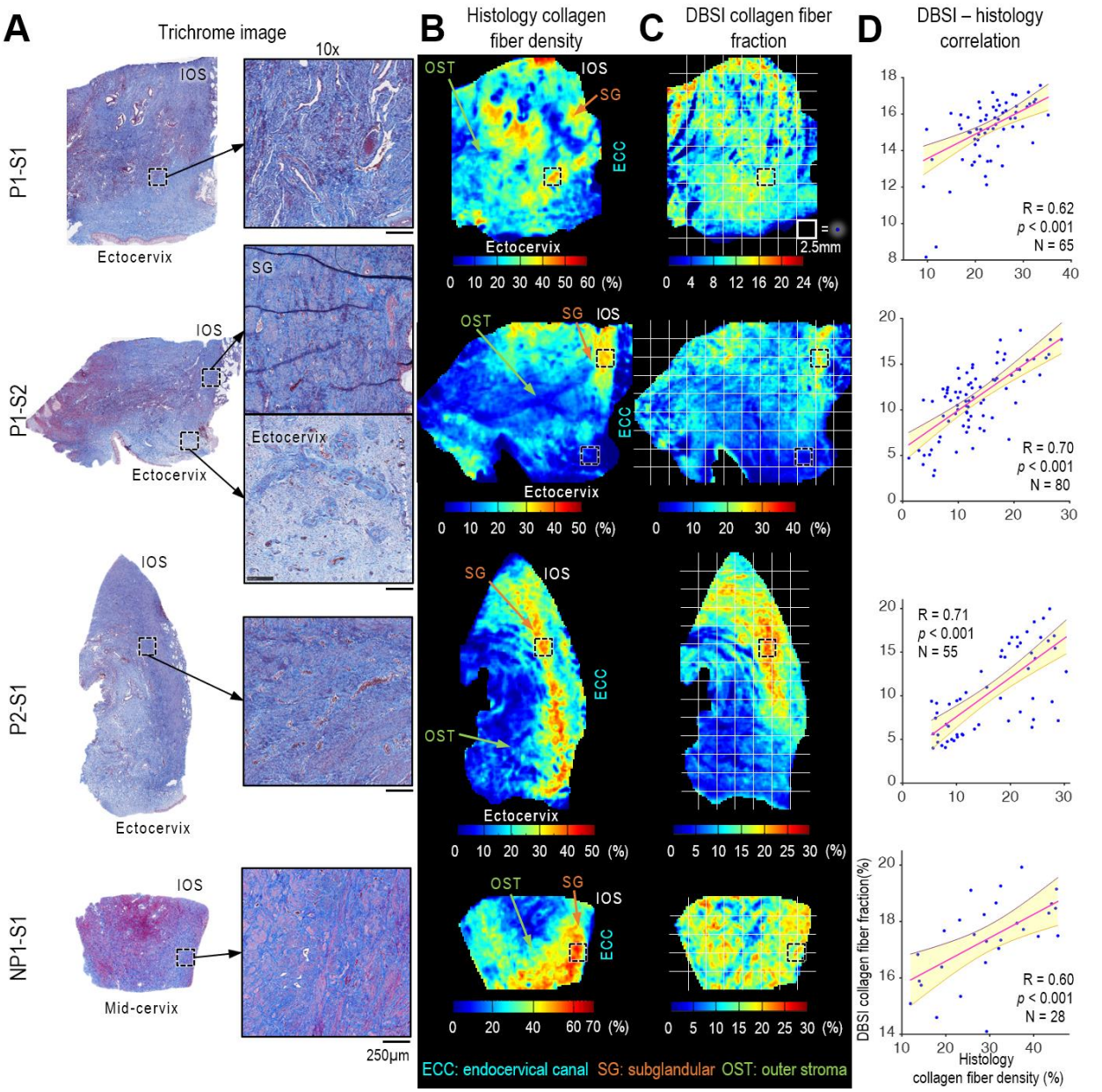

Figure 4.4: Correlation between histological collagen density maps and DBSI collagen fraction maps.
(A) Trichrome images of the specimens and 10× magnified views of the black-dashed-boxed regions. The magnified views of P1-S2 show examples of dense organized collagen fibers in the subglandular (SG) region and loose disorganized collagen fiber near the ectocervix, which are reflected on both histological density and DBSI maps. (B, C) Comparison of histological collagen density maps (B) and DBSI-derived collagen fraction maps (C). (D) Pearson correlation coefficients between DBSI collagen fiber fraction and histology collagen fiber density. Each blue dot represents the mean value from a 2.5 × 2.5 mm white grid box within the specimen's contour in Panels B and C.. Red lines indicate linear fits, and shaded areas indicate 95% confidence intervals.

4.6.3 DBSI-muscle in cervix

In the trichrome-stained images (**Figure 4.5A**), the positive stain of muscle fibers (scarlet) was segmented and converted to muscle fiber density maps (**Figure 4.5B**). In specimens P1-S1, P1-S2, and NP1-S1, the muscle was dense and clearly separated from the collagen. In the DBSI muscle fraction maps from these specimens, the orientations of muscle tracts appeared to coincide with those in the histological density maps. For example, specimen P1-S1 contained many longitudinal muscle fibers at middle locations radially from the canal, whereas specimen P1-S2 from the same patient contained many circumferential muscle fibers near the cervix-uterus junction (labeled "⊥"). Quantitatively, the DBSI-derived muscle fiber fractions correlated with the histological muscle densities **Figure 4.5D**).

Collectively, the strong correlations (**Figure 4.3D, Figure 4.4D**, **Figure 4.5D**) suggested that DBSI parameters allow us to accurately quantify cells, collagen, and muscle fibers throughout the entire human cervix samples.

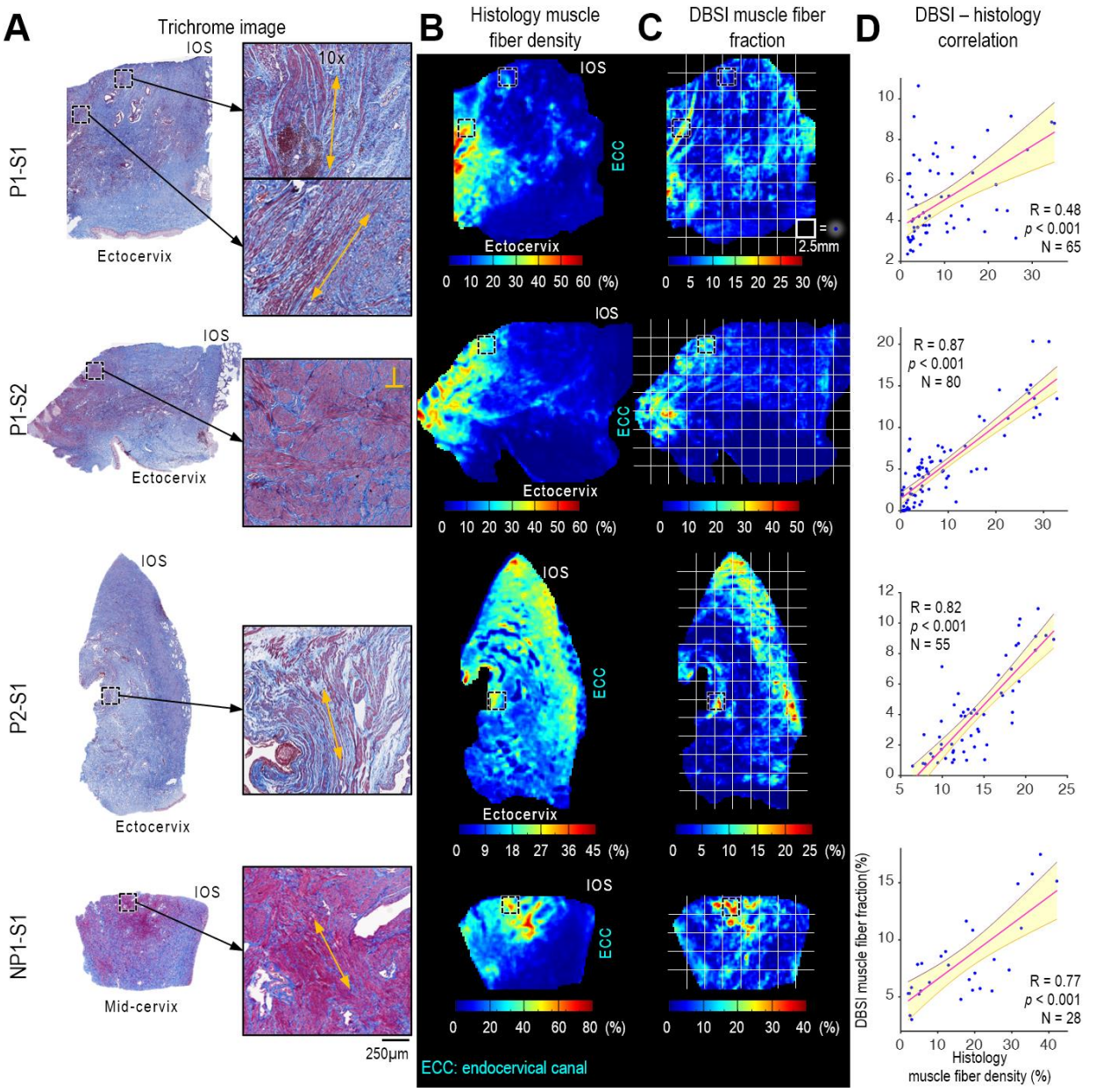

Figure 4.5: Correlation between histological muscle density maps and DBSI muscle fraction maps.
(A) Trichrome images of the specimens and 10× magnified views of the black-dashed-boxed regions. Specimen P1-S1 shows many longitudinal muscle fibers at middle locations radially from the canal; fiber directions indicated by yellow arrows). Specimen P1-S2 shows many circumferential muscle fibers near the cervix-uterus junction that are perpendicular (yellow⊥) to the slides. (B, C) Comparison of histological muscle density maps (B) and DBSI-derived muscle fraction maps (C). (D) Pearson correlation coefficients of DBSI muscle fiber fraction and histology muscle fiber density. Each blue dot represents the mean value from a 2.5 × 2.5 mm white grid box within the specimen's contour in Panels B and C. . Red lines are linear fits and shaded areas are 95% confidence intervals.

4.7 *In vivo* DBSI measures of the cervix differ between term and preterm patients

To begin to assess the utility of our whole cervix DBSI, we retrospectively analyzed DBSI data collected from patients at 32 ± 2 weeks of gestation who were enrolled in other studies. For this study, we selected ten healthy patients who had delivered at term (at or after 37 weeks of gestation) and did not present any adverse pregnancy complications. Eight of the ten patients were admitted for induced term labor. Two patients were admitted for spontaneous term labor with contractions, one of whom presented with rupture of membrane at admission. Additionally, we identified ten patients who completed the 32-week MR imaging, had inflammation-related adverse conditions (described in the method section in detail) and delivered preterm (less than 37 weeks of gestation). Three of the ten preterm patients were excluded because of inadequate image quality and motion blur; thus, seven preterm patients with adverse inflammatory conditions were included in the analysis (**Table 4.2**). In the preterm group, two patients were admitted for spontaneous preterm labor with contraction, one of whom presented with rupture of membrane at admission; three patients were admitted for induced labor due to preeclampsia and delivered vaginally preterm; one patient was admitted for preterm Caesarean section due to preeclampsia; and one patient was diagnosed with endometriosis in the cervix and was admitted for preterm Caesarean section due to placenta previa and accreta. The term and preterm groups were similar with regard to maternal age and race (**Table 4.2**).

Our *in vivo* DBSI data distinguishes between term and inflammation-associated preterm deliveries. This is accomplished by quantifying DBSI metrics like collagen content, which involves calculating the fraction of the T2-weighted signal from diffused water molecules among

collagen fibers, relative to the voxel's total T2-weighted signal under diffusion gradients. This approach is similarly applied to DBSI-cell and -muscle fractions.

Table 4.2: Demographic characteristics of the healthy term and adverse preterm group in the *in vivo* studies

In vivo patients			
Demographic parameters	Healthy term	Preterm	*P* value
Number of patients	10	7	
Median age, years (IQR)	31 (25 - 34)	29 (27 - 32)	0.82
Gestational age at deilvery, weeks.days(IQR)	39.3 (39.1 - 39.5)	35.2 (34.6 - 36.2)	
Race, n			0.43
White	6	3	
African American	3	4	
Asian	1	0	
Other	0	0	

Figure 4.6 shows T2-weighted (T2W) MR images and DBSI cellularity, collagen fiber, and muscle fiber fraction maps of the cervix in four representative preterm patients and four representative term patients. We used the T2W images to segment the cervix images and mask the mucus-filled endocervical canals. Qualitatively, the cervixes from all four preterm patients exhibited a higher DBSI cell fraction (with a few hot spots at 10%) than did the cervices from the term patients, in which the DBSI cell fractions were less than 5%. Cervices from the preterm patients appeared to have lower collagen density (less than 5% in most areas) than the cervices from the term patients (10% – 15% in most areas). The cervices from the preterm patients had several regions in which the muscle fraction was nearly 20%, whereas the cervices from the term patients had somewhat lower muscle fractions. Finally, the cervices in the preterm patients appeared to have higher DBSI free water fraction (up to 60%) than did the cervices in the term patients (mostly below 30%).

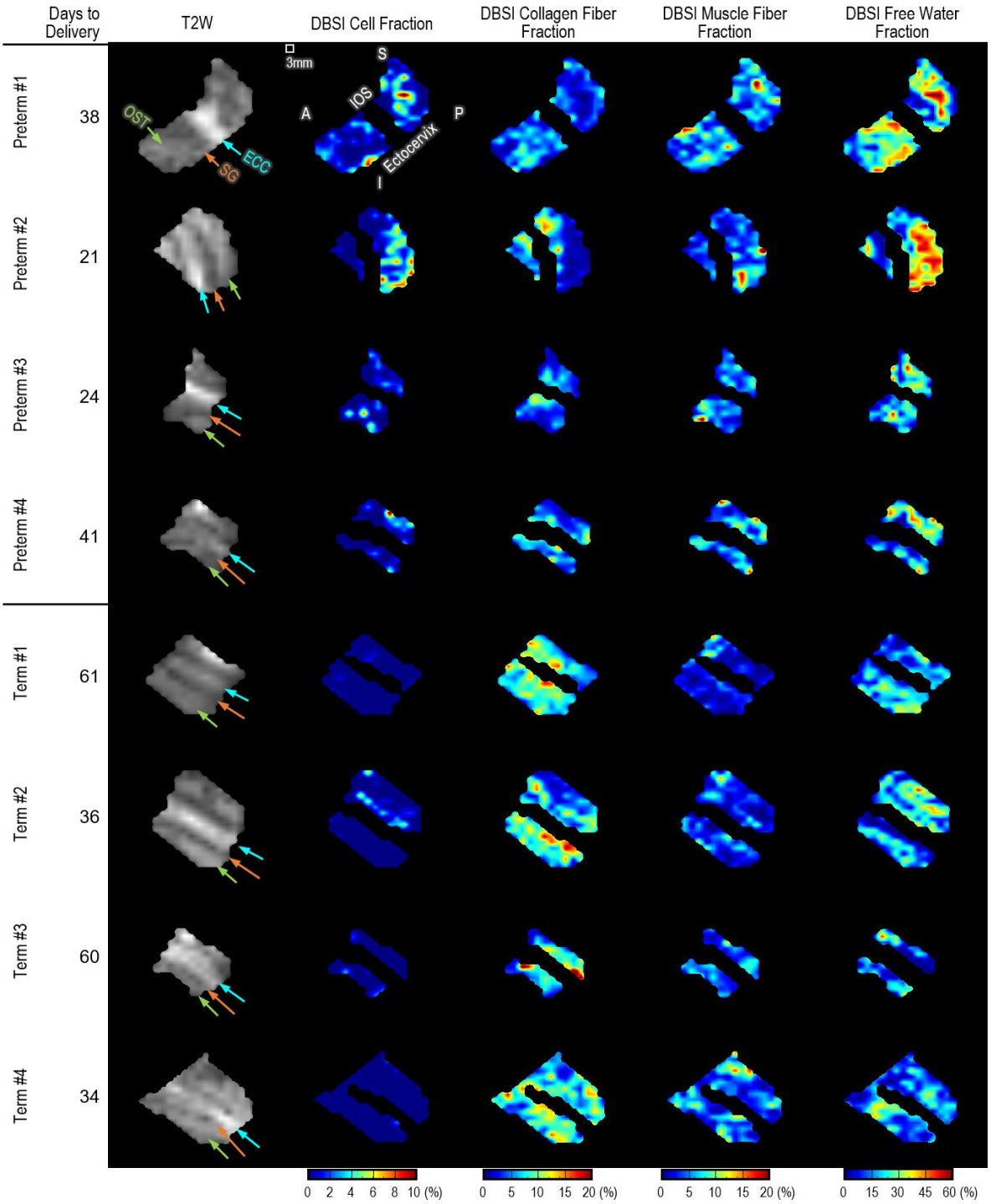

Figure 4.6: Sagittal view of T2W images and DBSI-derived cell, collagen, muscle fraction, and free water fraction maps from representative patients in the term and preterm groups.

Days to delivery are calculated from the day of MR imaging to the date of delivery. The color-mapping is the same for all eight patients. Color-coded arrows and labels "IOS" (white), "OST" (lime green), "SG" (orange), and "ECC" (cyan blue) indicate internal OS of cervix, outer stroma, subglandular, and endocervical canal, respectively. Labels "S", "I", "A" and "P" indicate patient's superior, inferior, anterior, and posterior positions, respectively.

Next, we quantitatively compared the DBSI measures in the whole cervical volume from all 17 patients. Compared to the cervices from the term group, the cervices from the preterm group had significantly higher DBSI cell fraction (**Figure 4.7A**), significantly lower collagen fiber fraction (**Figure 4.7B**), significantly higher muscle fiber fraction (**Figure 4.7C**), and significantly higher free water fraction (**Figure 4.7D**). Specifically, in the preterm group, the median values for cell fraction, muscle fraction, and free water fraction are approximately 1.94, 1.46, and 1.36 times of those in the term group, respectively. Conversely, the median collagen fraction in the term group is about 1.65 times that of the preterm group. We plotted the DBSI measures of cell fraction, collagen fiber fraction, and muscle fiber fraction on X-Y-Z axes for each patient and generated 3D Gaussian ellipsoids fit with two standard deviations of the mean and 95% probability in each dimension. We observed a clear separation between the term and preterm ellipsoids (**Figure 4.7O**).

Finally, we examined data with regard to days from DBSI imaging until delivery. We found significant linear correlations between days to delivery and cell (**Figure 4.7E**), collagen fiber (**Figure 4.7F**), and muscle fiber (**Figure 4.7G**) fractions. We also found significant linear correlations between these DBSI measures and cervical lengths measured at 32 ± 2 weeks of gestation in T2W MR images (**Figure 4.7I, J, K**). In contrast, no correlation was found between DBSI free water fraction and either days to delivery (**Figure 4.7H**) or cervical length at 32 weeks (**Figure 4.7L**). The cervical lengths, measured at 32 ± 2 weeks of gestation in the T2W MR images (**Figure 4.7M**), significantly differed between the term and preterm groups as expected. In contrast, the cervical lengths measured at 20 ± 2 weeks of gestation by transvaginal ultrasound (**Figure 4.7N**) did not significantly differ between the term and preterm groups. Taken together, these data suggest that the DBSI-derived measures of the cervix at 32 ± 2 weeks' gestation can differentiate between patients who deliver at term and patients who deliver preterm.

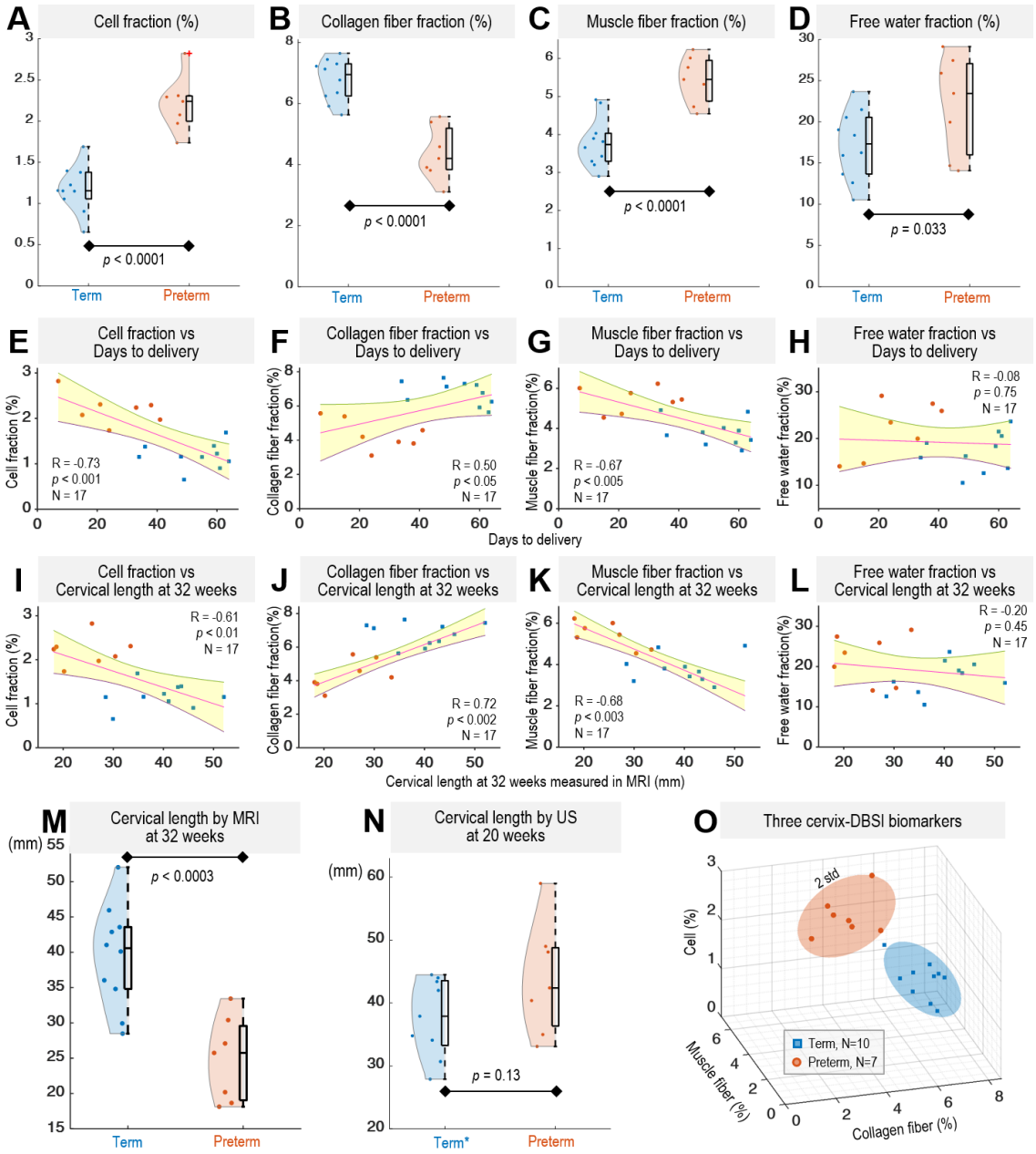

Figure 4.7: DBSI-derived cell, collagen fiber, muscle fiber, and free water fraction in the term and preterm groups.

(A–D) Box plots of the indicated DBSI measures in the term and preterm groups. Each dot represents the median value over the whole cervix of each patient (healthy term, blue, N = 10; preterm, orange, N = 7). The box plots show the medians and quartiles (solid black), and the violin plots show the distribution of the DBSI-derived median values from each patient. (E–H) Correlations between days from DBSI imaging to delivery and the indicated DBSI measures. (I–L) Correlations between cervical lengths measured at 32 ± 2 weeks of gestation in T2W MR images and the indicated DBSI measures. In E–L, each pink dot represents the median value over the whole cervix for one preterm patient, each blue dot represents the median value over the whole cervix for one term patient, red lines are linear fits, and shaded areas are 95% confidence intervals. (M, N) Box plots of (M) cervical length by MRI at 32 weeks and (N) cervical length by transvaginal ultrasound at 20 weeks in term and preterm groups. (O) Three DBSI measures on X-Y-Z axes for each patient and Gaussian ellipsoids of two standard deviations of the mean (95% probability in each dimension).

4.8 Additional correlation analysis

4.8.1 Correlation at different gird size

The chosen 2.5 × 2.5 mm grid size aligns with the standard *in vivo* diffusion MRI resolutions in clinical MR scanners. To reinforce the validity of our findings, we conducted additional analyses using different grid sizes (2 × 2 mm, 1.75 × 1.75 mm, and 1.5 × 1.5 mm). These analyses (**Figure 4.8** – **Figure 4.11**) consistently demonstrate a strong correlation between histology quantification and *ex vivo* DBSI metrics, underscoring the robustness of our approach.

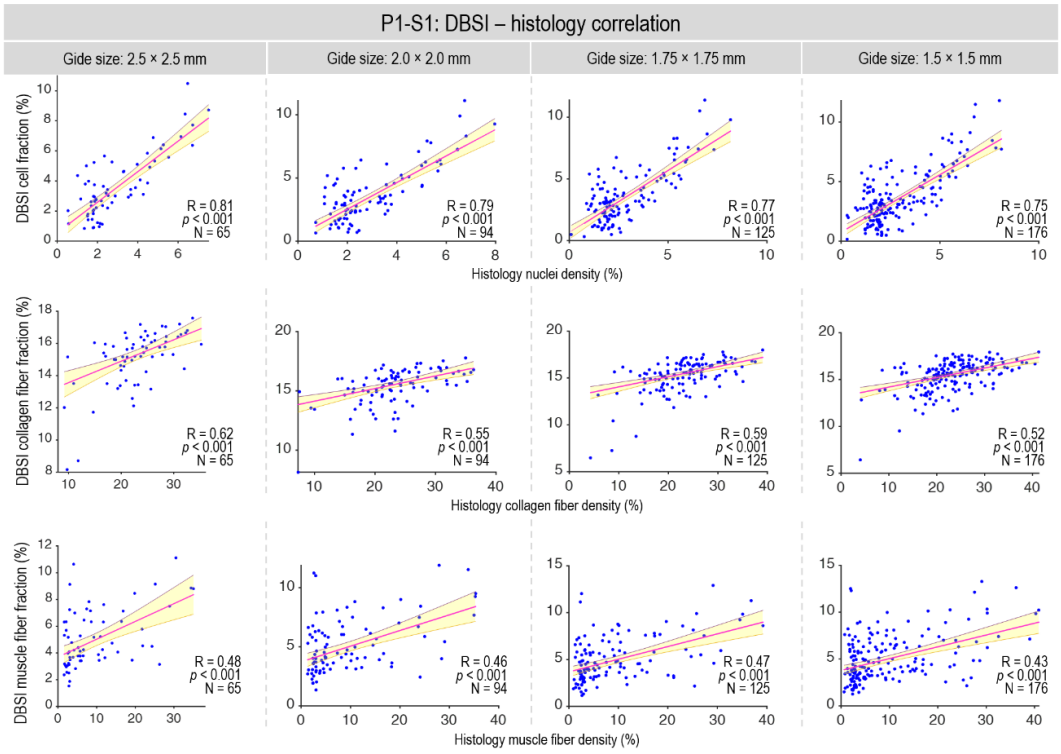

Figure 4.8 Pearson correlation analysis of DBSI versus histology at vaires grid sizes for specimen P1-S1.
Data points indicate mean values per grid box from Fig. 4.3, 4.4, and 4.5, panels B and C. Red lines: linear fits; shaded areas: 95% confidence intervals.

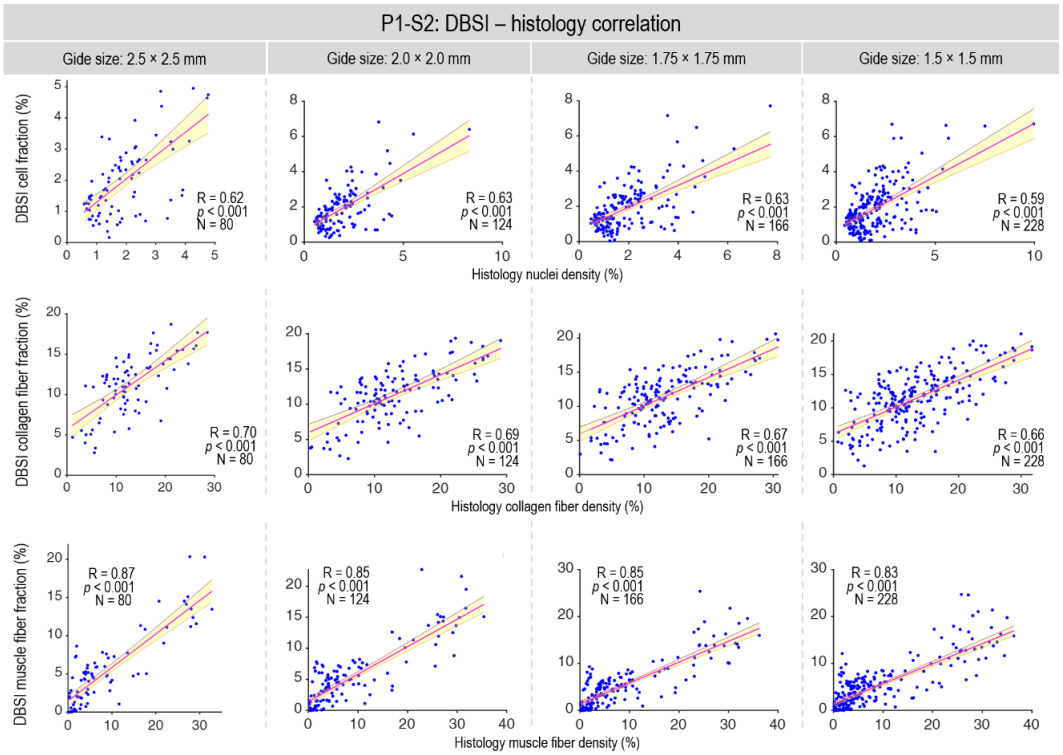

Figure 4.9: Pearson correlation analysis of DBSI versus histology at vaires grid sizes for specimen P1-S2. Data points indicate mean values per grid box from Fig. 4.3, 4.4, and 4.5, panels B and C. Red lines: linear fits; shaded areas: 95% confidence intervals.

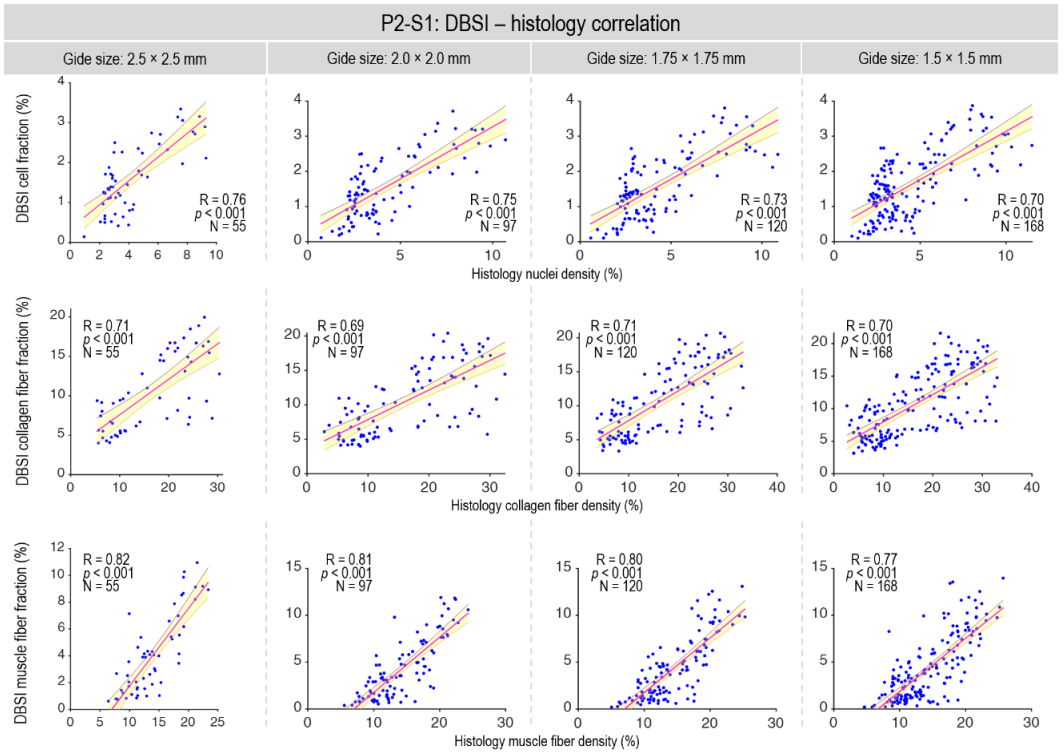

Figure 4.10: Pearson correlation analysis of DBSI versus histology at vaires grid sizes for specimen P2-S1. Data points indicate mean values per grid box from Fig. 4.3, 4.4, and 4.5, panels B and C. Red lines: linear fits; shaded areas: 95% confidence intervals.

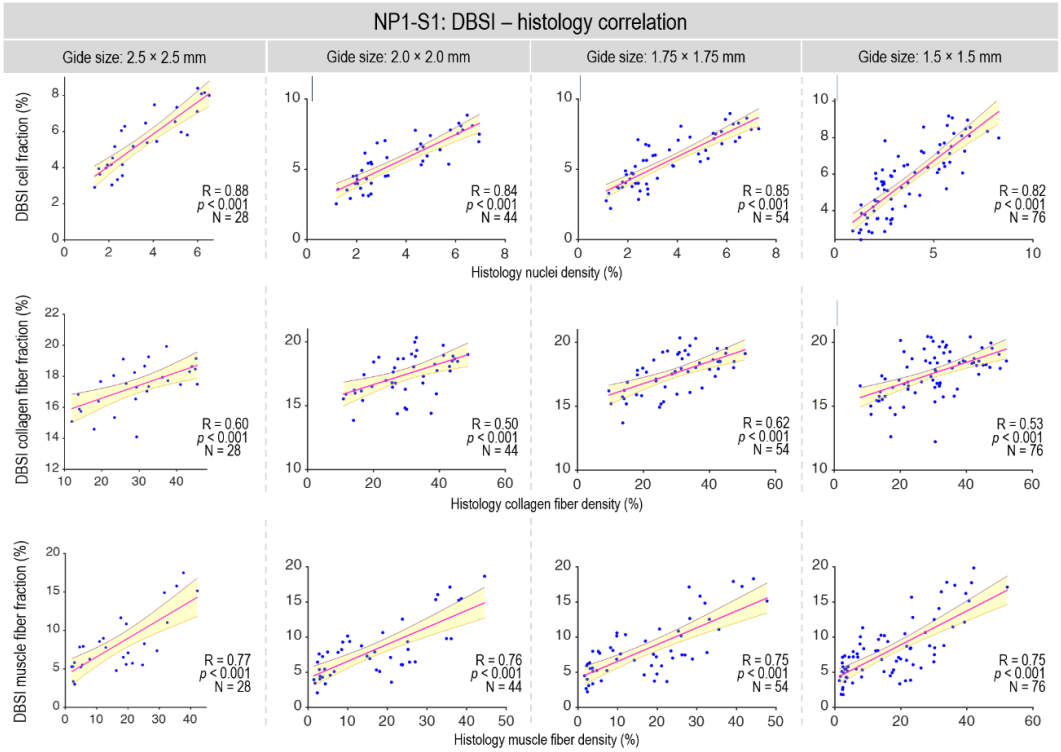

Figure 4.11: Pearson correlation analysis of DBSI versus histology at vaires grid sizes for specimen NP1-S1. Data points indicate mean values per grid box from Fig. 4.3, 4.4, and 4.5, panels B and C. Red lines: linear fits; shaded areas: 95% confidence intervals.

4.8.2 Correlation analysis of *ex vivo* specimen between diffusion tensor imaging and histology

This supplementary analysis utilizing diffusion tensor imaging (DTI) model (**Figure 4.12 – Figure 4.15**) reveals that the histology-derived data, including nuclei density indicative of cellularity and collagen fiber density, do not consistently correlate with DTI metrics such as apparent diffusion coefficient (ADC), fractional anisotropy (FA), and axial (AD) and radial diffusivity (RD). Notably, muscle density derived from histology shows a partial correlation with FA. However, given that DTI FA represents the averaged anisotropy from the entire imaging voxel, encompassing both collagen and muscle fibers, it lacks specificity as a biomarker for cervical collagen and muscle fibers.

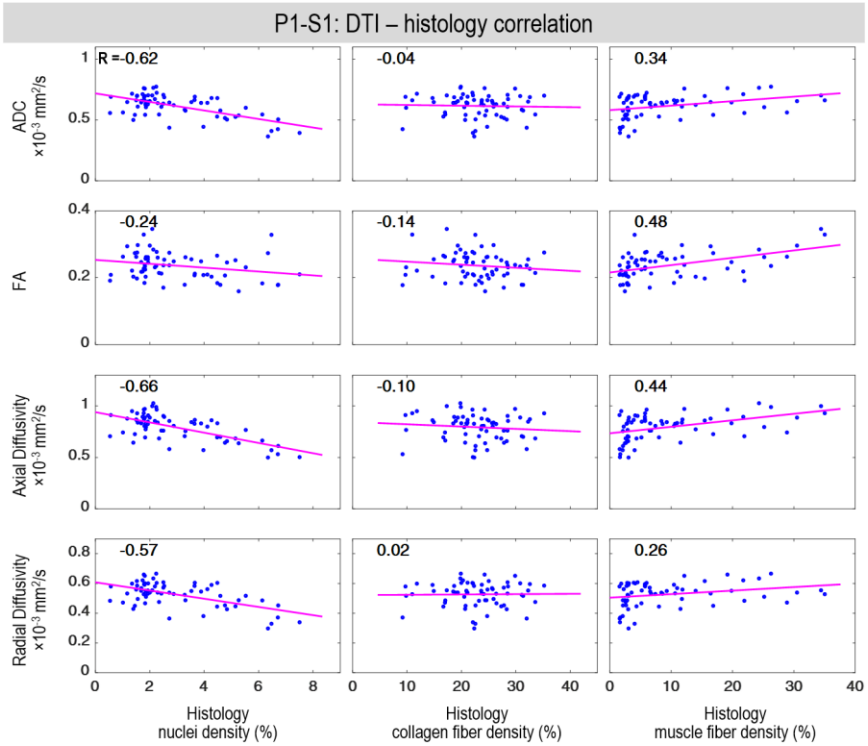

Figure 4.12: Pearson correlation analysis of DTI versus histology for specimen P1-S1.
Data points indicate mean values per grid box from Fig. 4.3, 4.4, and 4.5, panels B and C. Magenta lines: linear fits.

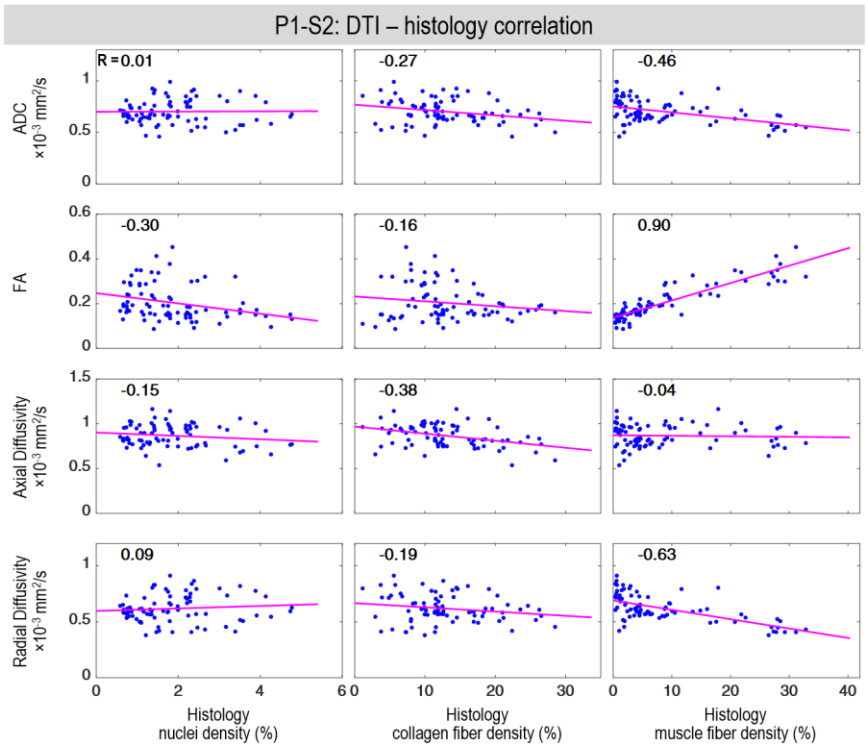

Figure 4.13: Pearson correlation analysis of DTI versus histology for specimen P1-S2.
Data points indicate mean values per grid box from Fig. 4.3, 4.4, and 4.5, panels B and C. Magenta lines: linear fits.

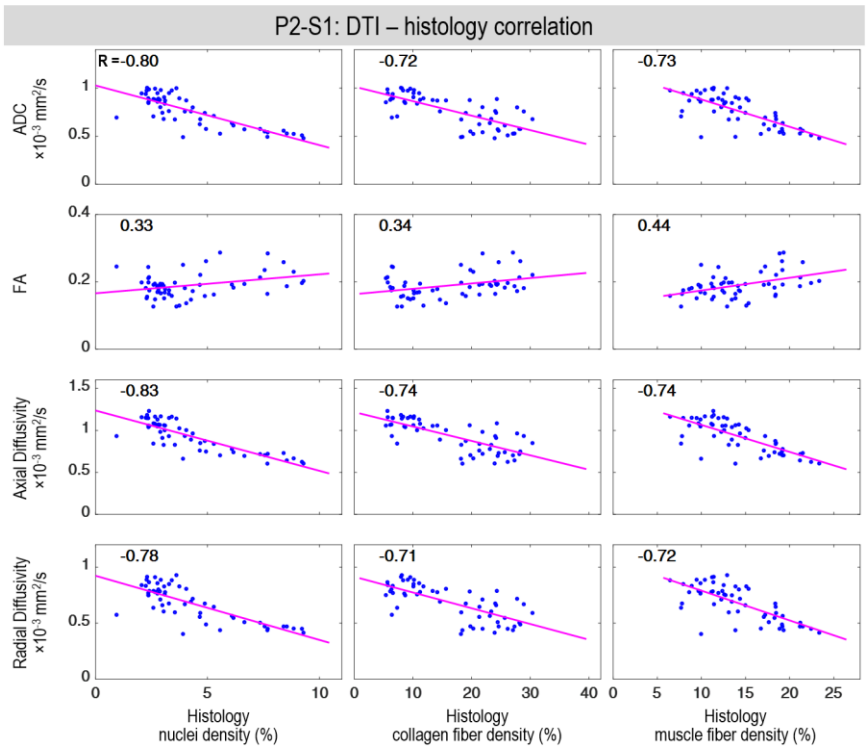

Figure 4.14: Pearson correlation analysis of DTI versus histology for specimen P2-S1.
Data points indicate mean values per grid box from Fig. 4.3, 4.4, and 4.5, panels B and C. Magenta lines: linear fits.

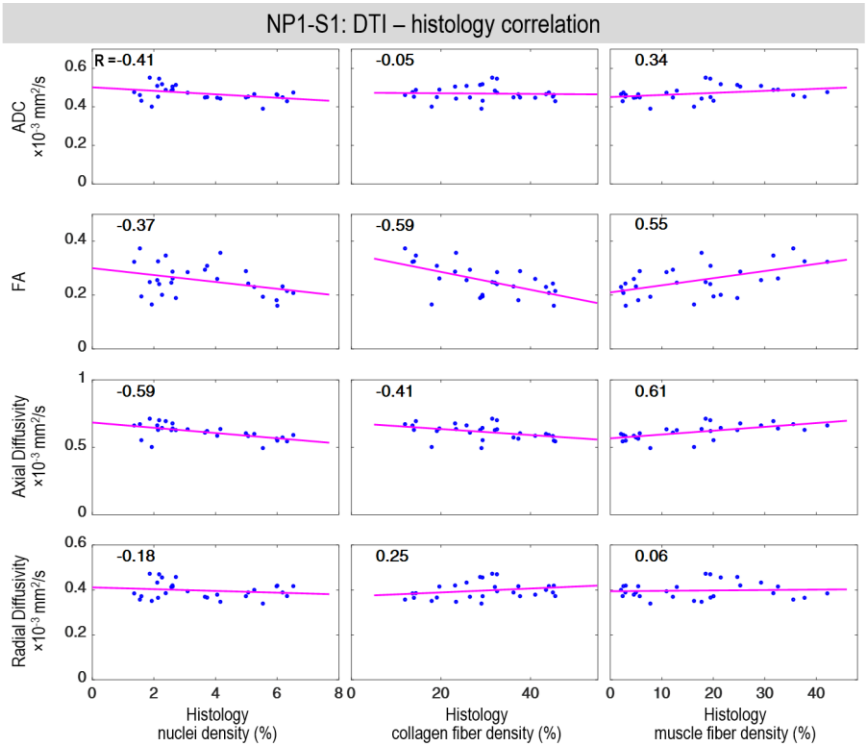

Figure 4.15: Pearson correlation analysis of DTI versus histology for specimen NP1-S1.
Data points indicate mean values per grid box from Fig. 4.3, 4.4, and 4.5, panels B and C. Magenta lines: linear fits.

4.8.3 Correlation analysis of *ex vivo* specimen between free water imaging and histology

In the free water imaging (FWI) analysis (**Figure 4.16** – **Figure 4.19**), we observe similar findings as DTI results. The histological data do not show a reliable correlation with FWI metrics.

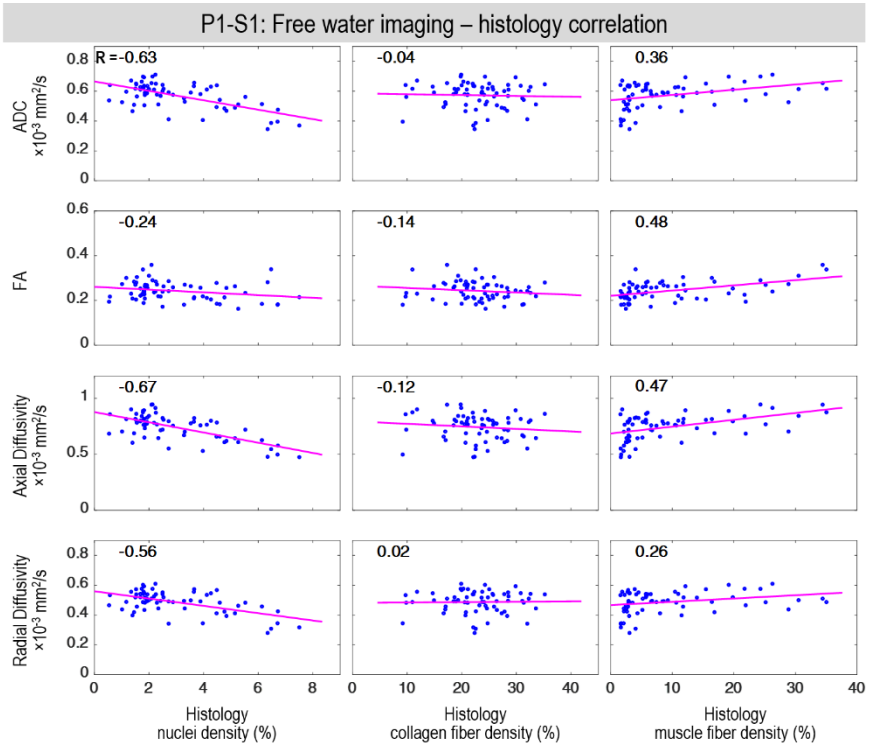

Figure 4.16: Pearson correlation analysis of FWI versus histology for specimen P1-S1.
Data points indicate mean values per grid box from Fig. 4.3, 4.4, and 4.5, panels B and C. Magenta lines: linear fits.

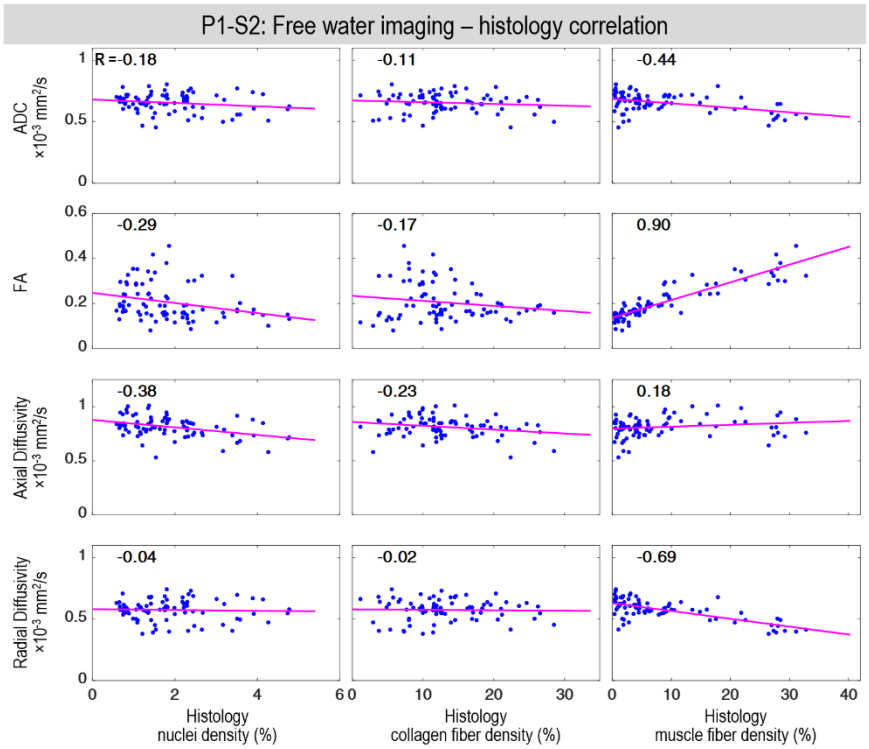

Figure 4.17: Pearson correlation analysis of FWI versus histology for specimen P1-S2.
Data points indicate mean values per grid box from Fig. 4.3, 4.4, and 4.5, panels B and C. Magenta lines: linear fits.

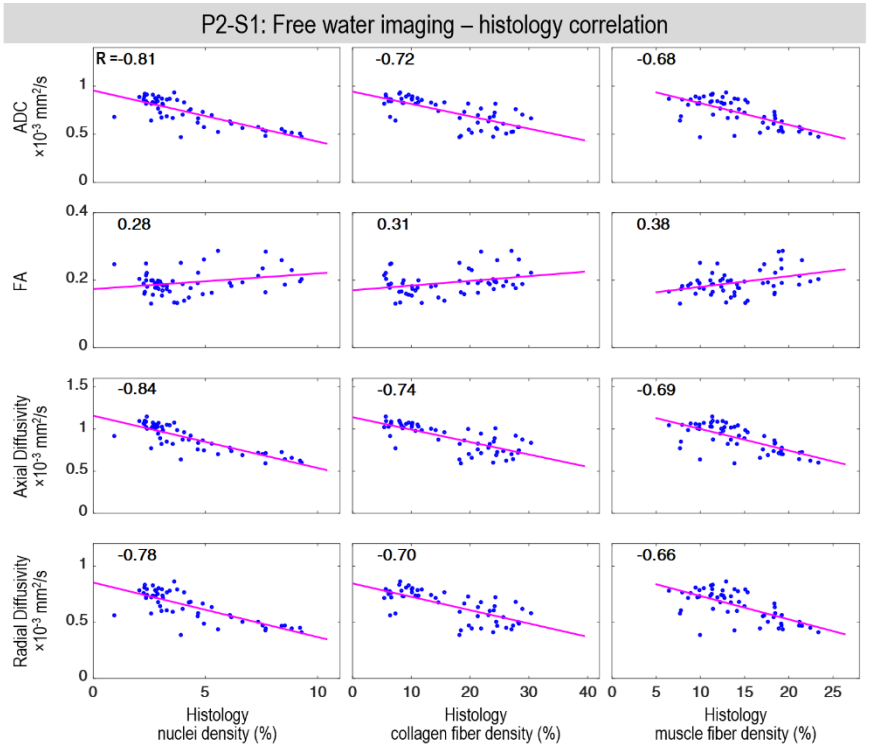

Figure 4.18: Pearson correlation analysis of FWI versus histology for specimen P2-S1.
Data points indicate mean values per grid box from Fig. 4.3, 4.4, and 4.5, panels B and C. Magenta lines: linear fits.

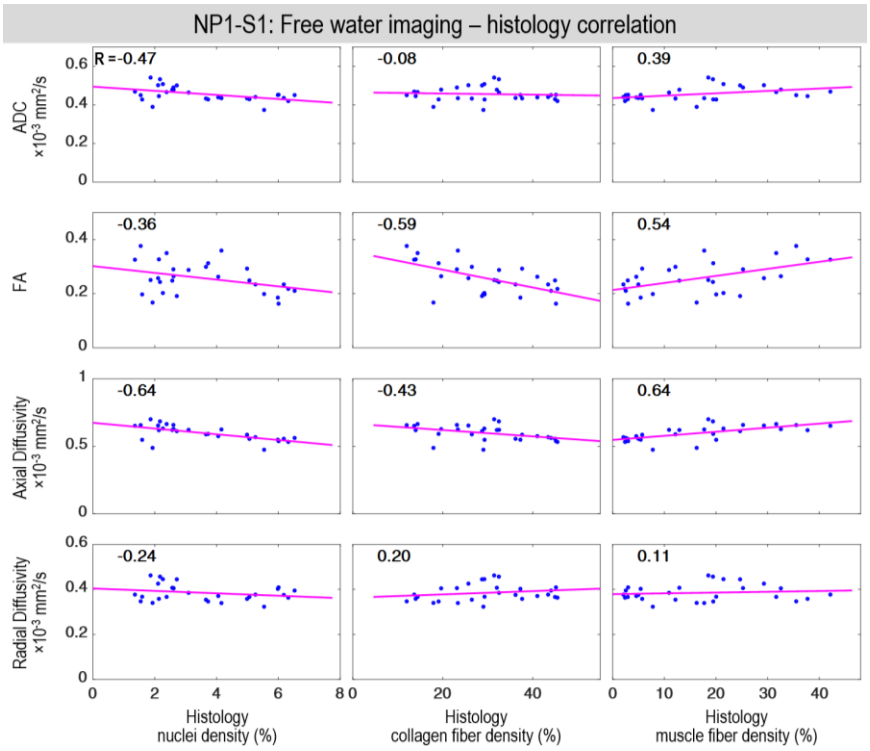

Figure 4.19: Pearson correlation analysis of FWI versus histology for specimen NP1-S1.
Data points indicate mean values per grid box from Fig. 4.3, 4.4, and 4.5, panels B and C. Magenta lines: linear fits.

4.9 Discussion

In our study, we developed and validated whole cervix DBSI measures for visualizing and quantifying microstructural features *in vivo* during human pregnancy. Our *ex vivo* results demonstrated that DBSI-derived cellularity, collagen fiber, and muscle fiber fraction maps correlated spatially with their corresponding histological maps. Furthermore, our *in vivo* data indicates that our DBSI-derived measures from the whole cervical volume, collected around 32 weeks of gestation, effectively distinguish cervical microstructural differences between term deliveries and preterm deliveries linked to inflammatory conditions.

Our DBSI findings are consistent with several previous observations regarding cervix microstructures. For example, we observed the highest cell density proximal to the subglandular

region. This was consistent with the known distribution of mucus-secreting cells in endocervical glands, which lie between the subglandular region and the endocervical canal[126–128]. Moreover, both *ex vivo* and *in vivo* DBSI-derived collagen fiber maps revealed a more homogeneous distribution of collagen in the subglandular region, adjacent to the cervical canal, than in the outer stroma region, as was observed previously[129,130]. Finally, DBSI identified muscle fibers that corresponded to those in trichrome images. These images revealed longitudinal fibers parallel to the cervical canal and circumferential fibers near the cervix-uterus junction, consistent with previous findings[96]. Combined with our *ex vivo* validation, these findings strongly indicate that our DBSI-derived measures accurately image cervix microstructures.

Our retrospective *in vivo* DBSI data indicated that the cervices from patients who later delivered preterm differed from those of patients who later delivered at term in three ways. First, the cervices from the preterm group had less collagen fraction than those from the term group, perhaps indicating premature collagen degradation. Additionally, the collagen fraction correlated with both days to delivery and cervical length measured by T2W MR images at 32 weeks of gestation. This finding is consistent with the observation that collagen concentration in the mouse cervix decreases over gestation[126].

Second, cervices in the preterm group exhibited greater cell fractions than those in the term group. Given that the preterm patients had all been diagnosed with infectious diseases or inflammatory conditions, the elevated cell fraction may reflect immune cell infiltration and elevated inflammation. The inverse correlation between DBSI cell fraction and both days to delivery and cervical length at 32 weeks of gestation suggest a link between elevated immune cell infiltration, a shorter and more dilated cervix, and proximity to delivery.

Third, cervices of the preterm group had a higher muscle fraction than those in the term group. Additionally, the muscle fraction inversely correlated with both days to delivery and cervical length at 32 weeks of gestation. These findings suggest that patients with high muscle fraction have a shorter cervix and are closer to delivery than those with a low muscle fraction. These findings align with an observation of increased smooth muscle in cervical insufficiency[131], the idea that cervical smooth muscle contraction plays a role in dilation[132], and the hypothesis that longitudinal muscle fibers can contract and promote cervical dilation[133]. In a recent *in vitro* study, an ultrasound and a force transducer were used to measure contractility in cervices from non-pregnant pre-menopausal women. The effective scatterer diameter measured by the ultrasound correlated with the generated contraction force well and both measures increased immediately after administration of oxytocin[134]. Irrespective of the precise mechanisms governing cervical smooth muscle contraction and cervical dilation, the observed increase in muscle fiber density, as revealed by our study, potentially offers an anatomical substrate that could facilitate such contractions.

Together, the three DBSI-derived measures distinguished preterm and term groups, as evidenced by the absence of overlap in the two Gaussian ellipsoids. The diversity and patient-specific nature of pathways to premature cervical dilation and preterm labor suggest that the combination of these three DBSI measures might serve as a more robust predictor of preterm labor than a single measure. This hypothesis invites further investigation in future larger studies.

One DBSI measure that showed only a small difference between the term and preterm groups was the free water fraction. Additionally, the free water fraction did not correlate with either days to delivery or cervical length at 32 weeks of gestation. It is important to note that DBSI was performed at a single time point at 32 weeks' gestation, likely before a sharp increase in hydration occurs. Moreover, Maradny et al. found small differences (about 5%) in pregnant rabbit

cervical hydration between control animals and those treated with hyaluronic acid to simulate cervix ripening[135]. Longitudinal DBSI studies conducted throughout pregnancy, with a specific focus on imaging closer to delivery, might reveal a time-dependent increase in the free water fraction.

Upon establishing the DBSI method on imaging the complex microstructure throughout the entire cervix and assessing its feasibility in discerning between normal term and preterm patients, we note several limitations of this work that point to the need for future investigation. First, in the *in vivo* analysis, all of the patients in the preterm cohort had infectious diseases or inflammatory conditions. Future studies can determine the ability of our DBSI measures to predict preterm birth in patients without any known pregnancy complications. Second, we only performed DBSI at a single timepoint. Longitudinal studies would enable us to use our DBSI measures to track patient-specific cervical remodeling. Third, in our H&E staining, we quantified nuclei density and compared it to DBSI cell fractions, which were defined as having a wide range of sizes. Future effort can be directed at developing DBSI parameters to quantitate specific immune cell types such as macrophages, etc. and validating them by using specific immunohistochemistry stains. In this way, we will obtain more specific information regarding the ability of DBSI to measure cervical inflammation.

Chapter 5 : Conclusions and future works

5.1 Conclusions

This dissertation has centered around three core biomarkers of preterm birth: uterine contractility, placental inflammation, and cervical integrity. It has established foundational work in electromyometrial imaging (EMMI) for uterine contractions, diffusion basis spectrum imaging (DBSI) for placental immune response and cervical microstructure, thereby confirming their accuracy, robustness, and clinical applicability.

In the first aim addressing uterine contractility, we provided evidence that potential maps generated through EMMI—based on non-invasive body surface recordings—are align well with maps acquired via direct uterine electrode placement. Additionally, our computational models confirmed that EMMI maintains its accuracy under clinically relevant variables to clinical settings, such as maternal and fetal movements and electrical noise. The clinical feasibility of EMMI was further confirmed by noninvasive EMMI mapping utilizing body-surface electrical recordings and MRI-derived anatomical data.

The second aim, targeting placental inflammation, involved the development and validation of placenta-specific DBSI metrics for the quantification and visualization of cellularity and inflammation. Our *ex vivo* results confirmed that DBSI-derived maps of cellularity and apparent diffusion coefficient (ADC) show strong spatial correlation with histological maps.

In the third aim addressing cervical integrity, we developed and validated the whole cervix DBSI to visualize and quantify microstructural features *in vivo* during human pregnancy. Our *ex vivo* results demonstrated that DBSI-derived cellularity, collagen fiber, and muscle fiber fraction

maps correlated spatially with their corresponding histological maps. Our *in vivo* findings indicated that DBSI metrics acquired around the 32nd week of gestation are capable of discriminating between patients delivering at term and those susceptible to inflammatory conditions leading to preterm delivery.

5.2 Future works

The future works of this dissertation can be considered on each aim individually and collectively.

For EMMI imaging of uterine contraction, future development aims to augment its utility in both research and clinical domains. In research settings, EMMI will continue to employ MRI to provide precise anatomical information. Clinically, we plan to transition towards more portable imaging solutions for anatomical imaging, such as ultrasound, particularly in delivery room scenarios. Additionally, there is a desire towards implementing a streamlined electrical mapping system employing fewer electrodes to facilitate real-time monitoring during labor. The future of EMMI's clinical research involves rigorous analysis on a large, comprehensive cohort to better understand the electrophysiologic properties involved in term and preterm labor.

EMMI's potential clinical applications could be in several ways. First, EMMI could serve as a triaging tool, assisting in the clinical decision-making process for pregnant women presenting with contractions by providing detailed 3D imagery of contraction initiation and propagation patterns. Second, EMMI may help assess the effects of medical tocolytic therapy in ways beyond the current tocodynamometer technology. Finally, a deeper understanding of uterine electrophysiology and pathophysiology could inspire innovative approaches to labor management, similar to current cardiac arrhythmia interventions, including sodium channel modulation, pacing

strategies, and even catheter-based ablation of hyperactive uterine regions to mitigate the risk of preterm labor.

In the context of future work for placenta-specific DBSI imaging, several areas warrant exploration to extend DBSI's clinical applicability. The application of DBSI in longitudinal *in vivo* clinical studies could facilitate patient-specific monitoring of placental inflammation over the gestation. Further refinement in specificity and resolution may be achieved through the incorporation of more targeted immunohistochemical stains, the utilization of high resolution 7-Tesla MRI and the application of advanced machine learning algorithms in DBSI. Such advancements could enable the differentiation of various types of immune cells, thereby enhancing the specificity of placental immune response assessment and corresponding treatment plans. Additionally, we propose the development of three-dimensional histological models using CLARITY technology to facilitate volumetric correlation with DBSI-derived metrics. This integration would offering a robust framework for evaluating pathological inflammation in the placenta.

For future work in whole-cervix Diffusion Basis Spectrum Imaging (DBSI), expanding the patient cohort to include individuals without known pregnancy complications could enhance the predictive capability of our DBSI metrics for preterm birth. Additionally, longitudinal studies may allow for the tracking of patient-specific cervical remodeling over time by the DBSI metrics. Furthermore, while our H&E staining focused on quantifying nuclei density and compared it with DBSI-defined cell fractions of varying sizes, subsequent research could aim to refine DBSI parameters for the quantification of specific immune cell types, such as macrophages. These refined parameters could then be validated using targeted immunohistochemical staining

techniques, thereby providing a more nuanced understanding of the capabilities of DBSI in assessing cervical inflammation.

Combining the findings from all three imaging modalities, future research could focus on constructing a patient-specific model to monitor pregnancy progression and conditions. Utilizing a more extensive and diverse patient cohort, this model could integrate advanced machine learning algorithms and simulation techniques to predict time to delivery with higher accuracy.

References

1. Blencowe, H. *et al.* National, regional, and worldwide estimates of preterm birth rates in the year 2010 with time trends since 1990 for selected countries: a systematic analysis and implications. *Lancet* **379**, 2162–2172 (2012).

2. Mathews, T. J. & MacDorman, M. F. Infant mortality statistics from the 2007 period linked birth/infant death data set. *Natl. vital Stat. reports from Centers Dis. Control Prev. Natl. Cent. Heal. Stat. Natl. Vital Stat. Syst.* **59**, 1–30 (2011).

3. Saigal, S. & Doyle, L. W. An overview of mortality and sequelae of preterm birth from infancy to adulthood. *Lancet* **371**, 261–269 (2008).

4. Goldenberg, R. L., Culhane, J. F., Iams, J. D. & Romero, R. Epidemiology and causes of preterm birth. *Lancet* **371**, 75–84 (2008).

5. Romero, R. *et al.* The preterm parturition syndrome. *BJOG An Int. J. Obstet. Gynaecol.* **113**, 17–42 (2006).

6. Romero, R., Dey, S. K. & Fisher, S. J. Preterm labor: one syndrome, many causes. *Science (80-.).* **345**, 760–765 (2014).

7. Timmons, B., Akins, M. & Mahendroo, M. Cervical remodeling during pregnancy and parturition. *Trends Endocrinol. Metab.* **21**, 353–361 (2010).

8. Badir, S., Mazza, E., Zimmermann, R. & Bajka, M. Cervical softening occurs early in pregnancy: characterization of cervical stiffness in 100 healthy women using the aspiration technique. *Prenat. Diagn.* **33**, 737–741 (2013).

9. Carlson, L. C., Hall, T. J., Rosado-Mendez, I. M., Mao, L. & Feltovich, H. Quantitative assessment of cervical softening during pregnancy with shear wave elasticity imaging: an in vivo longitudinal study. *Interface Focus* **9**, (2019).

10. Yoshida, K., Jayyosi, C., Lee, N., Mahendroo, M. & Myers, K. M. Mechanics of cervical remodelling: insights from rodent models of pregnancy. *Interface Focus* **9**, (2019).

11. Wray, S. & Wray, S. Insights into the uterus. *Exp. Physiol.* **92**, 621–631 (2007).

12. Harper, L. M., Shanks, A. L., Tuuli, M. G., Roehl, K. A. & Cahill, A. G. The risks and benefits of internal monitors in laboring patients. *Am. J. Obstet. Gynecol.* **209**, 38. e1-38. e6 (2013).

13. Miles, A. M., Monga, M. & Richeson, K. S. Correlation of external and internal monitoring of uterine activity in a cohort of term patients. *Am. J. Perinatol.* **18**, 137–140 (2001).

14. Eswaran, H. *et al.* Extraction, quantification and characterization of uterine magnetomyographic activity—a proof of concept case study. *Eur. J. Obstet. Gynecol. Reprod. Biol.* **144**, S96–S100 (2009).

15. Eswaran, H., Preissl, H., Murphy, P., Wilson, J. D. & Lowery, C. L. Spatial-temporal

analysis of uterine smooth muscle activity recorded during pregnancy. in *Engineering in Medicine and Biology Society, 2005. IEEE-EMBS 2005. 27th Annual International Conference of the* 6665–6667 (IEEE, 2006).

16. Hayes-Gill, B. *et al.* Accuracy and reliability of uterine contraction identification using abdominal surface electrodes. *Clin. Med. Insights Women's Heal.* **5**, CMWH. S10444 (2012).

17. Euliano, T. Y. *et al.* Monitoring uterine activity during labor: a comparison of 3 methods. *Am. J. Obstet. Gynecol.* **208**, 66. e1-66. e6 (2013).

18. Jacod, B. C., Graatsma, E. M., Van Hagen, E. & Visser, G. H. A. A validation of electrohysterography for uterine activity monitoring during labour. *J. Matern. Neonatal Med.* **23**, 17–22 (2010).

19. Hassan, M., Terrien, J., Marque, C. & Karlsson, B. Comparison between approximate entropy, correntropy and time reversibility: Application to uterine electromyogram signals. *Med. Eng. Phys.* **33**, 980–986 (2011).

20. Karlsson, B., Terrien, J., Gudmundsson, V., Steingrimsdottir, T. & Marque, C. Abdominal EHG on a 4 by 4 grid: mapping and presenting the propagation of uterine contractions. in *11th Mediterranean Conference on Medical and Biomedical Engineering and Computing 2007* 139–143 (Springer, 2007).

21. de Lau, H. *et al.* Automated conduction velocity analysis in the electrohysterogram for prediction of imminent delivery: a preliminary study. *Comput. Math. Methods Med.* **2013**, (2013).

22. Parkington, H. C., Harding, R. & Sigger, J. N. Co-ordination of electrical activity in the myometrium of pregnant ewes. *J. Reprod. Fertil.* **82**, 697–705 (1988).

23. Lammers, W. J. E. P., Stephen, B., Hamid, R. & Harron, D. W. G. The effects of oxytocin on the pattern of electrical propagation in the isolated pregnant uterus of the rat. *Pflügers Arch.* **437**, 363–370 (1999).

24. Lammers, W. J. E. P. *et al.* Patterns of electrical propagation in the intact pregnant guinea pig uterus. *Am. J. Physiol. Integr. Comp. Physiol.* **294**, R919–R928 (2008).

25. Oster, H. S., Taccardi, B., Lux, R. L., Ershler, P. R. & Rudy, Y. Noninvasive electrocardiographic imaging: reconstruction of epicardial potentials, electrograms, and isochrones and localization of single and multiple electrocardiac events. *Circulation* **96**, 1012–1024 (1997).

26. Rudy, Y. & Burnes, J. E. Noninvasive electrocardiographic imaging. *Ann. noninvasive Electrocardiol.* **4**, 340–359 (1999).

27. Ramanathan, C., Ghanem, R. N., Jia, P., Ryu, K. & Rudy, Y. Noninvasive electrocardiographic imaging for cardiac electrophysiology and arrhythmia. *Nat. Med.* **10**, 422 (2004).

28. Ghanem, R. N. *et al.* Noninvasive electrocardiographic imaging (ECGI): comparison to intraoperative mapping in patients. *Hear. Rhythm* **2**, 339–354 (2005).

29. Cuculich, P. S. *et al.* Noninvasive characterization of epicardial activation in humans with diverse atrial fibrillation patternsclinical perspective. *Circulation* **122**, 1364–1372 (2010).

30. Vijayakumar, R. *et al.* Electrophysiologic substrate in congenital long QT syndrome: noninvasive mapping with electrocardiographic imaging (ECGI). *Circulation* CIRCULATIONAHA. 114.011359 (2014).

31. Burnes, J. E., Taccardi, B., Ershler, P. R. & Rudy, Y. Noninvasive electrocardiogram imaging of substrate and intramural ventricular tachycardia in infarcted hearts. *J. Am. Coll. Cardiol.* **38**, 2071–2078 (2001).

32. Wu, W. *et al.* Noninvasive high-resolution electromyometrial imaging of uterine contractions in a translational sheep model. *Sci. Transl. Med.* **11**, (2019).

33. Wang, H. *et al.* Noninvasive electromyometrial imaging of human uterine maturation during term labor. *Nat. Commun. 2023 141* **14**, 1–13 (2023).

34. Kok, R. D., de Vries, M. M., Heerschap, A. & van den Berg, P. P. Absence of harmful effects of magnetic resonance exposure at 1.5 T in utero during the third trimester of pregnancy: a follow-up study. *Magn. Reson. Imaging* **22**, 851–854 (2004).

35. Choi, J. S. *et al.* A case series of 15 women inadvertently exposed to magnetic resonance imaging in the first trimester of pregnancy. *J. Obstet. Gynaecol. (Lahore).* **35**, 871–872 (2015).

36. Ray, J. G., Vermeulen, M. J., Bharatha, A., Montanera, W. J. & Park, A. L. Association between MRI exposure during pregnancy and fetal and childhood outcomes. *Jama* **316**, 952–961 (2016).

37. Wang, Y. & Rudy, Y. Application of the method of fundamental solutions to potential-based inverse electrocardiography. *Ann. Biomed. Eng.* **34**, 1272–1288 (2006).

38. Jenkin, G. & Young, I. R. Mechanisms responsible for parturition; the use of experimental models. *Anim. Reprod. Sci.* **82**, 567–581 (2004).

39. Elovitz, M. A. & Mrinalini, C. Animal models of preterm birth. *Trends Endocrinol. Metab.* **15**, 479–487 (2004).

40. Kastelic, J. P. *et al.* Induction of parturition in ewes with dexamethasone or dexamethasone and cloprostenol. *Can. Vet. J.* **37**, 101 (1996).

41. Rubianes, E., Rodas, E., Benech, A., Carrau, A. & Ferreira, A. Lambing and placental expulsion time after dexamethasone-induced parturition in Corriedale and Polwarth ewes. *Theriogenology* **36**, 329–334 (1991).

42. BioSemi. ActiveTwo system specification. https://www.biosemi.com/activetwo_full_specs.htm.

43. BioSemi. How does Biosemi limit the current flow to the subject? https://www.biosemi.com/faq/limit_current.htm.

44. Oster, H. S., Taccardi, B., Lux, R. L., Ershler, P. R. & Rudy, Y. Electrocardiographic imaging: noninvasive characterization of intramural myocardial activation from inverse-reconstructed epicardial potentials and electrograms. *Circulation* **97**, 1496–1507 (1998).

45. Burnes, J. E., Taccardi, B., MacLeod, R. S. & Rudy, Y. Noninvasive ECG imaging of electrophysiologically abnormal substrates in infarcted hearts. *Circulation* **101**, 533–540 (2000).

46. Burnes, J. E., Taccardi, B. & Rudy, Y. A noninvasive imaging modality for cardiac arrhythmias. *Circulation* **102**, 2152–2158 (2000).

47. Ramanathan, C. & Rudy, Y. Electrocardiographic imaging: I. Effect of torso inhomogeneities on body surface electrocardiographic potentials. *J. Cardiovasc. Electrophysiol.* **12**, 229–240 (2001).

48. Ramanathan, C. & Rudy, Y. Electrocardiographic imaging: II. Effect of torso inhomogeneities on noninvasive reconstruction of epicardial potentials, electrograms, and isochrones. *J. Cardiovasc. Electrophysiol.* **12**, 241–252 (2001).

49. Gulrajani, R. M. The forward and inverse problems of electrocardiography. *IEEE Eng. Med. Biol. Mag.* **17**, 84–101 (1998).

50. Tikhonov, A. N., Arsenin, V. I. & John, F. *Solutions of ill-posed problems*. vol. 14 (Winston Washington, DC, 1977).

51. Colli-Franzone, P. *et al.* A mathematical procedure for solving the inverse potential problem of electrocardiography. Analysis of the time-space accuracy from in vitro experimental data. *Math. Biosci.* **77**, 353–396 (1985).

52. Yu, L., Jin, Q., Zhou, Z., Wu, L. & He, B. Three-dimensional noninvasive imaging of ventricular arrhythmias in patients with premature ventricular contractions. *IEEE Trans. Biomed. Eng.* **65**, 1495–1503 (2018).

53. Cluitmans, M. J. M. *et al.* In vivo validation of electrocardiographic imaging. *JACC Clin. Electrophysiol.* 319 (2017).

54. Bulas, D. & Egloff, A. Benefits and risks of MRI in pregnancy. in *Seminars in perinatology* vol. 37 301–304 (Elsevier, 2013).

55. Hartwig, V. *et al.* Biological effects and safety in magnetic resonance imaging: a review. *Int. J. Environ. Res. Public Health* **6**, 1778–1798 (2009).

56. Chen, M. M., Coakley, F. V, Kaimal, A. & Laros, R. K. Guidelines for computed tomography and magnetic resonance imaging use during pregnancy and lactation. *Obstet. Gynecol.* **112**, 333–340 (2008).

57. Lammers, W. J., Arafat, K., el-Kays, A. & el-Sharkawy, T. Y. Spatial and temporal

variations in local spike propagation in the myometrium of the 17-day pregnant rat. *Am. J. Physiol. Physiol.* **267**, C1210–C1223 (1994).

58. Rabotti, C. & Mischi, M. Propagation of electrical activity in uterine muscle during pregnancy: a review. *Acta Physiol.* **213**, 406–416 (2015).

59. Miller, S. M., Garfield, R. E. & Daniel, E. E. Improved propagation in myometrium associated with gap junctions during parturition. *Am. J. Physiol. Physiol.* **256**, C130–C141 (1989).

60. Miyoshi, H., Boyle, M. B., MacKay, L. B. & Garfield, R. E. Gap junction currents in cultured muscle cells from human myometrium. *Am. J. Obstet. Gynecol.* **178**, 588–593 (1998).

61. Demianczuk, N., Towell, M. E. & Garfield, R. E. Myometrial electrophysiologic activity and gap junctions in the pregnant rabbit. *Am. J. Obstet. Gynecol.* **149**, 485–491 (1984).

62. Lucovnik, M. *et al.* Noninvasive uterine electromyography for prediction of preterm delivery. *Am. J. Obstet. Gynecol.* **204**, 228. e1-228. e10 (2011).

63. Hassan, M. *et al.* Better pregnancy monitoring using nonlinear correlation analysis of external uterine electromyography. *IEEE Trans. Biomed. Eng.* **60**, 1160–1166 (2013).

64. Lange, L. *et al.* Velocity and directionality of the electrohysterographic signal propagation. *PLoS One* **9**, e86775 (2014).

65. Marshall, J. M. Regulation of activity of uterine smooth muscle. *Physiol. Rev.* **42**, 213–235 (1962).

66. Young, R. C. The uterine pacemaker of labor. *Best Pract. Res. Clin. Obstet. Gynaecol.* (2018).

67. Csapo, A. The diagnostic significance of the intrauterine pressure. *Obstet. Gynecol. Surv.* **25**, 515–543 (1970).

68. Reynolds, S. R. & Heard, O. O. A multi-channel strain-gage tokodynamometer; an instrument for studying patterns of uterine contractions in pregnant women. *Bull. Johns Hopkins Hosp.* **82**, 446 (1948).

69. Lammers, W. J. E. P. The electrical activities of the uterus during pregnancy. *Reprod. Sci.* **20**, 182–189 (2013).

70. Young, R. C. Mechanotransduction mechanisms for coordinating uterine contractions in human labour. *Reproduction* REP-16-0156 (2016).

71. Wolfs, G. M. J. A. & van Leeuwen, M. Electromyographic observations on the human uterus during labour. *Acta Obstet. Gynecol. Scand.* **58**, 1–61 (1979).

72. Wolfs, G. & Rottinghuis, H. Electrical and mechanical activity of the human uterus during labour. *Arch. Gynakol.* **208**, 373–385 (1970).

73. Young, R. C. Synchronization of regional contractions of human labor; direct effects of region size and tissue excitability. *J. Biomech.* **48**, 1614–1619 (2015).

74. Ramon, C. *et al.* Synchronization analysis of the uterine magnetic activity during contractions. *Biomed. Eng. Online* **4**, 55 (2005).

75. Kalagiri, R. R. *et al.* Inflammation in Complicated Pregnancy and Its Outcome. *Am. J. Perinatol.* **33**, 1337–1356 (2016).

76. Romero, R., Gotsch, F., Pineles, B. & Kusanovic, J. P. Inflammation in Pregnancy: Its Roles in Reproductive Physiology, Obstetrical Complications, and Fetal Injury. *Nutr. Rev.* **65**, S194–S202 (2007).

77. Nadeau-Vallée, M. *et al.* Sterile inflammation and pregnancy complications: a review. *Reproduction* **152**, R277–R292 (2016).

78. Burdet, J. *et al.* Inflammation, infection and preterm birth. *Curr. Pharm. Des.* **20**, 4741–4748 (2014).

79. Gonçalves, L. F., Chaiworapongsa, T. & Romero, R. Intrauterine infection and prematurity. *Ment. Retard. Dev. Disabil. Res. Rev.* **8**, 3–13 (2002).

80. Romero, R., Espinoza, J., Chaiworapongsa, T. & Kalache, K. Infection and prematurity and the role of preventive strategies. *Semin. Neonatol.* **7**, 259–274 (2002).

81. de Moraes, L. V., Tadokoro, C. E., Gómez-Conde, I., Olivieri, D. N. & Penha-Gonçalves, C. Intravital Placenta Imaging Reveals Microcirculatory Dynamics Impact on Sequestration and Phagocytosis of Plasmodium-Infected Erythrocytes. *PLOS Pathog.* **9**, e1003154 (2013).

82. Wang, Y. *et al.* Differentiation and quantification of inflammation, demyelination and axon injury or loss in multiple sclerosis. *Brain* **138**, 1223–1238 (2015).

83. Wang, Y. *et al.* Quantification of increased cellularity during inflammatory demyelination. *Brain* **134**, 3590–3601 (2011).

84. Ramirez-Manzanares, A., Rivera, M., Vemuri, B. C., Carney, P. & Mareei, T. Diffusion basis functions decomposition for estimating white matter intravoxel fiber geometry. *IEEE Trans. Med. Imaging* **26**, 1091–1102 (2007).

85. Holz, M., Heil, S. R. & Sacco, A. Temperature-dependent self-diffusion coefficients of water and six selected molecular liquids for calibration in accurate 1H NMR PFG measurements. *Phys. Chem. Chem. Phys.* **2**, 4740–4742 (2000).

86. Easteal, A. J., Price, W. E. & Woolf, L. A. Diaphragm cell for high-temperature diffusion measurements. Tracer Diffusion coefficients for water to 363 K. *J. Chem. Soc. Faraday Trans. 1 Phys. Chem. Condens. Phases* **85**, 1091–1097 (1989).

87. Stritt, M., Stalder, A. K. & Vezzali, E. Orbit Image Analysis: An open-source whole slide image analysis tool. *PLOS Comput. Biol.* **16**, e1007313 (2020).

88. Fedorov, A. *et al.* 3D Slicer as an image computing platform for the Quantitative Imaging Network. *Magn. Reson. Imaging* **30**, 1323–1341 (2012).

89. Leppert, P. C. Anatomy and physiology of cervical ripening. *Clin. Obstet. Gynecol.* **38**, 267–279 (1995).

90. Word, R. A., Li, X.-H., Hnat, M. & Carrick, K. Dynamics of cervical remodeling during pregnancy and parturition: mechanisms and current concepts. in *Seminars in reproductive medicine* vol. 25 69–79 (Copyright© 2007 by Thieme Publishers, Inc., 333 Seventh Avenue, New York, NY …, 2007).

91. House, M., Kaplan, D. L. & Socrate, S. Relationships Between Mechanical Properties and Extracellular Matrix Constituents of the Cervical Stroma During Pregnancy. *Semin. Perinatol.* **33**, 300–307 (2009).

92. Uldbjerg, N., Ekman, G., Malmström, A., Olsson, K. & Ulmsten, U. Ripening of the human uterine cervix related to changes in collagen, glycosaminoglycans, and collagenolytic activity. *Am. J. Obstet. Gynecol.* **147**, 662–666 (1983).

93. Rechberger, T., Uldbjerg, N. & Oxlund, H. Connective tissue changes in the cervix during normal pregnancy and pregnancy complicated by cervical incompetence. *Obstet. Gynecol.* **71**, 563–567 (1988).

94. Myers, K., Socrate, S., Tzeranis, D. & House, M. Changes in the biochemical constituents and morphologic appearance of the human cervical stroma during pregnancy. *Eur. J. Obstet. Gynecol. Reprod. Biol.* **144**, S82–S89 (2009).

95. Pajntar, M. The smooth muscles of the cervix in labour. *Eur. J. Obstet. Gynecol. Reprod. Biol.* **55**, 9–12 (1994).

96. Vink, J. Y. *et al.* A new paradigm for the role of smooth muscle cells in the human cervix. in *American Journal of Obstetrics and Gynecology* vol. 215 478.e1-478.e11 (Mosby Inc., 2016).

97. Vink, J. The potential role of the cervix in myometrial function. *Curr. Opin. Physiol.* **13**, 33–37 (2020).

98. Pajntar, M. & Rudel, D. Changes in Electromyographic Activity of the Cervix after Stimulation of Labour with Oxytocin. *Gynecol. Obstet. Invest.* **31**, 204–207 (1991).

99. Stygar, D. *et al.* Increased level of matrix metalloproteinases 2 and 9 in the ripening process of the human cervix. *Biol. Reprod.* **67**, 889–894 (2002).

100. Junqueira, L. C. U. *et al.* Morphologic and histochemical evidence for the occurrence of collagenolysis and for the role of neutrophilic polymorphonuclear leukocytes during cervical dilation. *Am. J. Obstet. Gynecol.* **138**, 273–281 (1980).

101. Luque, E. H., Muñoz de Toro, M. M., Ramos, J. G., Rodriguez, H. A. & Sherwood, O. D. Role of relaxin and estrogen in the control of eosinophilic invasion and collagen remodeling in rat cervical tissue at term. *Biol. Reprod.* **59**, 795–800 (1998).

102. Timmons, B. C. & Mahendroo, M. Processes Regulating Cervical Ripening Differ from Cervical Dilation and Postpartum Repair: Insights from Gene Expression Studies. *Reprod. Sci.* **14**, 53–62 (2007).

103. Timmons, B. C., Fairhurst, A.-M. & Mahendroo, M. S. Temporal Changes in Myeloid Cells in the Cervix during Pregnancy and Parturition. *J. Immunol.* **182**, 2700–2707 (2009).

104. Hirsch, E., Filipovich, Y. & Mahendroo, M. Signaling via the type I IL-1 and TNF receptors is necessary for bacterially induced preterm labor in a murine model. *Am. J. Obstet. Gynecol.* **194**, 1334–1340 (2006).

105. Gonzalez, J. M., Xu, H., Chai, J., Ofori, E. & Elovitz, M. A. Preterm and Term Cervical Ripening in CD1 Mice (Mus musculus): Similar or Divergent Molecular Mechanisms? *Biol. Reprod.* **81**, 1226–1232 (2009).

106. Heath, V. C. F., Southall, T. R., Souka, A. P., Elisseou, A. & Nicolaides, K. H. Cervical length at 23 weeks of gestation: prediction of spontaneous preterm delivery. *Ultrasound Obstet. Gynecol.* **12**, 312–317 (1998).

107. Hassan, S. S. *et al.* Patients with an ultrasonographic cervical length ≤15 mm have nearly a 50% risk of early spontaneous preterm delivery. *Am. J. Obstet. Gynecol.* **182**, 1458–1467 (2000).

108. Taipale, P. & Hiilesmaa, V. Sonographic measurement of uterine cervix at 18–22 weeks' gestation and the risk of preterm delivery. *Obstet. Gynecol.* **92**, 902–907 (1998).

109. Sharvit, M. *et al.* Vaginal examination vs. cervical length - Which is superior in predicting preterm birth? *J. Perinat. Med.* **45**, 977–983 (2017).

110. Swiatkowska-Freund, M. & Preis, K. Elastography of the uterine cervix: implications for success of induction of labor. *Ultrasound Obs. Gynecol* **38**, 52–56 (2011).

111. Yo, Y. *et al.* Relationship between cervical elastography and spontaneous onset of labor. *Sci. Reports 2020 101* **10**, 1–8 (2020).

112. McFarlin, B. L. *et al.* Ultrasonic attenuation estimation of the pregnant cervix: a preliminary report. *Ultrasound Obstet. Gynecol.* **36**, 218–225 (2010).

113. Feltovich, H., Nam, K. & Hall, T. J. Quantitative Ultrasound Assessment of Cervical Microstructure. *http://dx.doi.org/10.1177/016173461003200302* **32**, 131–142 (2010).

114. Jiang, X. *et al.* In vivo high-resolution magnetic resonance elastography of the uterine corpus and cervix. *Eur. Radiol.* **24**, 3025–3033 (2014).

115. Yao, W. *et al.* Collagen Fiber Orientation and Dispersion in the Upper Cervix of Non-Pregnant and Pregnant Women. *PLoS One* **11**, e0166709 (2016).

116. McLean, J. P. *et al.* High-speed collagen fiber modeling and orientation quantification for optical coherence tomography imaging. *Opt. Express* **27**, 14457 (2019).

117. O'Brien, C. M. *et al.* In vivo Raman spectroscopy for biochemical monitoring of the human cervix throughout pregnancy. *Am. J. Obstet. Gynecol.* **218**, 528.e1-528.e18 (2018).

118. Masson, L. E. *et al.* In vivo Raman spectroscopy monitors cervical change during labor. *Am. J. Obstet. Gynecol.* **227**, 275.e1-275.e14 (2022).

119. Akins, M. L., Luby-Phelps, K. & Mahendroo, M. Second harmonic generation imaging as a potential tool for staging pregnancy and predicting preterm birth. *https://doi.org/10.1117/1.3381184* **15**, 026020 (2010).

120. Masselli, G. *et al.* Are second trimester apparent diffusion coefficient values of the short uterine cervix associated with impending preterm delivery? *Radiology* **280**, 897–904 (2016).

121. Weiss, S. *et al.* Three-dimensional fiber architecture of the nonpregnant human uterus determined ex vivo using magnetic resonance diffusion tensor imaging. *Anat. Rec. Part A Discov. Mol. Cell. Evol. Biol.* **288A**, 84–90 (2006).

122. Nott, J. P. *et al.* Diffusion tensor imaging determines three-dimensional architecture of human cervix: a cross-sectional study. *BJOG An Int. J. Obstet. Gynaecol.* **125**, 812–818 (2018).

123. Qi, W. *et al.* Magnetic resonance diffusion tensor imaging of cervical microstructure in normal early and late pregnancy in vivo. in *American Journal of Obstetrics and Gynecology* (Mosby Inc., 2020). doi:10.1016/j.ajog.2020.07.014.

124. Lin, T. H. *et al.* Diffusion Basis Spectrum Imaging Detects Axonal Loss After Transient Dexamethasone Treatment in Optic Neuritis Mice. *Front. Neurosci.* **14**, 1469 (2021).

125. Strain, J. F. *et al.* Diffusion Basis Spectrum Imaging Detects Ongoing Brain Inflammation in Virologically Well Controlled HIV+ Patients. *J. Acquir. Immune Defic. Syndr.* **76**, 423 (2017).

126. Read, C. P., Word, R. A., Ruscheinsky, M. A., Timmons, B. C. & Mahendroo, M. S. Cervical remodeling during pregnancy and parturition: molecular characterization of the softening phase in mice. *Reproduction* **134**, 327–340 (2007).

127. Carmichael, R. & Jeaffreson, B. L. Basal cells in the epithelium of the human cervical canal. *J. Pathol. Bacteriol.* **49**, 63–68 (1939).

128. DeSouza, N. M., Hawley, I. C., Schwieso, J. E., Gilderdale, D. J. & Soutter, W. P. The uterine cervix on in vitro and in vivo MR images: a study of zonal anatomy and vascularity using an enveloping cervical coil. *AJR. Am. J. Roentgenol.* **163**, 607–612 (1994).

129. Hao, J. *et al.* Characterization of the collagen microstructural organization of human cervical tissue. *Reproduction* **156**, 71–79 (2018).

130. Danforth, D. N. The morphology of the human cervix. *Clin. Obstet. Gynecol.* **26**, 7–13 (1983).

131. Buckingham, J. C., Buethe, R. A. & Danforth, D. N. Collagen-muscle ratio in clinically normal and clinically incompetent cervices. *Am. J. Obstet. Gynecol.* **91**, 232–237 (1965).

132. Oláh, K. S., Gee, H. & Brown, J. S. Cervical contractions: the response of the cervix to oxytocic stimulation in the latent phase of labour. *BJOG An Int. J. Obstet. Gynaecol.* **100**, 635–640 (1993).

133. Tantengco, O. A. G. & Menon, R. Contractile function of the cervix plays a role in normal and pathological pregnancy and parturition. *Med. Hypotheses* **145**, 110336 (2020).

134. Santoso, A. P., Vink, J. Y., Gallos, G., Feltovich, H. & Hall, T. J. Quantitative Ultrasound Detects Smooth Muscle Activity at the Cervical Internal Os in Vitro. *Ultrasound Med. Biol.* **46**, 149–155 (2020).

135. Maradny, E. El *et al.* The role of hyaluronic acid as a mediator and regulator of cervical ripening. *Hum. Reprod.* **12**, 1080–1088 (1997).

Appendix

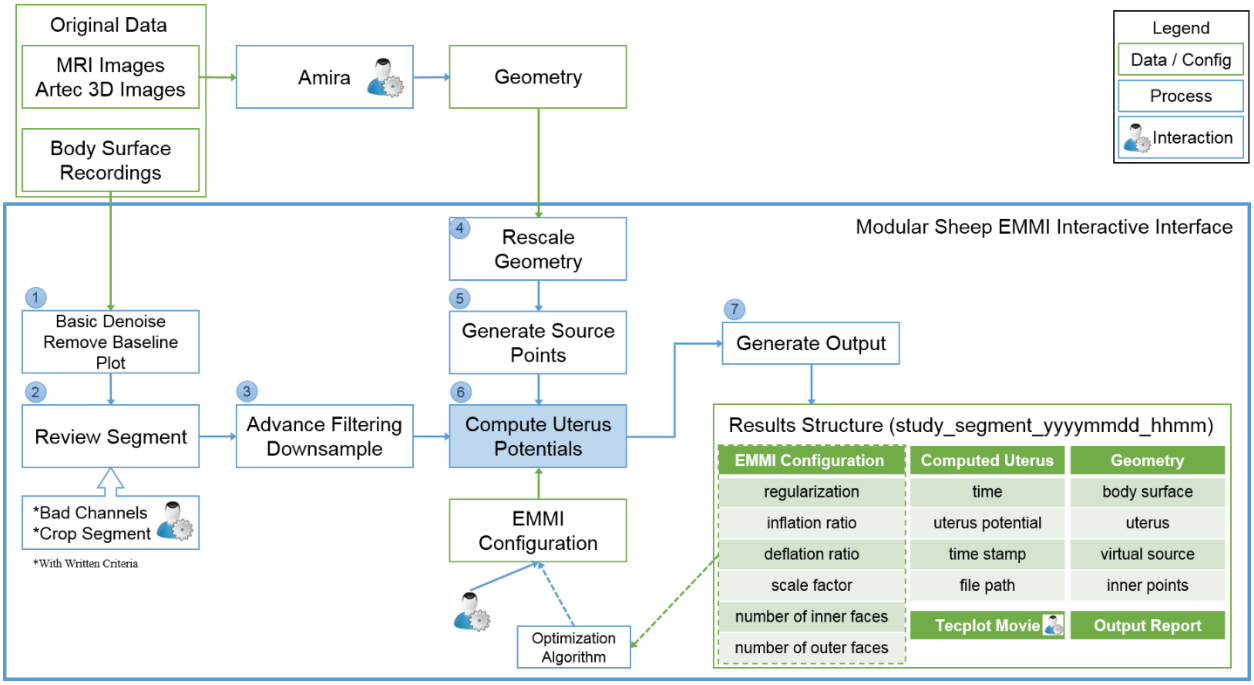

Figure Appx. 1: Software functional flowchart of interactive EMMI software.

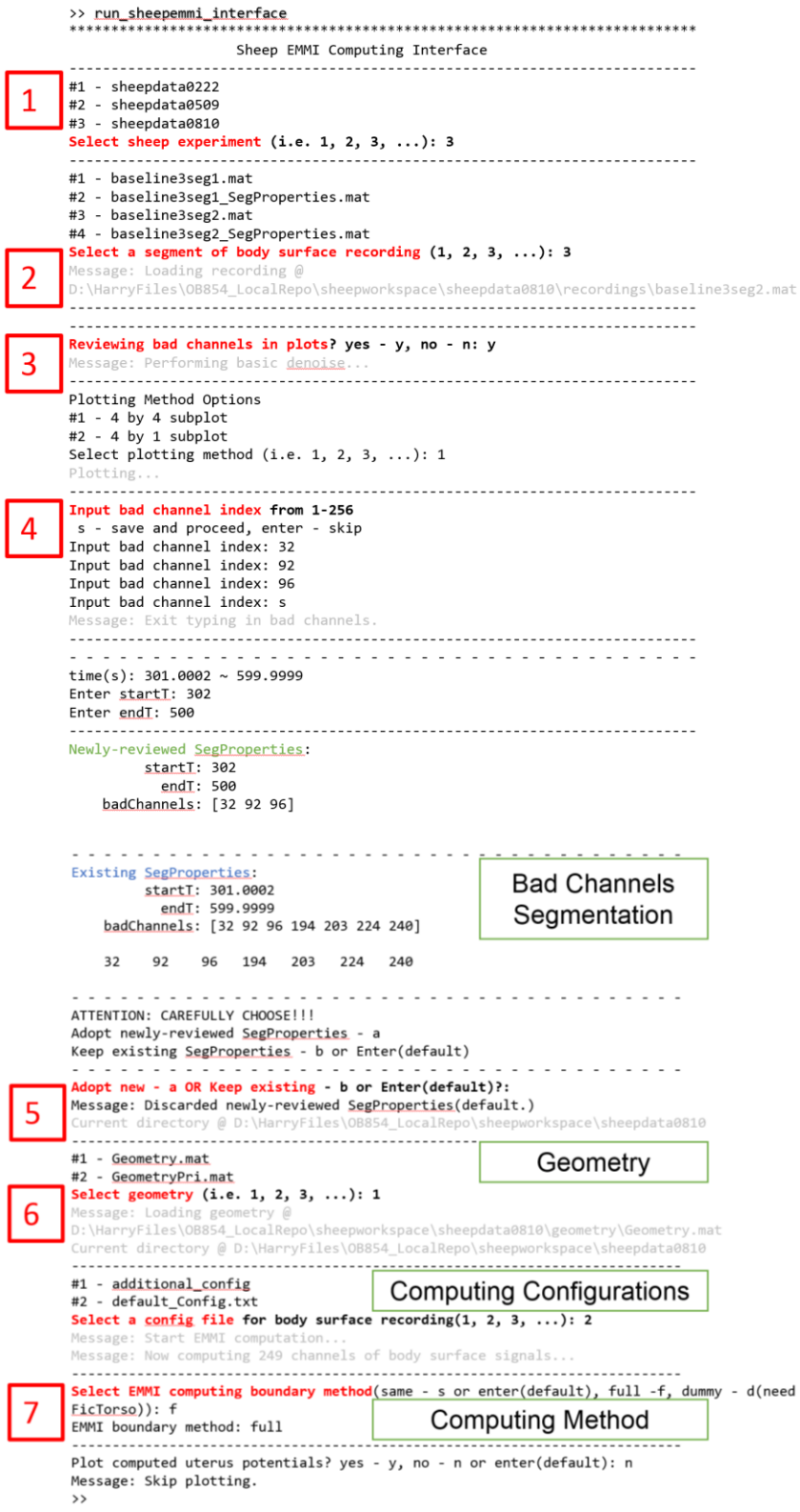

Figure Appx. 2: Example of EMMI post processing procedures in the interactive EMMI software.

Table Appx. 1: b table for DBSI

bValue in vivo	bValue ex vivo	bVector X_PE	bVector Y_RO	bVector Z_SL
0	0	0.000	0.000	0.000
10	20	0.685	0.430	0.589
50	100	0.000	-1.000	0.000
110	250	-0.046	0.895	0.443
200	450	-0.306	0.572	0.761
310	700	0.577	-0.577	0.577
540	1210	0.851	-0.500	0.162
720	1610	-0.526	-0.809	0.262
900	2020	0.000	0.808	-0.589
0	0	0.000	0.000	0.000
1120	2520	0.000	0.809	0.588
1260	2830	0.577	0.577	-0.577
1390	3130	-0.851	0.310	-0.425
1520	3410	-0.851	0.000	0.526
1640	3700	0.526	-0.500	-0.688
1770	3980	0.000	0.000	1.000
1900	4280	0.851	0.000	0.526
1900	4280	0.851	0.000	0.526
2000	4500	0.000	-0.809	-0.588
0	0	0.000	0.000	0.000
20	40	0.887	0.258	0.382
60	140	0.028	-0.693	-0.721
130	300	-0.852	-0.308	0.424
220	500	0.852	0.499	0.161
360	810	0.000	-0.309	-0.951
580	1310	0.000	-0.310	0.951
760	1710	-0.934	-0.357	0.000
940	2120	-0.577	-0.577	-0.577
0	0	0.000	0.000	0.000
1160	2620	0.000	0.934	0.356
1290	2910	0.851	0.500	-0.163
1420	3200	0.000	0.308	0.951
1550	3480	0.357	0.000	0.934
1680	3770	0.851	-0.500	-0.163
1800	4060	0.934	-0.357	0.000
1930	4350	0.851	0.000	-0.526
1800	4060	0.934	-0.357	0.000
1930	4350	0.851	0.000	-0.526
2000	4500	0.000	-0.809	-0.588
0	0	0.000	0.000	0.000
20	50	0.129	0.799	-0.588
80	180	-0.526	-0.236	-0.817
160	360	-0.272	-0.962	-0.039
270	600	0.000	-0.934	-0.358
400	910	0.357	0.000	-0.934
630	1410	-0.851	0.309	0.425
810	1810	-0.526	0.000	0.851
1030	2320	-0.850	0.000	-0.526
0	0	0.000	0.000	0.000
1200	2700	0.000	0.934	-0.357
1320	2980	-0.934	0.357	0.000
1450	3270	0.000	0.310	-0.951
1580	3560	-0.851	-0.309	-0.425
1710	3850	-0.526	-0.809	-0.263
1840	4140	0.526	0.000	-0.851
1970	4420	-0.357	0.000	0.934
1710	3850	-0.526	-0.809	-0.263
1840	4140	0.526	0.000	-0.851
1970	4420	-0.357	0.000	0.934
2000	4500	0.000	-0.809	-0.588
0	0	0.000	0.000	0.000
30	70	0.887	0.261	0.380
90	200	0.577	-0.577	-0.577
180	400	-0.357	0.000	-0.934
290	660	0.147	-0.280	0.949
490	1110	0.000	-0.934	0.356
670	1510	-0.526	0.809	0.262
850	1910	-0.526	0.500	-0.688
1080	2420	0.526	0.501	0.687
0	0	0.000	0.000	0.000
1230	2760	-0.526	0.809	-0.263
1360	3050	0.934	0.357	0.000
1480	3340	-0.526	0.000	-0.851
1610	3630	-0.526	-0.500	0.688
1740	3920	1.000	0.000	0.000
1870	4200	0.526	0.000	0.851
2000	4490	0.000	-0.809	0.588
1610	3630	-0.526	-0.500	0.688
1740	3920	1.000	0.000	0.000
1870	4200	0.526	0.000	0.851
2000	4490	0.000	-0.809	0.588
2000	4500	0.000	-0.809	-0.588